Bulk-boundary correspondence in $\mathcal{PT}$-symmetric models with non-Abelian band topology

Natascha Winter

Master Thesis
Theoretical Solid State Physics
Date: September 24, 2020

Department of Physics
University of Zurich

Supervisors:

Prof. Dr. Titus Neupert
Dr. Tomáš Bzdušek

Acknowledgment

First, I would like to thank Prof. Titus Neupert who gave me the opportunity to write this interesting thesis in his group. Special thanks go to Dr. Tomáš Bzdušek who supported me during the whole process of my thesis. He was always there if I had any questions and we had a lot of helpful discussions. In addition, he helped me a lot by understanding the theoretical concepts. I also want to thank Prof. Alexey A. Soluyanov who came up with the idea to do a master thesis on this topic.

Further thanks go to my family who supported me at home as well as to my friends for some valuable discussion on the topic. Special thanks also to S. Jöhr who helped out if I had problems with the programming in Python.

Abstract

In this thesis, we aim to gain deeper insights into the recently proposed non-Abelian topological charge that describes energy bands and band nodes in solids. First, we give a short overview on previously reported properties this charge exhibits and on how the non-commutativity is manifested. Further, we establish a bulk-boundary correspondence between the surface states and the topological charge. This we do using some existing models in $1D$ and $2D$ as well as with some new constructed models in $3D$. These two three-dimensional models have a similar surface Brillouin zone projection of the nodal lines but in one case these nodal lines are linked and in the other case they are unlinked. Using these models we further try to find a difference in the surface spectra between the linked and the unlinked case which would make it easier to differentiate between them in experiments. For all models the surface states are studied using various methods either applied on the actual band dispersion or on a spectrally flattened Hamiltonian. Finally, we formulate a conjecture on the surface states in the phase with non-Abelian topological charge of -1.

Abstract German

In dieser Arbeit möchten wir die kürzlich publizierte nicht abelsche topologische Invariante besser verstehen. Diese Invariante beschreibt Energiebänder und Entartungen zwischen diesen Bändern, sogenannte Knotenpunkte oder Knotenlinien in Festkörpern. Zuerst geben wir eine kurze Einführung in die Eigenschaften dieser Invarianten. Weiter erklären wir, wie sich die nicht vorhandene Kommutativität zeigt. Ebenfalls finden wir einen Zusammenhang zwischen dem Wert der Invarianten im Innern des Materials mit den beobachteten Zuständen an den Rändern. Dafür verwenden wir bereits existierende Modelle in einer und zwei Dimensionen sowie zwei eigens entwickelte Modelle in $3D$. Diese dreidimensionalen Modelle haben ähnliche Projektionen der Knotenlinien in die Oberflächen Brillouin-Zone mit dem Unterschied, dass im einen Fall diese Knotenlinien miteinander verlinkt sind und im anderen Fall nicht. Anhand diese zwei Modelle versuchen wir weiter einen Unterschied im Oberflächen Spektrum zwischen verlinkten und

nicht verlinkten Knotenlinien zu finden. Ein solcher Unterschied würde, es einfacher machen experimentell die Verlinkung zu überprüfen. In allen Modellen untersuchen wir die Oberflächenzustände mit verschiedenen Methoden. Diese Methoden verwenden entweder die wirkliche Bandstruktur der Modelle oder einen Hamiltonian mit flachen Bändern, aber denselben topologischen Eigenschaften. Abschliessend formulieren wir eine Hypothese über die Oberflächenzustände in der topologischen Phase mit der nicht abelschen Invarianten -1.

Contents

1. Introduction

In the past decade, the characterization of phases of matter based on symmetries has been augmented by a classification based on topological invariants. Topologically non-trivial phases of matter include a diverse spectrum of systems, with prospective applications in spintronics and quantum computing. If correlations between the constituent particles are sufficiently weak, the topological characterization of the system is obtained by considering the electron energy bands. Such topologically non-trivial bands arise for example in the topological insulator Bi_2Se_3 [1] or in the Weyl semimetal TaAs [2]. In this thesis, we focus on the recently proposed non-Abelian topological charge, which has been shown to characterize electron bands of three-dimensional nodal-line and nodal-chain semimetals, as well as of certain one-dimensional insulators [3]. The main goal of the thesis is to find a correspondence between this non-Abelian charge (as an extension of the Berry phase) and the edge states in different models for various dimensions.

In the first part of the work, which comprises Chapters 2 and 3, we start with a theoretical clarification on one-dimensional $\mathcal{PT}$-symmetric topological insulator by first introducing the well known Berry phase and afterwards giving a detailed explanation of the non-Abelian topological charge. To gain some further insights, we present three flat band models consisting of three energy bands. By choosing different rotations of the eigenstates of the flat band models, we are able to realize all topological phases. We then study these models numerically and analytically to find a first bulk-boundary correspondence between the non-Abelian charge and the edge states. Finally, we present a generalized N-band model of a topological insulator and try to reproduce the numerical results.

As a second part, consisting of Chapters 4 and 5, we go to higher dimensions and concentrate on $\mathcal{PT}$-symmetric topological semimetals that exhibit point nodes in $2D$ or line nodes in $3D$. We first generalize the non-Abelian charge to describe nodes in models with an arbitrary number of bands $N \geq 3$. Furthermore, we introduce some properties of these nodes that arise from the non-commutativity of the charge. We are mainly interested in the braiding of nodal points and the linking of nodal lines but we also check the validity of an adjusted version of doubling theorem for this topological charge. To better understand these concepts, we then introduce three models. First, we present a two-dimensional model with nodal points that perform a braiding along a tuning parameter t. Second, we introduce two models in $3D$ that have a similar diagonal projection of the nodal lines but in one model, these nodal lines are linked in the other model they are unlinked. Using these models, we answer the open questions in the last part.

Chapters 6 and 7 constitute the last part of the thesis. We first present four different

techniques to numerically detect surface states. The first three techniques use the actual band structure and try to visualize the surface states either by only looking at the finite spectrum or by checking the (surface) localization of the eigenstates. For the last method, we flatten the Hamiltonian. Thereby, we get clear bulk bands and band gaps while preserving the topology of the model and are able to clearly resolve the surface states. Applying these techniques to our different models, we finally establish a bulk-boundary correspondence for the topological charge. Furthermore, we compare the surface spectra of the linked and unlinked model and state a conjecture on the topological phase of charge -1.

We conclude and comment on possible future directions and outlooks in Chapter 8.

2. $\mathcal{PT}$-symmetric topology

In this thesis, we consider $\mathcal{PT}$-symmetric models[1] with negligible spin-orbit coupling. This allows us to drop the spin degree of freedom from the description. After a suitable rotation of the Hilbert space, we are always able to represent the $\mathcal{PT}$-symmetry as simple complex conjugation, i.e. $\mathcal{PT} = \mathcal{K}$. Therefore, we only consider real Hamiltonians for which we can also choose the eigenstates to be real.

In this chapter we review the topological invariants of such real Hamiltonians in one spatial dimension ($1D$). First we consider the well-known Berry phase and then, by an analogy to spin rotations, we motivate the definition of the non-Abelian quaternion charge. Along the way, we will find that the non-triviality of the 2π-rotation in $3D$ plays a crucial role.

2.1. Berry phase

The non-Abelian invariant we study in this work can be seen as a combination of two phenomena. On the one hand we have the Berry phase quantization for $\mathcal{PT}$-symmetric topological insulators and on the other hand we know that a 2π-rotation is non-trivial in $3D$. We now start in this section with an introduction of the Berry phase.

2.1.1. Mathematical formulation

The Berry phase is a well understood topological invariant which is often used to describe phenomena in topological band theory. From the adiabatic theorem, it is known that a state changing adiabatically in the parameter space along a closed path will return to its initial state up to a phase. Berry [4] however reported that besides a dynamical phase ($\exp(-\mathrm{i}Et/\hbar)$), the state, in addition, picks up a geometric phase ($\exp(\mathrm{i}\gamma)$), the Berry phase, which is invariant under gauge transformations, and therefore in principle an observable.

To find this phase we define a time-dependent Hamiltonian $H(\boldsymbol{R})$ where $\boldsymbol{R}$ is the vector of the time-dependent parameters $R_i = R_i(t)$, e.g. magnetic and electric fields or, in the case of electron energy bands, the momentum. We want to consider an adiabatic time evolution and ask therefore the parameters $\boldsymbol{R}(t)$ to vary slowly along a path $\mathcal{C}$ (open or closed). At each point $\boldsymbol{R}$ along this path we define an instantaneous orthonormal basis consisting of the eigenstates $|n(\boldsymbol{R})\rangle$ of $H(\boldsymbol{R})$. These are found (up to a phase) by a diagonalization of the Hamiltonian, i.e. $H(\boldsymbol{R})|n(\boldsymbol{R})\rangle = E_n(\boldsymbol{R})|n(\boldsymbol{R})\rangle$. By picking

[1] $\mathcal{PT}$-symmetry means that the system is invariant under combined parity and time-reversal symmetry but does not have to be invariant under the two symmetries separately.

a gauge, we can also fix the phase of the eigenstates to remove the arbitrariness. We choose the phase (or more precisely the gauge) such that the function $|n(\boldsymbol{R})\rangle$ is smooth and single valued along the path $\mathcal{C}$. If this is not possible we instead choose a piecewise smooth and single-valued gauge in a finite neighborhood in the parameter space.

Starting with an initial pure state $|n(\boldsymbol{R}(0))\rangle$, we analyze the phase it picks up when slowly moving along the path $\mathcal{C}$. By the adiabatic theorem, we know that if we start with an eigenstate at $t = 0$, we stay in an instantaneous eigenstate of the system for any other t during the evolution of the Hamiltonian $H(\boldsymbol{R}(t))$. The only degree of freedom we have is a phase $\theta(t)$ which, as we already know, is in general not zero because of the dynamical phase factor related to the energy of the eigenstate. However, as already mentioned above, this is not all that it encompasses. We consider the time evolution of the system for the state $|\psi(t)\rangle = \exp(-\mathrm{i}\theta(t))|n(\boldsymbol{R}(t))\rangle$:

$$H(\boldsymbol{R}(t))|\psi(t)\rangle = \mathrm{i}\hbar\frac{\mathrm{d}}{\mathrm{d}t}|\psi(t)\rangle \tag{2.1.1}$$

This can be rewritten as:

$$E_n(\boldsymbol{R}(t))|n(\boldsymbol{R}(t))\rangle = \hbar\left(\frac{\mathrm{d}}{\mathrm{d}t}\theta(t)\right)|n(\boldsymbol{R}(t))\rangle + \mathrm{i}\hbar\frac{\mathrm{d}}{\mathrm{d}t}|n(\boldsymbol{R}(t))\rangle \tag{2.1.2}$$

taking the scalar product by multiplying with $\langle n(\boldsymbol{R}(t))|$ from the left, we have:

$$E_n(\boldsymbol{R}(t)) - \mathrm{i}\langle n(\boldsymbol{R}(t))|\frac{\mathrm{d}}{\mathrm{d}t}|n(\boldsymbol{R}(t))\rangle = \hbar\frac{\mathrm{d}}{\mathrm{d}t}\theta(t) \tag{2.1.3}$$

This results in the following equation:

$$\theta(t) = \frac{1}{\hbar}\int_0^t E_n(\boldsymbol{R}(t'))\mathrm{d}t' - \mathrm{i}\int_0^t \langle n(\boldsymbol{R}(t'))|\frac{\mathrm{d}}{\mathrm{d}t'}|n(\boldsymbol{R}(t'))\rangle\mathrm{d}t' \tag{2.1.4}$$

where the first term on the right hand side represents the dynamical phase or time evolution of the state and the second term represents the Berry phase γ defined as:

$$\gamma_n = \mathrm{i}\int_0^t \langle n(\boldsymbol{R}(t'))|\frac{\mathrm{d}}{\mathrm{d}t'}|n(\boldsymbol{R}(t'))\rangle\mathrm{d}t' \tag{2.1.5}$$

Then the corresponding state of the system is given as:

$$|\psi(t)\rangle = \exp\left(\frac{-\mathrm{i}}{\hbar}\int_0^t E_n(\boldsymbol{R}(t'))\mathrm{d}t'\right)\exp(\mathrm{i}\gamma_n(t)|n(\boldsymbol{R}(t))\rangle \tag{2.1.6}$$

Going back to our path $\mathcal{C}$, we can rewrite the Berry phase as:

$$\gamma_n = \mathrm{i}\int_{\mathcal{C}}\langle n(\boldsymbol{R})|\nabla_{\boldsymbol{R}}|n(\boldsymbol{R})\rangle\cdot\mathrm{d}\boldsymbol{R} = \int_{\mathcal{C}}\mathrm{d}\boldsymbol{R}\cdot\boldsymbol{A}_n(\boldsymbol{R}) \tag{2.1.7}$$

where in the last step we defined the Berry connection as:

$$\boldsymbol{A}_n(\boldsymbol{R}) = \mathrm{i}\langle n(\boldsymbol{R})|\frac{\partial}{\partial\boldsymbol{R}}|n(\boldsymbol{R})\rangle \tag{2.1.8}$$

For closed paths (which are considered most often when talking about Berry phases) we simply replace $\int_{\mathcal{C}}$ by $\oint_{\mathcal{C}}$.

The Berry phase is real from the fact that $\langle n(\boldsymbol{R})|\frac{\partial}{\partial \boldsymbol{R}}|n(\boldsymbol{R})\rangle$ is imaginary and therefore the Berry connection is real, otherwise the state would decay exponentially. On the other hand, obviously the Berry connection (actually a vector potential) is gauge dependent. We can perform a gauge transformation with a smooth single-valued function $\zeta(\boldsymbol{R})$:

$$|n(\boldsymbol{R}(t))\rangle \longrightarrow \mathrm{e}^{\mathrm{i}\zeta(\boldsymbol{R})}|n(\boldsymbol{R}(t))\rangle \qquad \boldsymbol{A}_n(\boldsymbol{R}) \longrightarrow \boldsymbol{A}_n(\boldsymbol{R}) - \frac{\partial}{\partial \boldsymbol{R}}\zeta(\boldsymbol{R}) \tag{2.1.9}$$

So by a gauge transformation, the Berry phase changes by $\zeta(\boldsymbol{R}(0)) - \zeta(\boldsymbol{R}(T))$ with $\boldsymbol{R}(T)$ the end point of the path $\mathcal{C}$. This might suggest that by a smart choice of $\zeta(\boldsymbol{R})$, it is possible to gauge away the Berry phase. However, this is clearly not possible if we choose a closed path with $\boldsymbol{R}(0) = \boldsymbol{R}(T)$. As we have chosen the eigenstate basis to be single-valued, we know that for the same set of parameters, we need to return to the same state, i.e. $|n(\boldsymbol{R}(0))\rangle = |n(\boldsymbol{R}(T))\rangle$. Therefore, we find $\zeta(\boldsymbol{R}(0)) - \zeta(\boldsymbol{R}(T)) = 2\pi m$ with m an integer and can only gauge away the Berry phase in the special case where it is an integer.

If we restrict ourselves to closed contractible paths, i.e. the path has a well-defined interior without holes, we can apply Stokes' theorem and find the following formula for the Berry phase:

$$\gamma_n = -\operatorname{Im}\int \mathrm{d}\boldsymbol{S}\cdot(\nabla_{\boldsymbol{R}} \wedge \langle n(\boldsymbol{R})|\nabla_{\boldsymbol{R}}|n(\boldsymbol{R})\rangle) = -\operatorname{Im}\int \mathrm{d}\boldsymbol{S}\cdot\langle\nabla_{\boldsymbol{R}} n(\boldsymbol{R})| \wedge |\nabla_{\boldsymbol{R}} n(\boldsymbol{R})\rangle) \tag{2.1.10}$$

where in the last formula we define the Berry curvature:

$$F = \nabla_{\boldsymbol{R}} \wedge \boldsymbol{A} = \langle\nabla_{\boldsymbol{R}} n(\boldsymbol{R})| \wedge |\nabla_{\boldsymbol{R}} n(\boldsymbol{R})\rangle) \tag{2.1.11}$$

with $\wedge$ being the wedge product, which in the three-dimensional case is the cross product $\times$. The Berry phase on closed paths is a gauge-invariant quantity that depends only on the path in the parameter space and not on its time dependence [4, 5].

2.1.2. Understanding of the Berry phase as parallel transport

This up to now very technical consideration of the Berry phase can also be understood as the parallel transport of a vector. More precisely, we can relate the Berry phase to the geometric phenomena of anholonomy. This means that some variables fail to return to their initial value while the variables they depend on are changed along a closed path. To understand this phenomena, we first consider the parallel transport of a vector on a sphere.

As a simple illustration, we take a unit sphere centered at the origin and the starting point of the vector to be at the upper pole of the sphere at $(0, 0, 1)$ pointing in some direction $\boldsymbol{e}$ (illustrated in Figure 2.1). For parallel transport, we require the vector to always lie in a tangent plane of the sphere and to keep its orientation when moving along the path. We now transport the vector along a simple three-segment path that consists

of first descending to the equator along a meridian, then move along the equator, and finally move back up to the pole along a different meridian. Although coming back to the starting point, the vector will point to a different direction rotated by an angle α that depends on the details of the path. This observation can also be generalized to arbitrary starting points and paths.

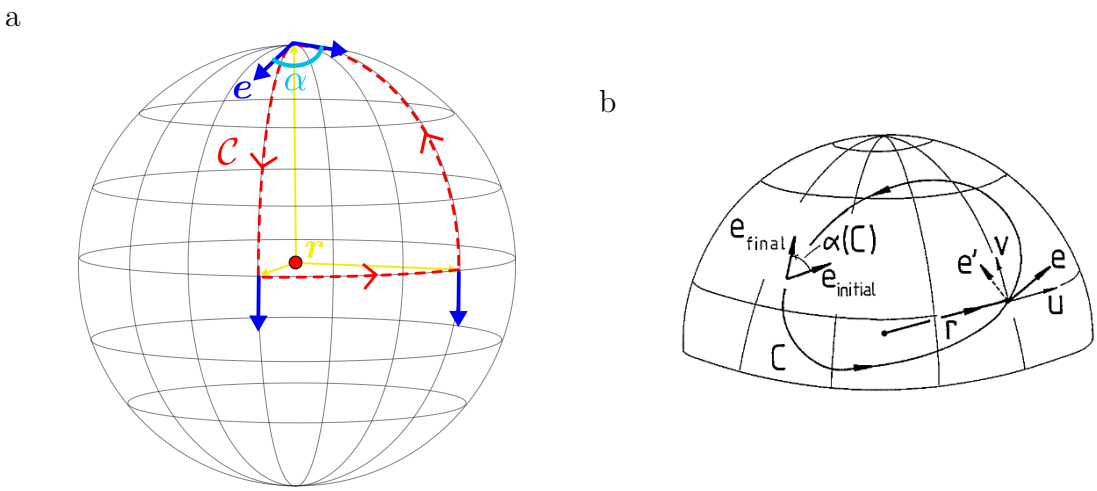

Figure 2.1.: Parallel transport: Panel (a) shows the described parallel transport on a sphere starting at the pole. The blue vector is the transported one $\boldsymbol{e}$, the yellow vectors indicate specific positions $\boldsymbol{r}$ and the red dashed lines indicate the path $\mathcal{C}$. In panel (b), adapted from [6], there is a generalization for an arbitrary path on a sphere.

Following Ref. [6], we can describe this process mathematically. We have a transported unit vector $\boldsymbol{e}$ attached at a point $\boldsymbol{r}$ on a sphere. During the transport, we shift the point $\boldsymbol{r}$ on a closed path $\mathcal{C}$ around the sphere with two conditions: i) $\boldsymbol{e} \cdot \boldsymbol{r} = 0$ and ii) the plane in which $\boldsymbol{e}$ and $\boldsymbol{r}$ lie is not allowed to rotate around $\boldsymbol{r}$. The second condition can be reformulated, using the angular velocity of the plane $\boldsymbol{\Omega} = \boldsymbol{r} \wedge \dot{\boldsymbol{r}}$, as $\boldsymbol{\Omega} \cdot \boldsymbol{r} = 0$. With this we can define the nonintegrable law for parallel transport: $\dot{\boldsymbol{e}} = \boldsymbol{\Omega} \wedge \boldsymbol{e}$. If now $\boldsymbol{r}$ returns to its initial point, the direction of $\boldsymbol{e}$ will change by an angle $\alpha(\mathcal{C})$, called the anholonomy. To determine the angle, we first define $\boldsymbol{e'} = \boldsymbol{r} \wedge \boldsymbol{e}$ to get an orthonormal frame, and then consider the complex unit vector $\boldsymbol{\psi} = \frac{1}{\sqrt{2}}(\boldsymbol{e} + \mathrm{i}\boldsymbol{e'})$. Using this vector, the law for parallel transport reads: $\mathrm{Im}\, \boldsymbol{\psi}^* \cdot d\boldsymbol{\psi} = 0$ with $d\boldsymbol{\psi}$ the change of $\boldsymbol{\psi}$ induced by the change of $\boldsymbol{r}$ to $\boldsymbol{r} + d\boldsymbol{r}$. In the next step, we express ψ in a local basis $\boldsymbol{u}(\boldsymbol{r})$, $\boldsymbol{v}(\boldsymbol{r})$ of the tangent plane (e.g the longitude and latitude of the sphere) as $\psi = \boldsymbol{n}\mathrm{e}^{-\mathrm{i}\alpha}$ where $\boldsymbol{n} = \frac{1}{\sqrt{2}}(\boldsymbol{u} + \mathrm{i}\boldsymbol{v})$.

Then the anholonomy becomes:

$$\alpha(\mathcal{C}) = \oint_{\mathcal{C}} \mathrm{d}\alpha = \mathrm{Im} \oint_{\mathcal{C}} \boldsymbol{n}^* \cdot \mathrm{d}\boldsymbol{n} = \mathrm{Im} \int (\mathrm{d}\boldsymbol{n}^* \wedge \mathrm{d}\boldsymbol{n}) \cdot \boldsymbol{n} \tag{2.1.12}$$

where the last integral is over the area on the sphere enclosed by $\mathcal{C}$.

In a similar way, it is possible to describe parallel transport of a quantum state. We reinterpret the complex vector $\boldsymbol{\psi}$ as a state $|\psi\rangle$ and the position $\boldsymbol{r}$ as a point in the parameter space $\boldsymbol{R}$. In this case we have as a nonintegrable transport law the following connection:

$$\mathrm{Im}\langle\psi|\mathrm{d}\psi\rangle = 0 \tag{2.1.13}$$

For the geometric phase we find that:

$$\langle\psi_{initial}|\psi_{final}\rangle = \exp(\mathrm{i}\gamma(\mathcal{C})) \tag{2.1.14}$$

which, after a closer look, matches the definition of the Berry phase on a closed loop (Equation 2.1.10) if we use $|\psi\rangle = |n(\boldsymbol{R})\rangle \exp(\mathrm{i}\gamma)$ [6, 7, 8].

So we find a direct correspondence between the Berry phase and the geometric parallel transport. The analog of the Berry connection using the complex vector $\boldsymbol{\psi}$ is given as $\boldsymbol{\psi}^* \cdot \mathrm{d}\boldsymbol{\psi}$ [9].

2.1.3. 1D lattice Hamiltonian

We now want to consider the Berry phase in the case of periodic crystals. If we have a crystal with periodicity a (lattice parameter) in real space, by the Bloch theorem, we know that the eigenstates are plane waves with a periodic modulated amplitude. Now switching to the reciprocal space, the eigenstates[2] will again have a periodicity, now of $\frac{2\pi}{a}$. Using this we can characterize all states within the Brillouin zone (BZ) and label them with momentum $\boldsymbol{k}$ and band index n. So we arrive at the picture of energy bands inside the BZ $[-\pi/a, \pi/a]^d$ where d is the dimension of the system [11].

If we consider periodic boundary conditions, we know that the BZ is a torus. This torus is a natural parameter space for the definition of the Berry phase. Considering the states $|\psi(n, \boldsymbol{k})\rangle$, we know they pick up a Berry phase on closed paths inside the BZ.

For simplicity, we look at the one-dimensional case and take as a closed path simply the BZ $[-\pi/a, \pi/a]$. Like this we can assign a Berry phase to every isolated energy band in the $1D$-system. Due to the symmetry of the Bloch states, the Berry phase in a $1D$ crystal is quantized to 0 or π [12]. In the case of $\mathcal{PT}$-symmetric systems this can be seen if we take a gauge in which the eigenstates of the Hamiltonians are real. Therefore considering any closed path, the only thing the eigenstate can do (if it has to stay real), is to switch sign, which corresponds to a Berry phase of π.

If we now consider a $\mathcal{PT}$-symmetric Hamiltonian with N energy bands, there is a further restriction concerning the Berry phase. Namely, the sum of the Berry phases over all bands needs to be zero (modulo 2π) [3]. Recently, this has been shown to be true only if all the atomic orbitals constituting the model lie inside the Wigner-Seitz cell and not on its boundary. If, in contrast, they are on the unit cell boundaries, the condition can be violated [13].

[2] This is actually only true if all the orbitals are centered in the unit cell as they are in all the models, we consider in this thesis. Further explanation for the case when the orbitals are not centered can be found in Chapter 3 of Ref. [10].

2.2. Frame rotation

In this section, we present the second building block of the non-Abelian invariant, the non-triviality of the 2π-rotation. To do so, we concentrate on three-band models with isolated bands. Since the eigenstates of such a Hamiltonian are three orthogonal 3-component vectors, they constitute an orthogonal frame, that can always be chosen to be right-handed. Moving along a closed path around the BZ, the eigenframe changes continuously. Returning to the same point in the BZ, we know that the Hamiltonian has to stay the same. With the Berry phase we have observed one possibility, how a single eigenstate can change. It can flip its sign. For the frame to stay right-handed, we cannot flip the sign of only one state, but we need to flip an even number of signs. Such flips of two signs correspond to a π-rotation around the state that does not flip its sign.

Using these properties we can define the parameter space for 3-band models as the quotient space $M_3 = SO(3)/D_2$ where $D_2 = \{1, C_{2x}.C_{2y}.C_{2z}\}$ is the space including the identity and the three π-rotations around the axes. The topological invariant characterizing the possible topological obstructions of the Hamiltonian along a closed path in k-space is given by the fundamental group of the parameter space.

To determine this fundamental group we can make use of the theorem by Mermin [14] that tells us: If the space G is simply connected and H subgroup of it, then we have that:

$$\Pi_1(G/H) = \Pi_0(H) \tag{2.2.1}$$

with Π_0 the set of connected components. This fundamental group of the parameter space M_3 then captures the non-Abelian band topology that we discuss in Section 2.3 but before we want to obtain some intuition about M_3 by first studying the topology of $SO(3)$.

Having this in mind, we want to look at the transformations a frame can do on a closed path and will eventually conclude that the quantization of the Berry phase is not enough to describe all the possible topological obstructions of energy bands in $1D$ [3].

2.2.1. Non-triviality of 2π-rotations

To see why this characterization of bands using the Berry phase is not enough, we now want to consider the non-triviality of a 2π-rotation in three-dimensional space. Therefore, we have a closer look at the topology of $SO(3)$.

A first simple possibility to see that a 2π rotation is topologically non-trivial is the Dirac belt trick [15]. Consider holding a belt letting the orientation of both ends fixed. If you now twist the belt by rotating one of its ends with respect to the other by 2π, there is no possibility to untwist the belt without cutting it, while fixing the orientation of the ends. In contrast, if you twist the belt by 4π, there is a possibility to untwist it letting the orientation of both ends fixed[3].

[3] A nice illustration of this trick is the following video: `https://www.youtube.com/watch?v=Vfh21o-JW9Q`

Now, we also want to see this in a more mathematical way. Having a closer look at $SO(3)$, we see that all rotations can be represented by a rotation axis $\boldsymbol{n}$ and a rotation angle α. With this in mind, we can represent all rotations as points $\alpha\boldsymbol{n}$ inside a ball of radius π. This works as we can interpret a rotation with an angle $\alpha \in (\pi, 2\pi]$ around $\boldsymbol{n}$ as a rotation with $\tilde{\alpha} = 2\pi - \alpha$ around the axis $-\boldsymbol{n}$. Further, we can identify antipodal points with each other as $\pi\boldsymbol{n} = -\pi\boldsymbol{n}$. In this setting, we can represent a 2π-rotation as a straight line connecting two antipodal points and thereby going through the center of the ball. This line then represents a closed path. For this rotation to be topologically trivial, we should be able to continuously contract the loop to a point. However, there is no possibility to do this, as the two points where the path intersects the surface of the ball need to stay at the antipodal positions for the loop to stay closed. In contrast, if we in addition consider a second 2π-rotation (possibly around a different axis $\boldsymbol{n}'$), we end up with a 4π-rotation which can be trivialized by a continuous transformation of the closed loop. This transformation is done by keeping the ends of the paths at antipodal positions but connecting the two different paths in the center, to be able to pull them to the surface of the ball [8]. These two cases are illustrated in Figure 2.2.

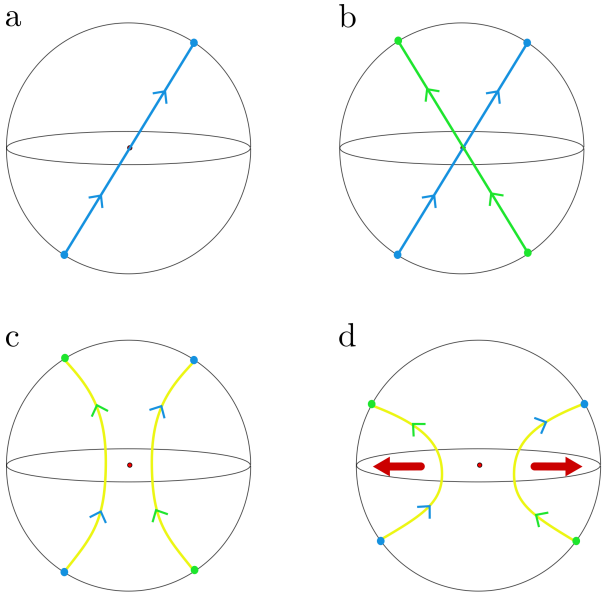

Figure 2.2.: Non-triviality of 2π-rotation vs. triviality of 4π-rotation: Panel (a) shows the 2π-rotation starting at the center of the ball (red dot), going up to the blue dot which is identified with the blue dot at the bottom, and continuing from there back to the center. The blue dots need to stay at antipodal positions, therefore, it is not possible to contract the loop to a point. Panel (b) shows again in blue a 2π-rotation and a second one in green so the total closed path is actually a 4π-rotation. In panel (c), we continuously deform the blue and green loops to the yellow path which is a single closed loop. Now, in panel (d), we simply pull out the yellow loop to the surface of the sphere (keeping the blue and green dots at antipodal positions) and are able to shrink it to a point (a constant path, i.e. no rotation).

2.2.2. Universal covering space of SO(3)

From the considerations in the last section, we can see that while $SO(3)$ is a connected space, it does not fulfill the stronger condition of being simply connected[4]. It is connected as the ball is just one piece, i.e. this means that it is not a union of disjoint non-empty sets. We can also see this from the fact that the ball is path-connected, i.e. there exists a path between any two points of the ball. But it is clearly not simply connected as we have just seen above with the 2π-rotation, which is a closed path that cannot be contracted to just a point. A different way to see this is the fundamental group. For rotations in $\mathbb{R}^3$ the fundamental group is $\Pi_1(SO(3)) = \mathbb{Z}_2$. The non-triviality of the fundamental group confirms that the space of rotations is not simply connected [8].

Now, we want to have a closer look at the universal cover of $SO(3)$. We know this cover exists as $SO(3)$ is a manifold and each manifold has a universal cover[5]. By looking at the cover, we preserve all local properties but include the non-triviality of the 2π-rotation. This universal cover will help us to find the fundamental group of the space M_3 classifying three-band models, as we know that the universal covering space is simply connected and we thereby will be able to apply Mermin's Theorem (Eq. 2.2.1).

First, we consider the covering space graphically (Figure 2.3). Yet instead of representing the rotations using one ball with antipodal points identified, we would now consider two balls and identify the same position on the different balls with each other. In the center of one ball we have identity, and the center of the other ball, we call the minus identity[6]. Using this setting the 2π-rotation connects the center of the first ball $(+\mathbb{1})$ with the center of the other ball $-\mathbb{1}$ and thereby clearly is non-trivial. Nevertheless, locally the two representations are the same, i.e. all rotations by an angle less than π can be represented using only the ball with center $+\mathbb{1}$.

We now have a closer look at paths corresponding to the 2π- and the 4π-rotations in such an augmented representation. Again, we start at the identity, following a direction $\boldsymbol{n}$ to the surface of the ball. However, this time, we then enter the other ball at the same point and follow the direction $-\boldsymbol{n}$ until arriving at the center of the second ball, i.e. at minus identity. We now can extend this to a 4π rotation. Therefore, we continue from minus identity along a possibly different direction $\boldsymbol{n}'$ to the surface of the second ball and re-enter the first ball at the corresponding position. From there we follow direction $-\boldsymbol{n}'$ back to plus identity. This representation of the rotation using two balls can also be interpreted as gluing the two balls together which results in a space that is isomorphic to S^3. Now from this isomorphism and the property that all paths on S^3 are contractible, we recover the fact that the 4π-rotation is trivial. Further, we know that S^3 has the same topology as $SU(2)$ with unitary matrices $\pm\mathbb{1}$ corresponding to a pair of maximally distant points. From this, we can see that $SU(2)$ is the double cover of $SO(3)$ and as it has trivial fundamental group, it is also its universal cover [8].

[4]This part is quite mathematical, the topological concepts are explained in Appendix A.

[5]The reason why is explained in Appendix A.4.

[6]This should not be confused with the inversion operator, which has a negative determinant and thus does not lie in $SO(3)$.

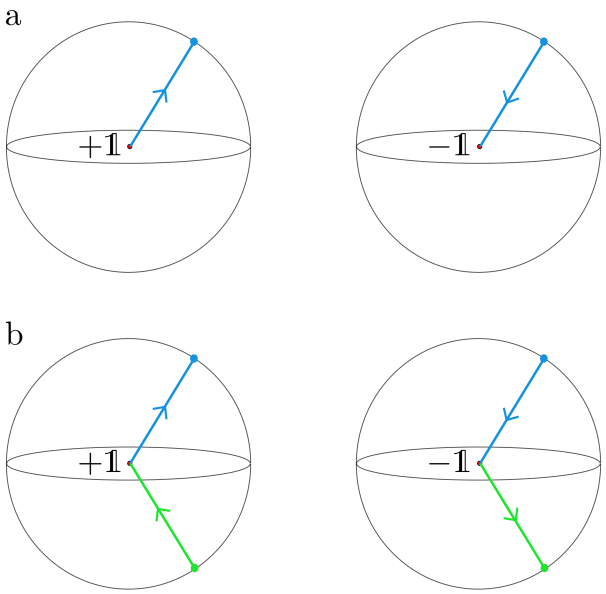

Figure 2.3.: Covering space of $SO(3)$: Panel (a) shows the 2π-rotation in the augmented two ball representation. We start at the identity in the left ball, go up to the blue dot identified with the blue dot on the other ball, and from there we go to the center of the second ball. Thereby, we end up at the minus identity. In panel (b), we have the 4π-rotation. We start a second 2π-rotation at the center of the right ball, leave this ball at the green dot and re-enter the left one to end up at plus identity.

We now describe explicitly the lift from $SO(3)$ to $SU(2)$ following Ref. [16]. Therefore, we need the generators of the groups. $SO(3)$ is generated by L_i with the properties that $(L_i)_{jk} = -\epsilon_{ijk}$ and the commutators therefore are $[L_i, L_j] = \epsilon_{ijk} L_k$ with ϵ the complete antisymmetric tensor. Using these, we can write every rotation as:

$$R(\alpha, \boldsymbol{n}) = \exp(-\alpha(n_1 L_1 + n_2 L_2 + n_3 L_3)) \tag{2.2.2}$$

or equivalently, we can describe the rotations using angles (α, β, γ) as:

$$R(\alpha, \beta, \gamma) = \exp(\alpha L_1 + \beta L_2 + \gamma L_3) \tag{2.2.3}$$

Similar representations, we can find for $SU(2)$-rotations. Here the generators are $S_i = -\frac{\mathrm{i}}{2}\sigma_i$ and the commutators are $[S_i, S_k] = \epsilon_{ijk} S_k$ with σ_i the Pauli matrices. The equivalence of the structure coefficients of $SO(3)$ and $SU(2)$ imply the local equivalence of the groups for elements close to the identity, as it was also the case for our one-ball and two-ball representations of rotations.

We again have two possibilities to represent the rotations using the rotation angle α and the rotation axis $\boldsymbol{n}$ or the three angles (α, β, γ).

$$R(\alpha, \boldsymbol{n}) = \exp\left(-\frac{\mathrm{i}}{2}\alpha \boldsymbol{n} \cdot \boldsymbol{\sigma}\right) \tag{2.2.4}$$

$$R(\alpha, \beta, \gamma) = \exp(\alpha S_1 + \beta S_2 + \gamma S_3) \tag{2.2.5}$$

So, we find two possible representations for the lift, either, by taking the formulas including three angles or the ones including the rotation angle and axis [8, 16].

2.3. Non-Abelian topological charge

We have now seen the quantization of the Berry phase for one-dimensional systems. Then we have specified our discussion to models including three isolated bands described by the space $M_3 = SO(3)/D_2$. By only using the Berry phase, we are not able to capture the non-triviality of the 2π-rotation as the Berry phase only includes sign flips, and for such a rotation all the signs stay the same.

These two observations motivate an extension of the Berry phase. Following the discussion above, we consider a model with three bands but the concept can also be generalized for $N \geq 3$ bands.

In a flattened three band model we can assign to each band a Berry phase of either 0 or π with the constraint that the sum of the Berry phases over all bands has to be 0 mod 2π. This leads to four possible phases for the system. If instead we consider the bands simultaneously as a right-handed frame, the Hamiltonian can be represented as a rotation of this frame and the topology is described by $\Pi_1(M_3)$. We now are able to determine this fundamental group explicitly by lifting both spaces $SO(3)$ and D_2 to their double covers and then use the theorem of Mermin (Equation 2.2.1). The lift of $SO(3)$ to its double cover is $Spin(3) \cong SU(2)$, which is also its universal cover and therefore has trivial fundamental group. The double cover of the dihedral group D_2 is its double group $\overline{D}_2$.

We can represent the gauge freedom (Berry phase 0 or π of each band with constraint that the sum over all Berry phases is 0 mod 2π) as a rotation of the eigenframe by $\pm\pi$ around one of the eigenstates. To get the double cover of D_2, we lift these π-rotations to $\mp\sigma_i$ and the identity to $\pm\mathbb{1}$. By assigning

$$\mathbb{1} \to 1 \quad -\mathrm{i}\sigma_1 \to \mathrm{i} \quad -\mathrm{i}\sigma_2 \to \mathrm{j} \quad -\mathrm{i}\sigma_3 \to \mathrm{k} \tag{2.3.1}$$

we see that the double cover of D_2 is isomorphic to the quaternion group:

$$Q = \{\pm 1, \pm \mathrm{i}, \pm \mathrm{j}, \pm \mathrm{k}\} \tag{2.3.2}$$

This is the group of anticommuting imaginary units $\mathrm{i}^2 = \mathrm{j}^2 = \mathrm{k}^2 = -1$.

So we find:

$$\Pi_1(M_3) = \Pi_1(SO(3)/D_2) = \Pi_1(SU(2)/Q) = \Pi_0(Q) = Q \tag{2.3.3}$$

Using this, we can assign to the system, instead of three Berry phases, one element of the quaternion group. The topological phases of the system are then described by the five conjugacy classes of the quaternion group $\{1\}, \{-1\}, \{\pm\mathrm{i}\}, \{\pm\mathrm{j}\}, \{\pm\mathrm{k}\}$. So, we find one additional topological phase (the one with quaternion charge -1 but all Berry

phases equal zero), compared to the four possible combinations of Berry phases (that are $(\pi, \pi, 0), (\pi, 0, \pi), (0, \pi, \pi), (0, 0, 0)$) summing to zero.

In Section 4.2, we generalize this charge to more bands and we discuss it in more detail. Thereby, we will focus on the interesting property that the charge is non-commutative. In general, we will be able to characterize bands of a one-dimensional system and band nodes of higher-dimensional systems using a non-Abelian charge, given as an element of the fundamental group of the parameter space M_N. As we have seen, in the case of three bands, this is the quaternion group and for more then three bands, we will call it the generalized quaternions [3, 14].

3. Edge states in 1D models

Before studying the non-Abelian charge in more detail for higher-dimensional systems, we consider three simple one-dimensional models. All of them consist of three flat bands but with different changes of the eigenstates when moving across the BZ. For simplicity and without loss of generality, we set the lattice constant a to unity in all models.

3.1. Elementary three-band models

We first consider the models presented in the Supplementary of Ref. [3]. That work presents two models with flat bands and studies their edge states. Starting from the simple Hamiltonian with energies $\{1, 2, 3\}$ and eigenstates represented in the reciprocal space as unit vectors, in x, y, z-direction, we generate an arbitrary Hamiltonian $\mathcal{H}(k)$ by a suitable (k-dependent) $SO(3)$ rotation of the eigenstates.

In the first model these three eigenvectors are rotated around one of the three axes, as a function of k. Throughout the BZ the eigenvectors are rotated by an angle π. Each of these rotations corresponds to a different topological quaternion charge. For the second model, we include a tuning parameter (angle) t to interpolate between the rotations around the x-axis and the z-axis, respectively. Here, throughout the BZ a rotation of 2π is maintained for all angles t. This corresponds to the topological charge -1, as we will calculate later. As a third model, we consider a rotation by 4π throughout the BZ. With this model we want to check if a 4π rotation exhibits a trivial spectrum as it corresponds to the trivial quaternion charge $+1$. Again we introduce a tuning parameter t, but now along t the rotation gets trivialized and for $t = \pi/2$ it ends up as the identity.

Mathematically, the models are defined as:

- Model 1: $\mathcal{H}_1^{x,y,z}(k) = R_1(k)\varepsilon R_1(k)^\dagger$, where we define:

$$\varepsilon = \begin{pmatrix} 1 & 0 & 0 \\ 0 & 2 & 0 \\ 0 & 0 & 3 \end{pmatrix} \quad \text{and} \quad R_1 = \exp^{kL_{x,y,z}/2} \tag{3.1.1}$$

- Model 2: $\mathcal{H}_2(k,t) = R_2(k,t)\varepsilon R_2(k,t)^\dagger$, where we define:

$$R_2(k,t) = \exp^{k[L_x\cos(t)+L_z\sin(t)]} \quad \text{for} \quad t \in \left[0, \frac{1}{2}\pi\right] \tag{3.1.2}$$

- Model 3: $\mathcal{H}_3(k,t) = R_3(k,t)\varepsilon R_3(k,t)^\dagger$, where we define:

$$R_3(k,t) = \exp^{\cos(t)\pi(\cos(k)L_y-\sin(k)L_z)} \quad \text{for} \quad t \in \left[0, \frac{1}{2}\pi\right] \tag{3.1.3}$$

To all models a perturbation $\mathcal{H}'(k) = \frac{1}{c}\sin(k)\mathbb{1}$ is added. The parameter c is adjusted to get sharper bulk states. This perturbation is needed to have bulk states of not exactly the same energy but to have a small dispersion such that the numerical computation with open boundary conditions is able to find eigenstates corresponding to certain momentum, and thus centered in the middle of a $1D$ chain, rather than an asymmetric linear combination of states originating from distinct momenta.

In a second step, after the Fourier transformation to the real space, a small Gaussian disorder was added to the on-site potential. We need this, in order to also have the edge states at slightly different energies, to find the physical edge state localized at only one edge rather than a superposition with a finite weight at both edges. This is done with a diagonal matrix having random Gaussian-distributed entries with mean $\mu = 0$ and standard deviation σ, chosen to get well localized edge states.

3.2. Computation of the topological invariants

In this section, we present the numerical techniques, we used to study the edge states of the one dimensional models. First, we explain how to transform the momentum-space Hamiltonian into a real-space one, and we present a method to visualize its edge states in the presence of an open boundary. Afterwards, we show the procedure how to numerically determine the Berry phase of an energy band using the corresponding edge state. As a last technique, we finally explain, how to calculate the quaternion charge of a one-dimensional system using the frame spanned by the three eigenstates of the Hamiltonian.

3.2.1. Transformation to real space

To be able to study edge states, we need a finite system. Therefore, we transfer the model to real space and choose a finite number of sites along the one-dimensional axis. To transform the Hamiltonian to the real space, each component of the Hamiltonian matrix is Fourier expanded in the following way:

$$\mathcal{H}_{\alpha\beta} = \sum_{n\in\mathbb{Z}} t^n_{\alpha\beta} \exp(\mathrm{i}kna) \tag{3.2.1}$$

where the lattice spacing a is set to unity, and $t^n_{\alpha\beta}$ represents the hopping amplitude by n sites ($n > 0$ to the right, $n < 0$ to the left) from orbital β to α. To get the Hermicity of the Hamiltonian $H^\dagger = H$, we need $\mathcal{H}_{\alpha\beta} = \mathcal{H}^*_{\beta\alpha}$, or in terms of the hopping parameters $t^n_{\alpha\beta} = (t^{-n}_{\beta\alpha})^*$.

The explanation for the procedure above can be motivated from the one-band model. There we find for a tight-binding Hamiltonian in real space with uniform hopping t^n by n sites the representation in reciprocal space as:

$$\mathcal{H}(k) = \sum_{n\in\mathbb{N}} [t^n \exp(\mathrm{i}kna) + (t^n)^* \exp(-\mathrm{i}kna)] \tag{3.2.2}$$

With this it is possible to set up the whole Hamiltonian matrix of the $1D$-system with N sites. The number of sites was set to 11 in the first model, and to 31 in the second and third one. As there are three orbitals a, b, c the matrix will be of dimension $3N \times 3N$.

This block matrix consists of N (number of sites) blocks t^0 on the diagonal, to the right (top) there follow the blocks $t^{-1}, t^{-2}, ...$ and to the left (bottom) the blocks $t^1, t^2, ...$ up to a cutoff n_0, above which the hopping amplitudes are negligible. In the first model, the blocks drop to zero beyond $n_0 = 1$, in the second model beyond $n_0 = 2$ (we will justify this in the Section 3.3.3 on the analytic solution) and in the third model beyond $n_0 = 4$. The components (α, β) of the blocks t^n are denoted by $t^n_{\alpha\beta}$. We thus represent the Hamiltonian as follows:

$$H = (c^\dagger_{1a}, c^\dagger_{1b}, c^\dagger_{1c}, c^\dagger_{2a}, \ldots, c^\dagger_{Nc}) \cdot \mathcal{H} \cdot (c_{1a}, c_{1b}, c_{1c}, c_{2a}, \ldots, c_{Nc})^T \tag{3.2.3}$$

$$\text{where} \qquad \mathcal{H} = \begin{pmatrix} t^0 & t^{-1} & t^{-2} & t^{-3} & \cdots \\ t^1 & t^0 & t^{-1} & t^{-2} & \ddots \\ t^2 & t^1 & t^0 & t^{-1} & \ddots \\ t^3 & t^2 & t^1 & t^0 & \ddots \\ \vdots & \ddots & \ddots & \ddots & \vdots \end{pmatrix} \tag{3.2.4}$$

and $c^\dagger_{n\alpha}$, $c_{n\alpha}$ are the electron creation and annihilation operators on site n in orbital α, respectively.

The three models are implemented in Python in reciprocal space (k-space) using the matrix form of the Hamiltonians (3.1.1, 3.1.2, 3.1.3). Then, the Fourier transform is done using a numerical integration tool in Python (complex version of the tool quad). The coefficients in the expansion (3.2.1) are given by:

$$t^n_{\alpha\beta} = \frac{1}{2\pi} \int_0^{2\pi} \mathcal{H}(k)_{\alpha\beta} \cdot \exp(\mathrm{i}nak) dk \tag{3.2.5}$$

The real space matrix is built as a block matrix and then diagonalized using the scipy.linalg package in Python. The output of the diagonalization are the eigenvalues and eigenvectors of the real-space Hamiltonian matrix.

The eigenenergies are found to be approximately $1, 2, 3$ for the bulk states, as expected. In the first model, in addition, there are states with eigenenergies $1.5, 2, 2.5$ for rotations around the z-,y-,x-axis, respectively, corresponding to edge states (compare Figure 3.2). For the second model the edge-state energies are found in the whole range between 1 and 3, depending on the angle t. A more intricate dependence of the edge states on t is observed for the third model which also vary in energy over the whole range between 1 and 3.

Having the energy spectrum that suggests the existence of edge states, we also want to check their localization properties. To do so we calculate the center of mass (COM) of each eigenstate. From the diagonalization, we get the eigenvectors. Physically, the components of these eigenvectors represent the probability amplitude for states being at a specific site in a specific orbital. So, we label the eigenvectors as: $v =$

$(v_{1a}, v_{1b}, v_{1c}, v_{2a}, \ldots, v_{Nc})$. Having these coefficients, we calculate the center of mass using the following formula:

$$x_{COM} = \sum_{i=0}^{N-1} \sum_{\alpha=a,b,c} r_{i\alpha} |v_{i\alpha}|^2 = \sum_{i=0}^{N-1} i \cdot \left(\sum_{\alpha=a,b,c} |v_{i\alpha}|^2 \right) \tag{3.2.6}$$

In the above equations $r_{i\alpha}$ corresponds to the positions of orbital α on site i. The second equality is valid because we assume that all three orbitals a, b, c are centered at the corresponding site.

We are now able to plot the center of mass of all states on the x-axis and the energy on the y-axis and can directly see the edge states and their energies. To better understand the correspondence between the edge states and the topological invariants, we now explain how to calculate the Berry phase and the quaternion charge

3.2.2. Computation of the Berry phase

From Section 2.1, we know that we can define the Berry phase for closed paths and that in the case of a one-dimensional system the BZ is such a closed path. So to calculate the Berry phase of one of the energy bands, we integrate its Berry connection over the whole BZ (Eq. 2.1.7). We find that:

$$\phi_B = \int_0^{\pi} A(k) dk \quad \text{with the Berry connection} \tag{3.2.7}$$

$$A = \mathrm{i} \langle u_n(k) | \partial_k | u_n(k) \rangle \tag{3.2.8}$$

where $|u_n(k)\rangle$ is the eigenvector of the band with index n with a gauge freedom $|u_n(k)\rangle \to e^{\mathrm{i}\xi} |u_n(k)\rangle$.

To evaluate the integral numerically, we have to partition our path into N points: $k_0, k_1, k_2, \ldots, k_{N-1}$ (Figure 3.1a). At each position, we find the eigenvector of the nth band as $|u_n(k_i)\rangle$ (possibly in a discontinuous gauge-see below). For large enough N, we apply the following formula for the Berry phase [17]:

$$\phi_B = \arg \left[\prod_{i=0}^{N-1} \langle u_n(k_i) | u_n(k_{i+1}) \rangle \right] \tag{3.2.9}$$

$$= \arg \left[\langle u_n(k_0) | u_n(k_{N-1}) \rangle \langle u_n(k_{N-1}) | u_n(k_{N-2}) \rangle \ldots \langle u_n(k_1) | u_n(k_0) \rangle \right] \tag{3.2.10}$$

with $k_N = k_0$. From this formula, we can see that for all the states except for the state $|u(k_0)\rangle$ the gauge cancels itself, i.e. we always find $e^{\mathrm{i}\xi_i} |u_n(k_i)\rangle \langle u_n(k_i)| e^{-\mathrm{i}\xi_i}$ which is the same as $|u_n(k_i)\rangle \langle u_n(k_i)|$. Therefore, we only have to choose $|u(k_0)\rangle$ at the beginning and the end of the closed path in the same gauge such that it cancels as well.

We can understand the last formula in the above equation from the point of view of parallel transport. Consider a vector $\boldsymbol{v}$ on a sphere (compare $\boldsymbol{e}$ in Figure 2.1) that is moved on a closed path on this sphere keeping its orientation. After going around the closed path we end up with a differently orientated vector $\boldsymbol{v}'$. This vector $\boldsymbol{v}'$, we now want to determine numerically. Therefore, we partition the path into N parts at the

points: $x_0, x_1, \ldots, x_{N-1}$. We find the final vector $\boldsymbol{v}'$ by projecting the initial vector $\boldsymbol{v}$ at each discrete point onto the tangent plane at this point, i.e. we find:

$$\boldsymbol{v}' = P(x_{n-1}) \ldots P(x_1) P(x_0) \boldsymbol{v} \tag{3.2.11}$$

where $P(x)$ is the projector onto the tangent plane at x. To get the anholonomy angle, we finally have to take the inverse cosine of the scalar product $\boldsymbol{v}' \cdot \boldsymbol{v}$.

By interpreting $|u_n(k_i)\rangle\langle u_n(k_i)|$ as the projector onto the state $|u_n(k_i)\rangle$, we see the analogy between the two formulas. In Equation (3.2.10), we take the initial state $|u_n(k_0)\rangle$, then project it onto the eigenstate at each point k_i to find the final state $|\tilde{u}_n(k_0)\rangle$ after going around the path. Finally to arrive at the Berry phase, we have to take the complex argument of the scalar product with the initial vector which due to the reality condition equals to 0 or π.

This procedure is easily implemented in Python to determine the Berry phase along any closed path. In the case of these one-dimensional topological insulators the closed path is always the BZ $[-\pi, \pi]$.

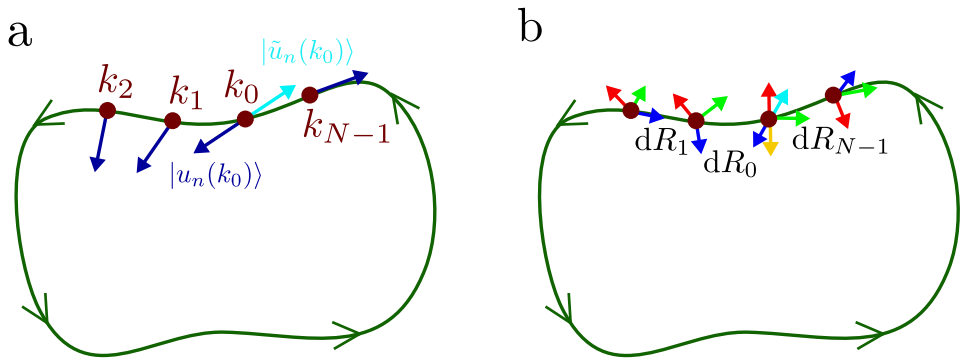

Figure 3.1.: Computation of the Berry phase and of the quaternion invariant. In panel (a), we see the partition of the path for the computation of the Berry phase as dark red dots. The blue arrows indicates the normalized eigenstate of the nth band at several locations along the path. At point k_0 we have drawn a second light blue arrow indicating the vector after moving around the path, having Berry phase of π. Panel (b) shows the computation of the quaternion invariant along the same path. At each k_i we see the frame of eigenstates as blue, red and green arrows, and between the discrete points we have an infinitesimal rotation $\mathrm{d}\boldsymbol{R}$. The light blue and yellow arrows show the final direction of the initial blue and red vectors at the same point. The green vector is the same after once going around the path, so this would represent a quaternion charge of i,j or k.

3.2.3. Computation of the quaternion charge

As a last technique, we now explain how to determine the quaternion invariant numerically. This is done similarly to the case just seen for the Berry phase but this time instead of only considering one eigenstate, we take the whole frame spanned by the three eigenstates.

The procedure to calculate the quaternion invariant along an arbitrary closed path γ consists of five steps (compare Supplementary material of Ref. [18] for the algorithm and Supplement of Ref. [3] for the idea):

i) Partition the path γ into short segments

ii) Find the infinitesimal rotation in $SO(3)$ between the frames at two neighboring discrete points k_i, k_{i+1}

iii) lift this $SO(3)$ rotation to an $SU(2)$ rotation close to identity

iv) multiply all the infinitesimal $SU(2)$ rotations, result is either $\pm\mathbb{1}$ or $\pm\mathrm{i}\sigma_i$

v) get the quaternion charge of the Hamiltonian with the correspondence between the quaternion charge and the Pauli matrices (Eq. 2.3.1)

We now have a closer look at all of these steps (compare Figure 3.1). Starting with a path γ in reciprocal space, which is either the BZ in the one-dimensional case or a thread through the BZ in the two- and three-dimensional case (see Sections 5.1.3 and 5.2.3). We first partition γ into N segments $[k_i, k_{i+1}]$ for the points $k_0, k_1, \ldots, k_{N-1}, k_N = k_0$. At each of these points we diagonalize the Hamiltonian to find the three eigenstates $|u_1(k_i)\rangle, |u_2(k_i)\rangle, |u_3(k_i)\rangle$ that span the frame $u(k_i) \in SO(3)$. We always chose this frame to be right handed, i.e. the third eigenstate $|u_3(k_i)\rangle$ has to be oriented parallel to the cross product $|u_1(k_i)\rangle \times |u_2(k_i)\rangle$.

For all segments $[k_i, k_{i+1}]$, we want to find the infinitesimal rotation $\mathrm{d}R_i$ the frame performs. This means, we search for $\mathrm{d}R_i$ such that $u(k_{i+1}) = \mathrm{d}R_i u(k_i)$. We see that $\mathrm{d}R_i = u(k_i)^T u(k_{i+1})$ by the orthonormality of $u(k_i)$. However, although we fixed the frames to be right-handed, we still have some gauge freedom and it is possible that two of the eigenstates changed their signs from k_i to k_{i+1}. Therefore, we need to check if the rotation is close to the identity and otherwise change the sing of two of the eigenstates at k_{i+1}, until we find $\mathrm{d}R_i$ to be close to the identity and thereby fix the gauge.

To lift the infinitesimal $SO(3)$ rotation to $SU(2)$, we first have to decompose it according to Equation (2.2.3). Therefore we take the logarithm of $\mathrm{d}R_i$ and decompose it as $\alpha L_1 + \beta L_2 + \gamma L_3$ to find α, β, γ. To get the lift of this rotation to $SU(2)$, we can use Equation (2.2.5) with the calculated values of α, β, γ, i.e. we find the lift as: $\overline{\mathrm{d}R_i} = \exp(\alpha S_1 + \beta S_2 + \gamma S_3)$.

Having determined the lifted small rotations, we can multiply all of them together and the result is a 2×2-matrix. Finally we decompose this matrix into the basis $\{\mathbb{1}, -\mathrm{i}\sigma_1, -\mathrm{i}\sigma_2, -\mathrm{i}\sigma_3\}$. In this decomposition, we have one parameter close to ± 1 and all the others close to zero (for large enough N). Using the isomorphism in Equation (2.3.1), we find the quaternion charge corresponding to the largest value in the decomposition.

This procedure is implemented in Python and can be applied to any real symmetric Hamiltonian along any closed path not passing a degeneracy (node). For the one-dimensional model we chose the path as the BZ, and in the higher-dimensional models we take the threads shown in Figure 5.5. Whereas for the $1D$ model, we get one quaternion charge describing the system (Section: 3.3.1), for higher dimensional models we find

the topological phase diagram inside the surface BZ, with projections of the bulk band nodes forming the boundaries between the different phases (Sections 5.1.3 and 5.2.3).

3.3. Results for the elementary three-band models

In this section, we present the numerical results we found for the one-dimensional models defined in Equations (3.1.1-3.1.3). We start with the calculation of the Berry phase and the quaternion invariant. Then, we show how these invariants are related to the edge states, and finally, we present an analytic solution for the first two models.

3.3.1. Quaternion charge and Berry phase

For all models, we can calculate the quaternion charge and the Berry phase. From the previous chapter, we know that for three-band models we have four possible phases, when considering the Berry phase, and five of them when using the quaternion charge for the topological characterization.

We implement the models in reciprocal space in Python to determine the Berry phase for each band separately as well as the quaternion charge for the system, numerically using the techniques presented in Sections 3.2.3 and 3.2.2. As we are considering the models in k-space, we do not need to include the perturbation $\mathcal{H}'$ for this calculation.

For the quaternion charge, we get the following results:

- π-rotation of the eigenstates around x-axis: charge i
- π-rotation of the eigenstates around y-axis: charge j
- π-rotation of the eigenstates around z-axis: charge k
- 2π-rotation of the eigenstates around axes interpolated between the x- and z-axis independent on interpolation angle t: charge -1
- 4π-rotation of the eigenstates in $\mathcal{H}_3$ for $t = 0$: charge 1
- No rotation of the eigenstates in $\mathcal{H}_3$ for $t = \frac{\pi}{2}$: charge 1

In general, the quaternion charge is only defined up to conjugacy classes, i.e. if we say a Hamiltonian has charge i, it means that it has either charge +i or $-$i depending on the (non-canonical) choice of the initial right-handed frame. However, the charges $+1$ and -1 describe different phases.

In the case of the Berry phase, we find a phase for each band. We label the bands $1, 2, 3$ from low energy to high energy. For the different models, we find the following phases:

- π-rotation of the eigenstates around x-axis: 0 for band 1 and π for bands 2 and 3
- π-rotation of the eigenstates around y-axis: 0 for band 2 and π for bands 1 and 3

- Rotation of the eigenstates around z-axis: 0 for band 3 and π for bands 1 and 2
- 2π-rotation of the eigenstates around axes interpolated between the x- and z-axis independent on interpolation angle t: 0 for all three bands
- 4π-rotation of the eigenstates contracted to identity along t: 0 for all three bands

So, we can assume the following correspondence between the Berry phases and the quaternion charge. Further, we directly relate the phases to our elementary models.

Elementary Hamiltonian	$\mathcal{H}_1^x$	$\mathcal{H}_1^y$	$\mathcal{H}_1^z$	$\mathcal{H}_2$	$\mathcal{H}_3$
Berry phase band 1	0	π	π	0	0
Berry phase band 2	π	0	π	0	0
Berry phase band 3	π	π	0	0	0
quaternion charge	i	j	k	-1	$+1$

Table 3.1.: The correspondence between the topological phases described by the Berry phases and by the quaternion charge, respectively. For $\mathcal{H}_2$ and $\mathcal{H}_3$ the values of the invariants are independent of the tunable parameter t.

The observed correspondence tells us that we are not able to detect the non-trivial phase with quaternion charge -1 by only considering the Berry phase.

3.3.2. Edge states

We are able to see the edge states for the different models by plotting the COM on the horizontal axis and the corresponding energies on the vertical axis. Some examples are found in the figures below. For all the plots the parameter for the perturbation $\mathcal{H}'$ was set to $c = 1/2000$ and the standard deviation of the Gaussian random distribution to $\sigma = 5 \cdot 10^{-7}$.

Model 1

Figure 3.2 shows the results for the first model using the three rotations around the x-,y- and z-axis, respectively. The edge states are very well localized and can be seen also if the edge state energy coincides with the energy of the bulk band, so they do not hybridize.

We can relate this observation to the quaternion charge. Comparing the results from the edge states for the different rotations with the results in Table 3.1, we can see that there is always an edge state produced in the middle between the two bands with non-zero Berry phase. In the case of the y-rotation, the energy of the edge state coincides with the energy of the middle band with Berry phase zero. In the language of the

quaternion charge, we can say that charge i produces edge states between the upper two bands and charge k produces them between the lower two bands. For the charge j it is not that obvious how to interpret it as from the rules of the quaternion group, we know that j is equal to $-\mathrm{i} \cdot \mathrm{k}$. So from the above picture, it is not clear if the edge states lie between the edge states corresponding to charges i and k, or simply between the lowest and highest energy band. This can be checked by adapting the model in a way that we change the diagonal matrix ε to have entries $1, 2, 4$, instead of $1, 2, 3$. In this adapted case, we find the edge states at 1.5, 2.5 and 3, which indicates that for charge j the edge state simply lies in the middle of the lowest and highest energy band.

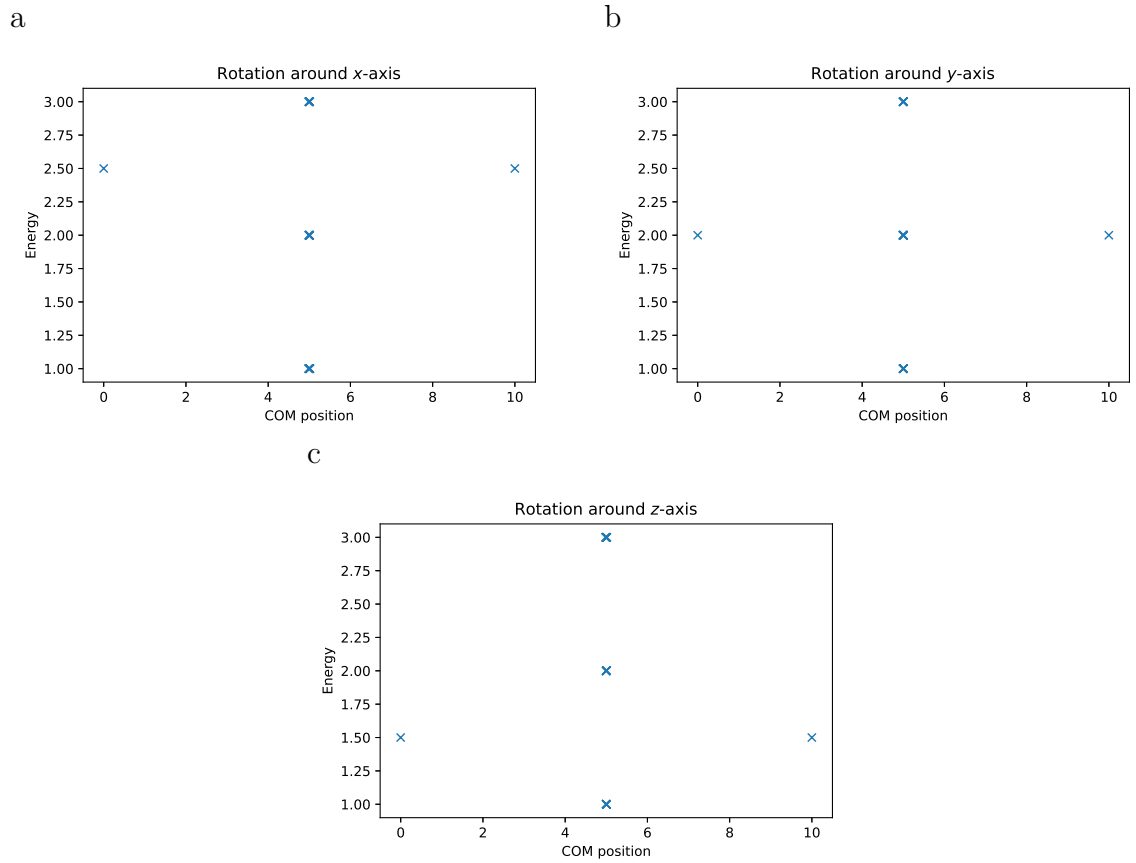

Figure 3.2.: Model 1: π-rotation around one axis for 11 sites. Panel (a) shows the rotation around the x-axis and we see at both edges of the system a very well localized edge state (localized on the outermost site) at an energy of 2.5. In panel (b), we have the rotation around the y-axis and in panel (c), the one around the z-axis. We again see well localized states at energies 2 and 1.5, respectively.

Model 2

The second model was implemented for the angles $t = \frac{m}{50}\pi$ with $m = 0, 1, 2, \ldots, 25$ and 31 sites. The results are shown in Figure 3.3. For $m = 0$ and $m = 25$, we have

nearly the same situation as in model 1 for the rotation around the x- and z-axis. The major difference is that we perform a 2π-rotation here, while in model 1 it was only a π-rotation. Correspondingly, we now find 2 edge states per edge at energies 1.5 and 2.5, respectively, but less localized than in model 1.[1]

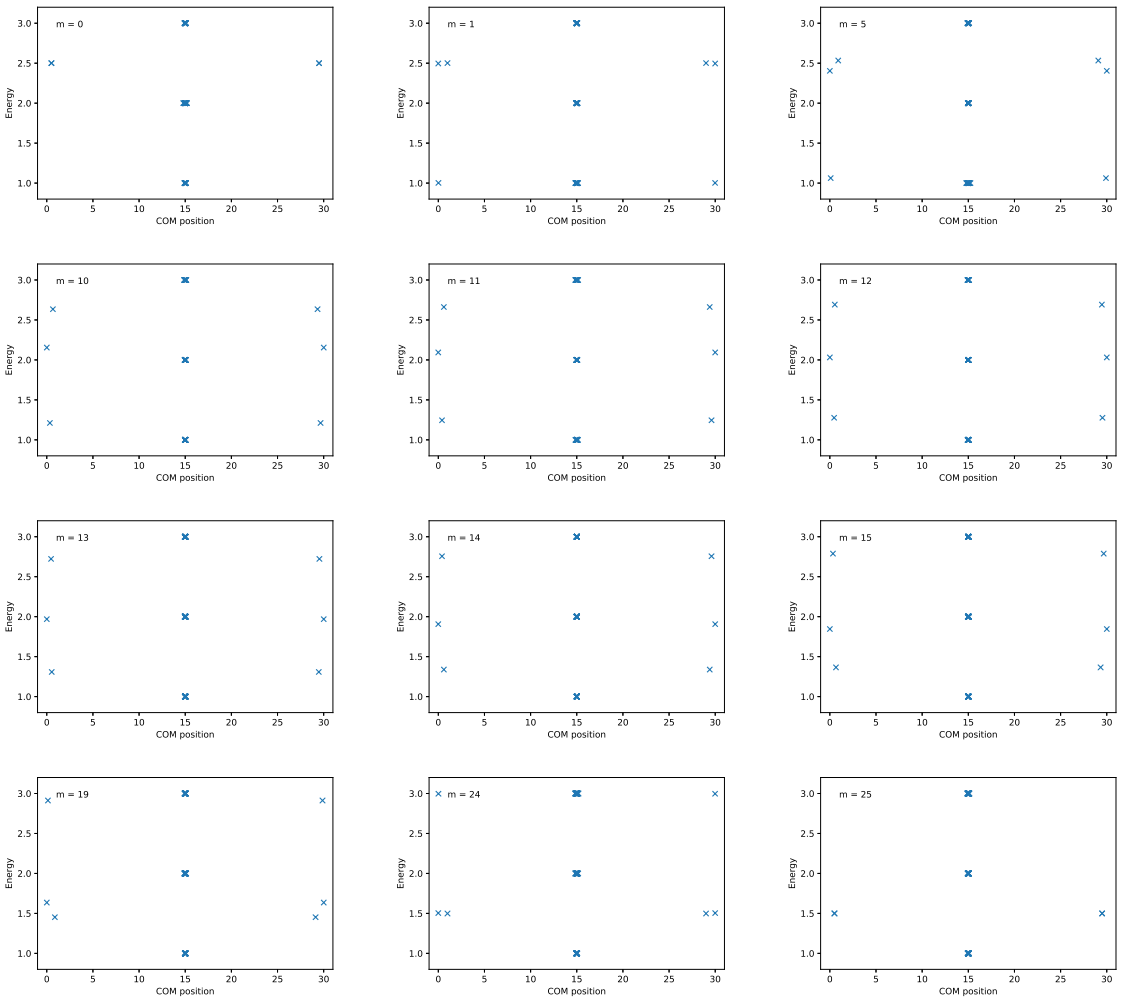

Figure 3.3.: Model 2: 2π-rotation for different angles t and 31 sites. Again we can see bulk states in the middle and edge states on the boundaries. This time the localization length, as well as the number of edge states on each edge, changes by tuning the angle $t = \frac{m}{50}\pi$. For $m = 0$ and 25 we see two edge states per edge localized at a position around 0.5 from the edge. In the other cases, we always have one state per site completely localized and two edge states per edge which change localization from completely to less localized respectively the other way round. All the six edge states (three per edge) change their energy in different ways.

As the pictures are symmetric in the two edges, we concentrate from now on only on

[1]This weaker localization is only a numerical artifact as explained later.

the states localized on the left edge. For $m = 1$, we see a third edge state appearing in the lower band gap at energy 1. Increasing m, one of the two edge states in the upper gap increases in energy while getting better localized while the other one crosses the middle band between $m = 12$ and $m = 13$ with localization length 0 throughout the whole process. The edge state in the lower band gap increases its energy and its localization length by growing m.

To better understand how the localization length and the energy behave as we tune the angle t, we plot them as a function of t (see Figure 3.4). We observe a cosine behavior of all the energies, as well as for the localization length of two of the edge states on each side. Only the edge state crossing the middle band has a localization length of zero during the whole process. Here, we see the left-right symmetry of the edge spectrum even better. The dots and crosses, representing the two edge states on the different sides, are exactly on top of each other. The finite localization length of 0.5 for the cases with $m = 0, 25$ can be explained as a numerical artifact of the hybridization of the two edge states per edge with exactly the same energy and localization lengths of 0 and 1, respectively. This is confirmed in the next section where we present the analytic solution with localization length of 0 also for these two cases.

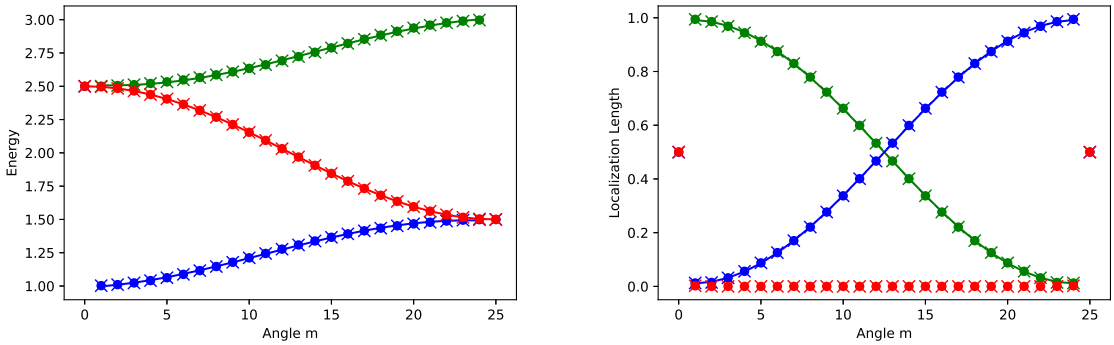

Figure 3.4.: Energy and localization length of the numerically identified edge states as a function of the angle t. The left panel shows the energy of the edge states depending on the angle $t = \frac{m}{50}\pi$. The dots and crosses indicate their energies and the lines show a cosine fit. In the right panel the same is shown for the localization length. For the red one, we show no fit as it has localization length zero throughout the process (up to a numerical artifact at $m = 0$ and 25).

As calculated in the previous section, we know that the Berry phases of all three bands are zero. This suggests a trivial phase with no edge states. However, considering the quaternion charge, we calculated a value of -1, which tells us that the phase is topologically non-trivial. From the properties of the quaternion group, we know that this is the square of any charge i, j or k. So, we would expect this phase to only have two edge states per edge but in the same band gap. However, we observe three of them and one might naively guess that only two of them are topological and the third one is

trivial, i.e. disappears by small perturbations. Looking at the extreme values of t, for $m = 0$, we only see the green and the red edge states whereas for $m = 25$ we observe the red and the blue one. Therefore, one cannot globally and meaningfully define which two out of these three edge states are the topological ones for the continuum of models spanned by the parameter t.

The interesting thing we observe, here, is that in this phase -1 one of the edge states passes through the middle band. We also observe this behavior for other models in higher dimensions (see Section 7.3).

Model 3

Finally, we study the model with the 4π rotation that is trivialized for $t = \pi/2$. The model was implemented for 31 sites and for different angles t. We want to see how do the edge states evolve during the contraction of the rotation to identity. But before studying the edge states, we have a closer look on how the rotation is trivialized.

Therefore, we consider the representation of $SO(3)$ as a ball with radius π. For $t = 0$ the rotation is represented as a circle on the surface of the ball going through the north and the south pole of the sphere in the $y - z$-plane for $x = 0$. Upon increasing t the circle shrinks while staying in the same plane. Like this we contract the circle to a point in the origin of the ball which represents the identity (Figure 3.5).

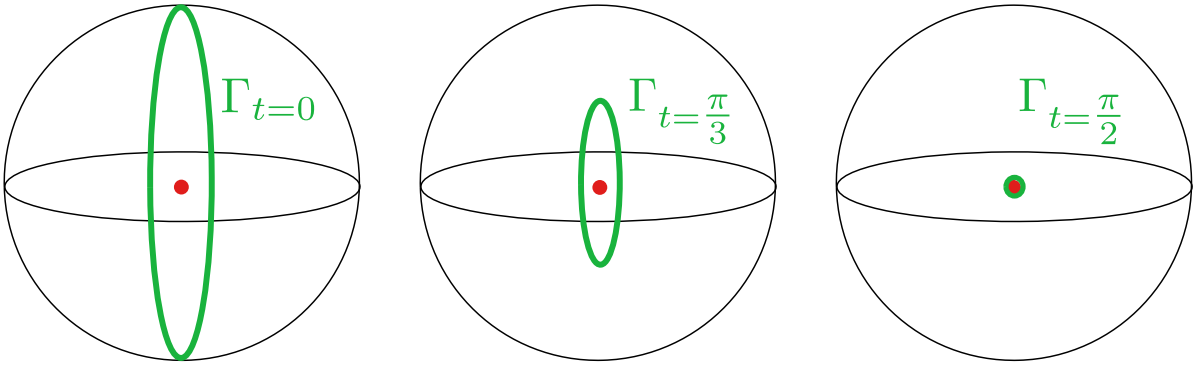

Figure 3.5.: Trivialization of the 4π-rotation. The green line shows the rotation $R_3(k, t)$ of the model $\mathcal{H}_3$ for different values of t represented using the a ball of radius π. For $t = 0$ the rotation is on the surface of the ball. When increasing t the rotation gets contracted towards the origin (red dot) for $t = \frac{\pi}{2}$.

Figure 3.6 shows the evolution during this process for the values $t = \frac{m}{50} \cdot \pi$ where m is indicated in the plots. For the 4π-rotation at $t = 0$, we see four edge states per site lying exactly on top of each other at energy 2.5. Then by increasing t a fifth edge state is ejected from the lowest band. From the upper four edge states two start increasing and the other two are decreasing in energy. For $t = \pi/4$ one state crosses the middle band and joins the fifth one in the lower band gap. Finally for $t = \pi/2$ all the edge states disappear.

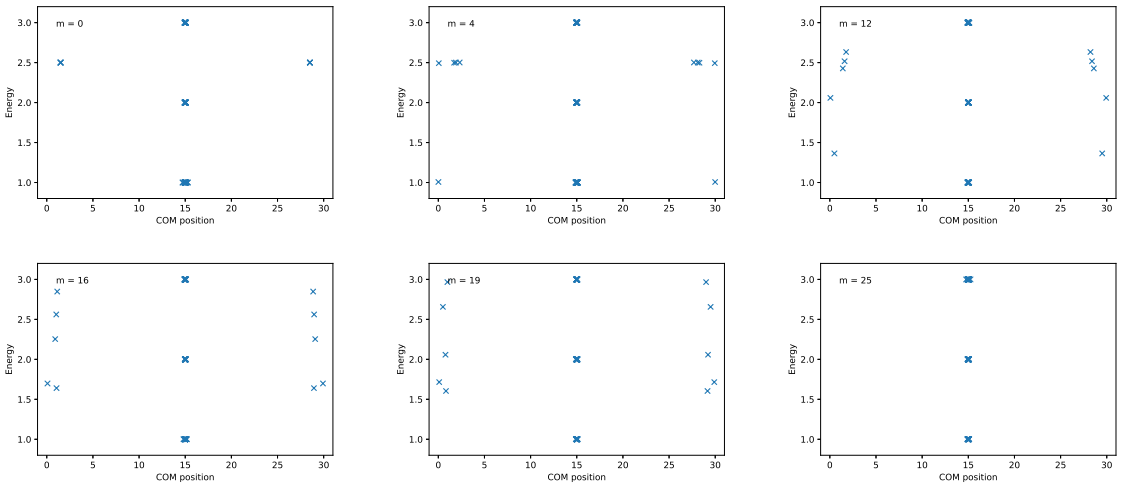

Figure 3.6.: Model 3: starting with a 4π-rotation that gets contracted to identity. In the middle we clearly see the bulk states, and on the edges we have a varying number of edge states. For $t = 0$, we find four edge states per end that lie exactly at the same position. Along the evolution for $t \in (0, \frac{\pi}{2})$, we observe five edge states per edge. In the end where the rotation is contracted to identity ($t = \pi/2$), all the edge states disappear.

To better see the behavior of the edge states depending on the parameter $t = \frac{m}{50} \cdot \pi$, we also plotted the energy of the edge states as well as their localization lengths as a function of m (Figure 3.7).

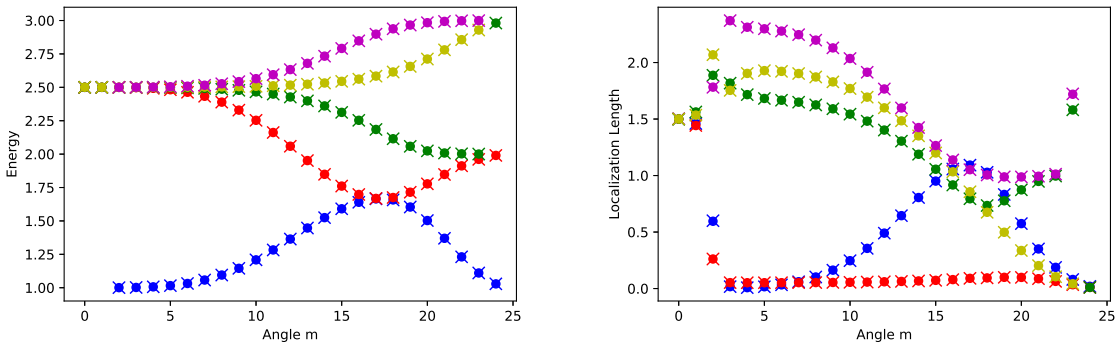

Figure 3.7.: Energy and localization length of the edge states as a function of the angle t for the 4π-rotation. The left panel shows the energy of the edge states depending on the angle $t = m/50\pi$. The dots and crosses indicate the numerically obtained energies from the two edges. In the right panel the same is shown for the localization length. For the value $m = 25$, we see that all edge states disappeared

Although a 4π rotation is trivial, we also observe edge states in this case but we suggest that these edge states are not topological, i.e. not stable against small perturbations.

Furthermore, along the process of this continuous trivialization of the 4π-rotation, we observe five edge states per edge and only for the trivial case where we do not perform any rotation, we observe no edge states.

Interesting along this trivialization is, that we can observe a degeneracy between the blue and the red edge states for $m \approx 17$ ($t \approx \frac{\pi}{3}$). At the moment it is unclear if this degeneracy is a purely accidental feature of our model, or if there is a deeper topological origin.

3.3.3. Analytic solution

The observed cosine dependence of the energy and the localization length on t in the second model suggests a possible simple analytic solution, depending on the angle t. In this section, we consider the first two Hamiltonians $\mathcal{H}_1, \mathcal{H}_2$ without the perturbation $\mathcal{H}'$. In this case, we can explicitly find the blocks t^n for the tight binding model in real space (Equation 3.2.4). We did not search for an analytic solution for the last model, as it includes too many blocks t_n.

Model 1

First, we consider the model $\mathcal{H}_1^{x,y,z}$, where the solution is much easier to find. Here, we only have nearest neighbor hopping. As the solutions for the three possible rotation axes are found in a similar way, we present the explicit solution only for the rotation around the x-axis, i.e. the Hamiltonian $\mathcal{H}_1^x$. We find the following blocks:

$$t^0 = \begin{pmatrix} 1 & 0 & 0 \\ 0 & 2.5 & 0 \\ 0 & 0 & 2.5 \end{pmatrix} \tag{3.3.1}$$

$$t^1 = \begin{pmatrix} 0 & 0 & 0 \\ 0 & -\frac{1}{4} & -\frac{1}{4}\mathrm{i} \\ 0 & -\frac{1}{4}\mathrm{i} & \frac{1}{4} \end{pmatrix} \qquad t^{-1} = \begin{pmatrix} 0 & 0 & 0 \\ 0 & -\frac{1}{4} & \frac{1}{4}\mathrm{i} \\ 0 & \frac{1}{4}\mathrm{i} & \frac{1}{4} \end{pmatrix} \tag{3.3.2}$$

So the matrix in real space becomes quite simple as the first band has energy 1 and is completely decoupled from the other two bands. Therefore we can ignore it and solve the system for the other two bands. In this way we easily find the edge states with energy 2.5 as:

$$v_{\text{edge},1} = (0, -\mathrm{i}, 1, 0, \ldots, 0) \tag{3.3.3}$$

$$v_{\text{edge},2} = (0, \ldots, 0, \mathrm{i}, 1) \tag{3.3.4}$$

where the number of zeros depends on the number of sites, we take for the finite system. From this, we can confirm that the edge states are really localized on the outermost site.

Model 2

The second model is a bit more complicated. First, we need to include the dependence on the angle t and second we not only have nearest neighbor hopping but also second nearest neighbor hopping, i.e. we also need to include the blocks t^2, t^{-2}. To find the hopping amplitude, we first have to write down the Hamiltonian as a single matrix and not a multiplication of them. Then, we write out all the $\sin(nk)$ and $\cos(nk)$ in terms of exponential functions. From this form, we can directly read out the hoppings in real space as the coefficients in front of the exponentials. For example a term $\frac{1}{8}\cos(2t)\left[\exp(2\mathrm{i}k) + \exp(-2\mathrm{i}k)\right]$ represents a hopping of $\frac{1}{8}\cos(2t)$ by 2 sites in positive and negative k-direction. Using this method[2], we find the following blocks:

$$t^0 = \begin{pmatrix} \frac{13}{8} - \frac{1}{4}\cos(2t) - \frac{3}{8}\cos(4t) & 0 & -\frac{3}{8}\sin(4t) \\ 0 & 2 + \frac{1}{2}\cos(2t) & 0 \\ -\frac{3}{8}\sin(4t) & 0 & \frac{19}{8} - \frac{1}{4}\cos(2t) + \frac{3}{8}\cos(4t) \end{pmatrix} \tag{3.3.5}$$

$$t^1 = \begin{pmatrix} \frac{1}{4}(-1+\cos(4t)) & -\frac{\mathrm{i}}{2}\sin(t)(1+\cos(2t)) & \frac{1}{4}\sin(4t) \\ -\frac{\mathrm{i}}{2}\sin(t)(1+\cos(2t)) & 0 & \frac{\mathrm{i}}{2}\cos(t)(-1+\cos(2t)) \\ \frac{1}{4}\sin(4t) & \frac{\mathrm{i}}{2}\cos(t)(-1+\cos(2t)) & \frac{1}{4}(1-\cos(4t)) \end{pmatrix} \tag{3.3.6}$$

$$t^2 = \begin{pmatrix} \frac{1}{16}(-1+2\cos(2t)-\cos(4t)) & \frac{\mathrm{i}}{4}\sin(t)\cos(2t) & -\frac{1}{16}\sin(4t) \\ \frac{\mathrm{i}}{4}\sin(t)\cos(2t) & -\frac{1}{4}\cos(2t) & -\frac{\mathrm{i}}{4}\cos(t)\cos(2t) \\ -\frac{1}{16}\sin(4t) & -\frac{\mathrm{i}}{4}\cos(t)\cos(2t) & \frac{1}{16}(1+2\cos(2t)+\cos(4t)) \end{pmatrix} \tag{3.3.7}$$

The remaining blocks are given as:

$$t^{-1} = (t^1)^* \qquad \text{and} \qquad t^{-2} = (t^2)^* \tag{3.3.8}$$

using the Hermicity of the Hamiltonian.

This time the real-space matrix becomes quite complicated and it is not possible to directly find the analytic solution. From the cosine fit in Figure 3.4, we are able to guess the energy of the edge state that crosses the middle band as:

$$E_{\text{edge state, red}} = 2 + \frac{1}{2}\cos(2t) \tag{3.3.9}$$

We know that if this is an eigenstate, the determinant of the matrix minus the eigenvalue on the diagonal has to be zero. We therefore define the Hamiltonian for 10 sites $\mathcal{H}_{10}$ which is a 30×30 matrix, and check using Mathemtatica that:

$$\det(\mathcal{H}_{10} - E_{\text{edge state, red}}\,\mathbb{1}) = 0 \tag{3.3.10}$$

which confirms that this is the correct energy for the edge state. To find the corresponding eigenstates, we look at the matrix $\mathcal{H}_{10} - (2 + \frac{1}{2}\cos(2t))\mathbb{1}$. Keeping in mind that Figure 3.4 further suggests that the state is localized at the outermost side, we take as

[2]We used Mathematica for the analytic calculations.

an Ansatz for the left edge state $v_{\text{edge},1} = (a, b, c, 0, \ldots, 0)$ and $v_{\text{edge},2} = (0, \ldots, 0, a', b', c')$ for the right one. Using again Mathematica, we can solve the following equations for $i = 1, 2$:

$$\mathcal{H}_{10} v_{\text{edge},i} = \left(2 + \frac{1}{2}\cos(2t)\right) v_{\text{edge},i} \tag{3.3.11}$$

and find the two edge states as:

$$v_{\text{edge},1} = \frac{1}{\sqrt{2}} (\sin(t), \mathrm{i}, -\cos(t), 0, \ldots, 0) \tag{3.3.12}$$

$$v_{\text{edge},2} = \frac{1}{\sqrt{2}} (0, \ldots, 0, \sin(t), -\mathrm{i}, -\cos(t)) \tag{3.3.13}$$

So, we see that the state is really localized completely at the edge.

From the numerical results, we know there are two more edge states. For them we were not able to find the analytic solution. The suggested solutions from the fits are:

$$E_{\text{edge state, blue}} = \frac{5}{4} - \frac{1}{4}\cos(2t) \qquad E_{\text{edge state, green}} = \frac{11}{4} - \frac{1}{4}\cos(2t) \tag{3.3.14}$$

But putting them into Equation (3.3.10) the analytic result for the determinant is not zero. Yet if we calculate the determinant numerical for different values of t it gets very close to zero. A possible reason for this could be that we work with quite small finite systems and that our guessed energies in Eq. (3.3.14) become exact only in the thermodynamic limit, i.e. if we let the number of sites go to infinity.

3.4. Models with four and more bands

We now focus on the non-Abelian charge -1 that is missed that is missed by the Berry phase. To study the stability of the topology and the edge states observed in this phase for three bands, we now extent the second model representing a 2π-rotation to $N \geq 3$ bands and start with the extension to four bands. With this generalized model, we then want to check if we still observe one edge state crossing the middle bands.

3.4.1. Ideal four-band model

We consider a model with four flat bands at energies $1, 2, 3, 4$. For this model, we rotate three eigenstates according to model 2 (Equation 3.1.2) letting the last eigenstate untouched. Therefore, we split the model into two parts. In the first part, we let the eigenstate of energy 1 constant while rotating the other three and in the second part, we let the one with energy 4 constant. This, we do using the Heaviside function $\theta(t)$ which is equal zero for $t \leq 0$ and equal 1 for $t > 0$. So, we define the model as:

$$\mathcal{H}_4(k,t) = \theta\left(\frac{1}{2}\pi - t\right) \mathcal{H}_{4,A}(k,t) + \theta\left(t - \frac{1}{2}\pi\right) \mathcal{H}_{4,B}\left(k, t - \frac{1}{2}\pi\right) \quad \text{for} \quad t \in [0, \pi] \tag{3.4.1}$$

$$\mathcal{H}_{4,i}(k,t) = R_i(k,t)\varepsilon R_i(k,t)^\dagger \quad \text{where} \quad \varepsilon = \begin{pmatrix} 1 & 0 & 0 & 0 \\ 0 & 2 & 0 & 0 \\ 0 & 0 & 3 & 0 \\ 0 & 0 & 0 & 4 \end{pmatrix} \tag{3.4.2}$$

for $i = A, B$. We define the rotations using $R_2(k,t)$ from Equation (3.1.2) as block matrices consisting of a 3×3 block ($R_2(k,t)$) and a 1×1 block (identity):

$$R_A(k,t) = \begin{pmatrix} 1 & 0 \\ 0 & R_2(k,t) \end{pmatrix} \qquad R_B(k,t) = \begin{pmatrix} R_2(k,t) & 0 \\ 0 & 1 \end{pmatrix} \tag{3.4.3}$$

With these definition the Hamiltonian in Equation (3.4.1) is well defined and continuous also for the angle $t = \pi/2$. At $t = \pi/2$ we have that $\mathcal{H}_{4,1}(k,t) = \mathcal{H}_{4,2}\left(k, t - \frac{1}{2}\pi\right)$ is simply the Hamiltonian with eigenvalues $1, 2, 3, 4$ and eigenvectors as the unit vectors along the axes of the four-dimensional space. We use the same perturbations introduced for the three-band model to find physical eigenstates for both the bulk and the edges.

The model is implemented in the same way as explained in Section 3.2. Also for this model, we find a Berry phase of zero for all four bands, what would suggest a trivial phase. Here, we cannot calculate the quaternion charge, as it is only defined for three bands but using the generalized non-Abelian charge proposed in Ref. [3] also for more than three bands, we would expect a topological phase analogous to the phase -1 here as well.

We used the same method as for three-band models to visualize the edge states. Therefore, we plotted the COM vs. energy for different angles $t = \frac{m}{25}\pi$ with $m = 0, \ldots, 25$ and for 31 sites.

We observe the same behavior as for three bands between $m = 0$ and $m = 12$ as well as between 13 and 25. Between 12 and 13, i.e. for $t = \pi/2$, we would again have a situation with only two edge states per site, as for $m = 0$ and 25, but with an energy of 2.5. For most of the angles, we observe again three edge states per site. Always two of them in the same band gap and a third one in a neighboring one. Such a behavior is not surprising, as we simply added a fourth trivial band. First, we observe an additional bulk band at energy 1 and in the second part at energy 4 whereas the other three band show the behavior of model 2. More clearly, we see this by looking at the energy and localization lengths as a function of the angle $t = \frac{m}{25}\pi$. It is really just a stacking of twice the situation shown in Figure 3.4 where in the plot of the energy vs. the angle for one half the energies are shifted by 1.

As expected, we again observe a non-trivial topological phase although all the Berry phases are zero. Furthermore, the red edge state crosses two energy bands to evolve from the highest to the lowest band gap with a localization lengths of zero throughout the whole process, similar to the observation for the three-band model. These results suggest that we could extend our model in this way to any $N \geq 3$ bands, and we would always observe one edge state per edge moving uppermost to the lowest band gap with a localization lengths of zero and thereby crossing all the middle bands .

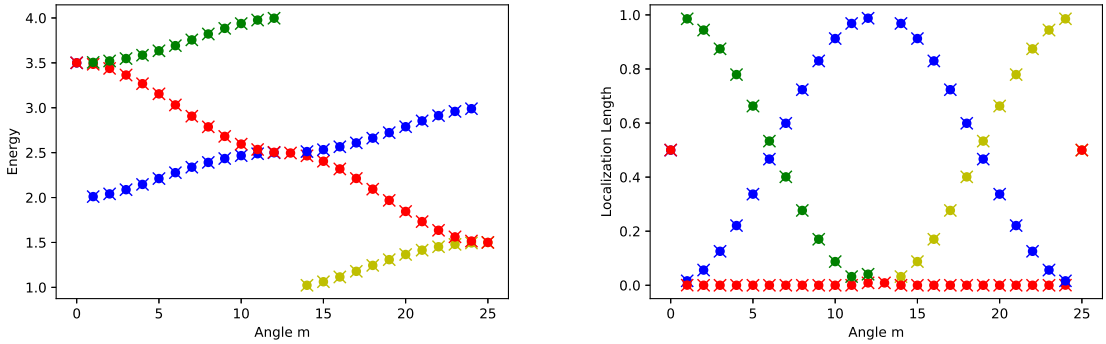

Figure 3.8.: Energy and localization length of the edge states as a function of the angle t in the model with 4 bands (Eq. 3.4.1). The left panel shows the energy of the edge states depending on the angle $t = \frac{m}{25}\pi$. The dots and crosses indicate the numerically obtained energies for the different edges. In the right panel the same is shown for the localization length.

As a last step concerning the one-dimensional models, we have a look at how the states are distributed among the bulk bands. More specifically, we study how edge states are pumped between the bulk bands in the generalized "-1" phase, and the possible associated filling anomaly. Therefore, we extend our models to an arbitrary number of bands.

3.4.2. Generalization to N bands

We now consider a model with N bands similar to the one constructed for four bands in Eq. (3.4.1). It consists of N flat bands with energies $\varepsilon = 1, 2, \ldots, N$ and eigenstates v_i as unit vectors of the N-dimensional space (eigenstate v_i corresponding to energy $\varepsilon_i = i$). We then start by rotating the eigenstates corresponding to the highest three energies according to $R_2(k,t)$ in $\mathcal{H}_2$, then continue with the eigenstates $v_{N-3}, v_{N-2}, v_{N-1}$ and so on. In total, we apply the elementary model $\mathcal{H}_2$ $(N-2)$ times, the last time for eigenstates v_3, v_2, v_1.

This model is in fact an interpolation between $(N-2)$ ideal realizations of the phase with non-Abelian charge -1 where we take $\mathcal{H}_2$ as the elementary building block for the interpolations. By "ideal" realization, we mean that we perform a 2π-rotation[3] of the eigenstates of two consecutive bands while leaving the other $(N-2)$ eigenstates constant across the BZ. We first rotate the two states corresponding to the highest energies, interpolate to a rotation of the second and third highest, until we end up with a rotation between the states corresponding to the lowest two energies.

[3]This 2π-rotation remains non-trivial also in the higher-dimensional space of rotations $SO(N)$ that we need for the generalized non-Abelian charge, analyzed in Section 4.2.

3.4.3. Pumping of edge states and filling anomaly

For the model with N bands presented above, we are able to count the states in each bulk band. At the beginning we have $(N-2)$ states in each of the highest two bulk bands and 4 states in the uppermost band gap, whereas all other bulk bands host N states. Two of the edge states merge into the highest band during the interpolation whereas the other two cross the second highest band and end up in the second uppermost band gap. So, we have $(N-2)$ bulk states in the second and in third highest bands, and 4 edge states in the second uppermost band gap and N bulk states in all other bands. In fact with each such performed cycle (interpolation of two ideal realization), we pump two edge states down by one band gap. So after $N-2$ cycles we did pump two edge states from the uppermost to the lowest band gap. This pumping[4] of edge states between bulk bands in the phase -1 could lead to additional future insights into the band topology of such systems[5].

We finally study the possible presence of filling anomaly in the (generalized) -1 phase. Filling anomaly associated with a topological band means the impossibility to simultaneously (i) be at integer filling, and (ii) respect the symmetry of the system. Condition (ii) is sometimes replaced by the presence of zero-energy excitation. Since in our models the topological edge states are distributed over several band gaps, one could generalize filling anomaly to the impossibility to fulfill (i) and (ii) for at least one integer filling fraction [21].

To study this filling anomaly, we now look at the chemical potential for filling fractions $\nu = 1/N, 2/N, \ldots, (N-1)/N$ which correspond to an integer number of electrons per unit cell. For these fillings, we look where the chemical potential lies and if we find gapless excitations. We first look at filling $\nu = (N-1)/N$ for the situation where we perform the rotation of model 2 for the eigenstates of the uppermost three bands. During the whole interpolation we have the chemical potential in the middle of the band gap at $\nu = (2N-1)/2$ but only for the angle $t = 0$ we have a gapless excitation. The same is true for all other interpolations between two ideal realizations. Thus, we have gapless excitation for some of the considered filling fractions only in the case of the ideal realization of the phase with charge -1. In general, for a filling $\nu = (2i+1)/2$, we have a gapless excitation if we perform a 2π-rotation of the bands i and $i+1$. Therefore, we conclude that for the phase -1, in general, we do not observe a filling anomaly, except we consider an ideal realization of the N-band model. However, we do observe the filling anomaly for the first model $\mathcal{H}_1$ which has a non-zero Berry phase for two of the energy bands.

[4] Such pumping of states related to topology was first mentioned by Laughlin [19], but he referred to a pumping of states across the so-called Corbino disc, i.e. in space, whereas here we pump the states in energy.

[5] In our model, we only pump one edge states from the highest to the lowest band gap. Using periodically driven systems, so-called Floquet systems, it could be possible to perform a full closed cycle, by pumping the edge state around a quasi-energy circle [20].

4. $\mathcal{PT}$-symmetric topology in higher dimensions

In this chapter, we look at topological semimetals in higher dimensions. Band nodes of such semimetals are described by topological invariants. We mainly concentrate on $\mathcal{PT}$-symmetric systems, which generally exhibit band nodes of codimension 2, i.e. we look at point nodes in $2D$ and line nodes in $3D$ [22]. We discuss the generalization of the previously introduced non-Abelian invariant to arbitrary many $N \geq 3$ bands, and apply it to $\mathcal{PT}$-symmetric semimetals in two and three dimensions. Thereby we focus on the non-commutativity and its implications. Our discussion of these topics reviews Refs. [3, 23]. We also present several further $\mathcal{PT}$-protected topological properties and analyze them using the non-Abelian charge. At the end of the section, we postulate certain open questions related to the topology of the $\mathcal{PT}$-symmetric semimetals, which are addressed in the remainder of the work..

4.1. Topological semimetals

In the previous two chapters, we had a closer look at topological insulators in one dimension. We now extend the introduced concepts to topological semimetals. A semimetal in general is defined as a system where the conduction and the valence band are degenerate at some momenta $k \in \mathrm{BZ}$. Such a semimetal is called topological if it is robust against perturbations that do not break symmetries. In general, we do not need symmetries to produce stable band crossings, but the presence of a symmetry has an impact on the type of the expected band nodes (through their codimension)[22].

There are different types of topological semimetals. On the one hand, we can have points nodes, i.e. the bands cross each other at points. Such systems are called Dirac- or Weyl-semimetals. In contrast, we can also have nodal lines. These are band crossing along a curve inside the BZ. A nodal line can either be a closed curve inside the BZ, or it could extend and wind around the BZ torus in a periodic way and thereby be closed as well. Such systems are called nodal-line semimetals. We now want to see, how such nodes can be characterized by topological invariants [24].

In Section 2.1, we introduced the Berry phase to characterize bands in a one-dimensional $\mathcal{PT}$-symmetric topological insulators. Similarly, for two-dimensional topological insulators without $\mathcal{PT}$-symmetry, one can define an integer topological invariant called the Chern number, that is assigned to the two-dimensional energy band of the insulator. The Chern number is defined as the integration of the Berry curvature $\boldsymbol{F}$ (defined in

Eq. 2.1.11) over the two dimensional BZ M), i.e.

$$c = \frac{1}{2\pi} \oint_M \boldsymbol{F} \mathrm{d}\boldsymbol{S} \tag{4.1.1}$$

[25]. These two topological invariants describing bands in an insulator can be extended to characterize nodes in semimetals. This is achieved by enclosing the nodes with a closed loop or a closed surface (illustration in Figure 4.1). Enclosing a nodal point in $2D$ or a nodal line in $3D$ with a closed loop, we assign to it a Berry phase by integrating the Berry connection along this loop (Eq. 2.1.7 with $\mathcal{C}$ the closed loop). On the other hand, we can enclose a nodal point in $3D$ by a closed surface and assign to it a Chern number by integrating the Berry curvature over this surface (Eq. 4.1.1 with M the enclosing surface).

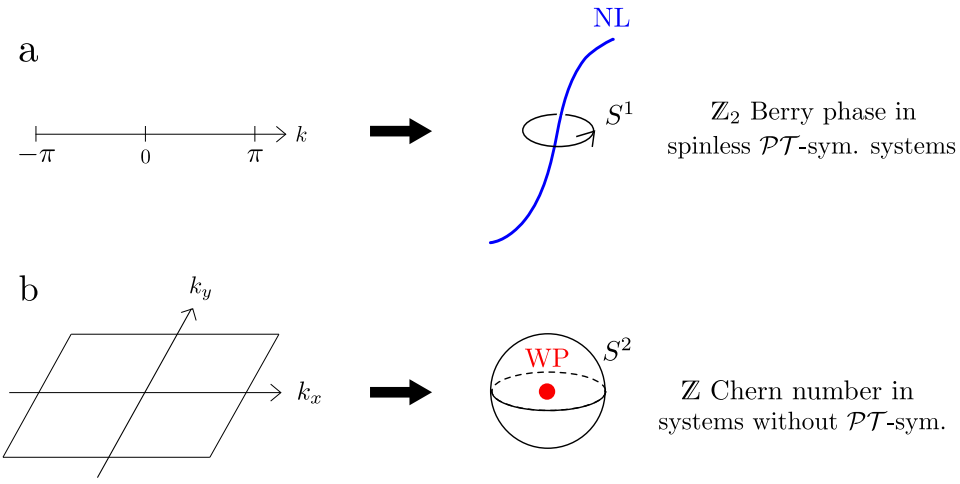

Figure 4.1.: Generalization of topological invariants from topological insulators to topological semimetals. Panel (a) shows on the left the path through the BZ to define the Berry phase for one-dimensional topological insulator. On the right the path to define the Berry phase of a nodal line (NL) is shown. In Panel (b) we present an analogous construction with the Chern number. The left part shows the BZ as the closed surface where the Chern number is defined. On the right is the generalization for Weyl points (WP) in $3D$ that are enclosed by a sphere.

To see this construction in action, we now have a look at two examples. First, we recall the case of single-layer graphene. This is an example of a two-dimensional $\mathcal{PT}$-symmetric system with point nodes. Graphene is well known to have a spectrum with Dirac cones meeting at so-called Dirac point nodes. By the concept explained above we can enclose these Dirac points by a tiny circle and determine the Berry phase around these circles. For graphene the Berry phase is quantized to 0 or π on any path, and reaches the value of π for paths enclosing one of the two Dirac point nodes [26].

The second example, we consider, are Weyl semimetals. These are three-dimensional systems with broken $\mathcal{PT}$-symmetry. Such Weyl-points, i.e. nodal points in $3D$, can be

enclosed by a tiny sphere. We then characterize the nodes by determining the Chern number over this sphere. The Chern number of Weyl-points is quantized to integers, and the sum of the Chern number of all Weyl-points has to vanish, which is known as the Nielsen-Ninomiya doubling theorem [27, 28]. Now, we have seen two examples of nodal points with present or broken $\mathcal{PT}$-symmetry characterized by the Berry phase and the Chern number, respectively.

In this work, we focus on semimetals with $\mathcal{PT}$-symmetry and negligible spin orbit coupling, which exhibit point nodes in $2D$ and line nodes in $3D$. These nodes can be described using the Berry phase and are thereby the natural extension of the one-dimensional $\mathcal{PT}$-symmetric topological insulators discussed in the previous two chapters. Following the construction in Figure 4.1, we see that in $2D$, as well as in $3D$, we can enclose the node by a tiny circle and assign to it a topological charge[1]. This observation motivates the extension of the non-Abelian charge defined for $\mathcal{PT}$-symmetric insulators to describe nodal points and nodal lines in higher dimensions. We want to see what one can learn about the nodes from the perspective of the non-Abelian topological invariant. Therefore, we consider the general case of N bands and we use again the fact that topological obstructions can be described using elements of the fundamental group of the order-parameter space [3].

4.2. Non-Abelian charge

In this section, we give a rigorous introduction to the non-Abelian charge for systems with $N \geq 3$ bands following Ref. [3]. We first give a quite mathematical definition, then we present some constraints on nodal line composition, and finally introduce the interesting property of the braiding of nodal points and the linking of nodal lines.

4.2.1. Mathematical definition

We want to define a topological invariant to describe nodal points (NP) and nodal lines (NL) in semimetals. Therefore, we start by introducing a convenient way to characterize nodes. This is done by looking at the Hamiltonian on a manifold around the node. For semimetals the nodes we are interested in occur between the valence (highest occupied) and the conduction (lowest unoccupied) band. With the restriction of $\mathcal{PT}$-symmetry and negligible spin-orbit coupling our Hamiltonian is real and we can always find the eigenstates to span a real orthonormal basis of the Hilbert space. We now consider a Hamiltonian with N bands from which n are occupied and $l = N - n$ are unoccupied. For $1 \leq j \leq N$ we find its eigenstates as $|u^j_{\boldsymbol{k}}\rangle$ and for $i < j$ we have eigenenergies $\varepsilon_i \leq \varepsilon_j$. The set of nodes we want to characterize is given by: $\mathcal{N}_{\mathcal{H}} = \{\boldsymbol{k} \in \mathrm{BZ} | \varepsilon^n_{\boldsymbol{k}} = \varepsilon^{n+1}_{\boldsymbol{k}}\}$. We do

[1] We can see the similarity between nodal points in $2D$ and nodal lines in $3D$ if we consider the $3D$ case as world lines of the $2D$ case. This means that we interpret the third momentum component as the time such that we end up with a $2D$ case evolving in time. We consider such a model consisting of point nodes extended to world lines in Section 5.1.

not change the topology of the Hamiltonian if we set the energies of all occupied bands to -1 and the ones of all unoccupied bands to $+1$ for all $\boldsymbol{k} \notin \mathcal{N}_{\mathcal{H}}$. We thereby end up with a simple Hamiltonian for all momenta not in the set $\mathcal{N}_{\mathcal{H}}$.

$$\mathcal{H}_{(n,l)} = -\sum_{j=1}^{n} |u_{\boldsymbol{k}}^j\rangle\langle u_{\boldsymbol{k}}^j| + \sum_{j=n+1}^{n+l} |u_{\boldsymbol{k}}^j\rangle\langle u_{\boldsymbol{k}}^j| \tag{4.2.1}$$

The restriction to momenta $\boldsymbol{k}$ that are not nodes is no problem as we define the topological invariant of the node on a manifold around the node, where the above Hamiltonian is well-defined.

We are interested in the order-parameter space $M_{(n,l)}$ of such spectrally flattened Hamiltonians, in particular in the fundamental group of this space, as we already know that we can assign an element of this group to each node.

From Equation (4.2.1), we see that the Hamiltonian is defined by a frame consisting of N orthonormal N-component vectors and is invariant under mixing the n first or the l last vectors. Therefore, we find the parameter space as a quotient space:

$$M_{(n,l)} = O(n+l)/O(n) \times O(l) \tag{4.2.2}$$

called the real Grassmanian. We can find its fundamental group in the Supplementary of [3] as:

$$\Pi_1(M_{(n,l)}) = \begin{cases} \mathbb{Z} & \text{for } n = l = 1 \\ \mathbb{Z}_2 & \text{for } n + l \geq 3 \end{cases} \tag{4.2.3}$$

Using this characterization, we see that for three or more bands there are two values of the topological invariant to assign to a path. More precisely, the Hamiltonian on any closed path γ is either trivial or non-trivial, in the latter case the path encloses a node.

In Chapter 2 we have seen that the Berry phase describes a single energy band, whereas the non-Abelian charge characterizes the system consisting of all three energy bands. In analogy to this one-dimensional description, we now also want to generalize this characterization of the nodes in one band gap to a situation where we consider all band gaps at once as a system.

To do so we consider models with $N \geq 3$ bands, eigenstates $|u_{\boldsymbol{k}}^j\rangle$ for $1 \leq j \leq N$ and energies $\varepsilon_i \leq \varepsilon_j$ for $i < j$. We now have a set of nodes for each band gap defined as $\mathcal{N}_{\mathcal{H}}^j = \{\boldsymbol{k} \in \mathrm{BZ} | \varepsilon_{\boldsymbol{k}}^j = \varepsilon_{\boldsymbol{k}}^{j+1}\}$ and the total set of nodes is then given by $\mathcal{N}_{\mathcal{H}} = \bigcup_{j=1}^{N-1} \mathcal{N}_{\mathcal{H}}^j$. For all $\boldsymbol{k}$ not in the set of nodes, we then simplify the Hamiltonian without changing its topology by setting the energies to $\varepsilon_j = j$. The resulting Hamiltonian looks as follows:

$$\mathcal{H}_N(\boldsymbol{k}) = \sum_{j=1}^{N} j |u_{\boldsymbol{k}}^j\rangle\langle u_{\boldsymbol{k}}^j| \tag{4.2.4}$$

This spectrally flattened Hamiltonian is defined by the orthonormal frame $\{|u_{\boldsymbol{k}}^j\rangle\}_{j=1}^N$ consisting of N-component vectors with gauge freedom $|u_{\boldsymbol{k}}^j\rangle \to -|u_{\boldsymbol{k}}^j\rangle$. Using this we can define the order parameter space of N-band Hamiltonians M_N as orthonormal frames

$O(N)$ modulo a multiplication of any eigenstate by ± 1, i.e. the group $O(1)$ for each eigenstate. This represents the gauge degree of freedom while preserving reality of the eigenstates. To simplify, we can restrict the frames to be right-handed, so we find the order parameter space to be the group $SO(N)$ modulo π-rotations flipping the sign of an even number of $|u^j_{\boldsymbol{k}}\rangle$ (flip of only one would lead to a left-handed frame).

From Section 2.3, we already know that for three bands we have $M_3 = SO(3)/D_2$ and $\Pi_1(M_3) = Q$. We are now looking for a generalization of this. More specifically, we are looking for a description of the group switching an even number of signs of the vectors $|u^j_{\boldsymbol{k}}\rangle^N_{j=1}$. Therefore, we define the Abelian group $P_{Nh} \equiv O(1)^N$ generated by reflection with respect to N mutually perpendicular axes in N-dimensional Euclidean space and P_N as the special component of it (to stay with right-handed frames), by taking only the elements with positive determinant. We arrive at the quotient space:

$$M_N = O(N)/O(1)^N = SO(N)/P_N \tag{4.2.5}$$

To compute the fundamental group of this space, we again want to use the theorem of Mermin (Equation 2.2.1). As in the case of three bands, we can do this by taking $Spin(N)$, the double (and also universal) cover of $SO(N)$. Now, we also need the double cover of P_N denoted by $\bar{P}_N$. So by Mermin's theorem we find that:

$$\Pi_1(M_N) = \Pi_1(Spin(N)/\overline{P}_N) = \Pi_0(\bar{P}_N) = \bar{P}_N \tag{4.2.6}$$

The group $\bar{P}_N$ is known as the Salingaros vee group and it is non-Abelian for $N \geq 3$. For a mathematical description consider the Supplement of Ref. [3].

Similar to the quaternion group discussed for three bands, the generators of the Salingaros vee group anticommute and square to -1, so they can be expressed using the real Clifford algebra $\mathcal{C}l_{0,N-1}$. We go into more detail on what the elements of the group describe in Section 4.2.3.

We now have a look at the number of conjugacy classes of this group, as we will see in the Section 4.2.2 that the nodes of a semimetal can be described by conjugacy classes of this group. It was shown by [3] that in the case of an odd number of bands, we find $2^{N-1} + 1$ conjugacy classes and for an even number we have $2^{N-1} + 2$ conjugacy classes.

We now look at the number of different topological phases in N-band models. In the one-dimensional case for the quaternion group, we have already seen that we find four phases by considering the Berry phase but five phases when using the quaternion charge for the characterization. This can be generalized for $1D$-system consisting of N bands. We know that we can assign to each band either a Berry phase of 0 or π with the constraint that the sum over all Berry phases is equal 0 mod π [12], leading to 2^{N-1} possible phases. Considering instead the non-Abelian charge that assigns an conjugacy class of the group $\bar{P}_N$ to the system, we find one or two additional phases depending on whether the number of bands is even or odd. Therefore, in general we can observe more topological phases characterized by the non-Abelian charge compared to the Berry phase. The relevance of the non-Abelian charge for the characterization of nodes is further discussed in Section 4.3.

4.2.2. The role of conjugacy classes

As already mentioned, we now argue why the characterization of nodes can only be done up to conjugacy. Therefore, we consider first the two-dimensional case and then extend it to $3D$ using world lines.

In general, we assign a charge to a nodal point by taking a loop that starts at a base point X_0, then winds around the node and finally ends up at the base point again. So, we have a closed curve along which we calculate the topological charge, we assign to the node. The Hamiltonian along the path can be interpreted as a $1D$-system, similar to those analyzed in Chapter 3. It is important that we only enclose one node with our loop. We now look at a specific example and explain why we can only assign the charge up to conjugacy.

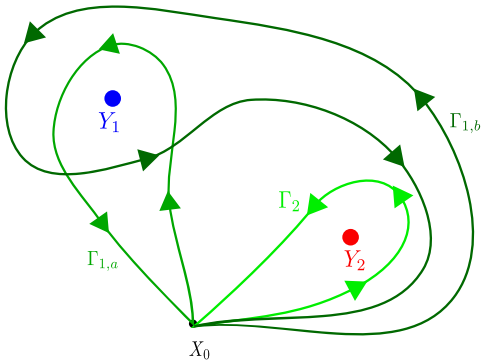

Figure 4.2.: Illustration that shows why the charge is only defined up to conjugacy class. There are two nodes Y_1, Y_2 in different band gaps. We have two different paths with the same base point X_0 going around the blue node Y_1 that assign different charges to it. Adapted from [3].

Assume we have two nodal points Y_1, Y_2 and a fixed base point X_0. We further fix the direction to go around the node as counterclockwise. There are several topologically distinct possibilities to enclose the node Y_1, two of which are shown in Figure 4.2. Either we can take the direct path $\Gamma_{1,a}$ around the node Y_1 or we take the path $\Gamma_{1,b}$ that in addition winds behind the second node Y_2. This second path is homotopic (can be continuously deformed) to the path going around the node Y_2 counterclockwise (path Γ_2), then around Y_1 counterclockwise (path $\Gamma_{1,a}$), and finally around Y_2 clockwise (path Γ_2^{-1}). Using this we find:

$$\Gamma_{1,b} \sim \Gamma_2^{-1} \circ \Gamma_{1,a} \circ \Gamma_2 \tag{4.2.7}$$

where $\circ$ represents the composition of paths that is read from right to left. Ascribing the element $g_i \in \Pi_1(M_N)$ to the path Γ_i we find $g_{1,b} \sim g_2 \cdot g_{1,a} \cdot g_2^{-1}$ which is the definition for elements $g_{1,a}$ and $g_{1,b}$ to be conjugate, i.e. in the same conjugacy class. Therefore, depending on the path we choose around the node, we can get different elements of a conjugacy class describing the node but not elements of other conjugacy classes. This makes the characterization using conjugacy classes unique.

There is a second source of non-uniqueness of the charge arising from the choice of the initial right-handed frame. At the base point of our path, we choose a right handed frame consisting of the eigenstates at this position. However, this choice is not unique as by flipping the orientation of an even number of initial eigenstates, i.e. by a π-rotation around the state not flipping its orientation, we again have a right-handed frame. This ambiguity leads to a conjugation of the quaternion charge assign to the path with an element of the quaternion group. However, again we see that also including this observation we still have a unique characterization using the conjugacy classes.

In the case of Abelian groups, each element has its own conjugacy class. This we see from the fact that for any element g we find that $h \cdot g \cdot h^{-1} = h \cdot h^{-1} \cdot g = g \quad \forall h$ and therefore g is the only element in its conjugacy class. For example, the groups $\mathbb{Z}, \mathbb{Z}_2$ characterizing nodes using the Berry phase or the Chern number are Abelian. This implies that for Abelian groups the characterization with elements is unique and independent of the path.

4.2.3. Correspondence between non-Abelian charge and band nodes

In the previous two sections, we have seen that nodes in models with $N \geq 3$ bands are characterized by the conjugacy classes of the group $\bar{P}_N$. We now have a closer look at this correspondence.

Similar to the edge states in $1D$-models (Chapter 3), a node between two consecutive bands j and $j+1$ corresponds to an elementary π-rotation of the eigenstates $|u^j_{\boldsymbol{k}}\rangle$ and $|u^{j+1}_{\boldsymbol{k}}\rangle$ of the flat band Hamiltonian $\mathcal{H} = \varepsilon = diag(1, \ldots, N)$ along a path $\Gamma \simeq S^1$ around the node. These π-rotations we can relate to elements g_j of the group $\bar{P}_N$ (also called generalized quaternions). The conjugacy class of g_j then represents a node between the bands $(j, j+1)$. With this notation all the conjugacy classes of the group $\bar{P}_N$ are collections of nodes in different band gaps.

The elements $g_j \in \bar{P}_N$ have the following properties which follow from the Clifford-algebra representation of $\overline{P}_N$ [3]:

$$g_j \cdot g_{j+1} = -g_{j+1} \cdot g_j \quad \text{and} \quad g_j^2 = -1 \tag{4.2.8}$$

The first property represents the anticommutation of nodes in neighboring band gaps as well as the commutation of all other pairs of nodes, whereas the second property includes the topological non-triviality of the 2π-rotation. Therefore, we deduce that the exchange of nodes not in neighboring band gaps is trivial but the exchange of nodes in consecutive band gaps is non-trivial. We now check the implications of this non-trivial exchange for the simple case of the quaternion charge.

We now restrict ourselves to Hamiltonians with three bands and the quaternion charge, although we can easily extend these observations to more than three bands. We assign to each conjugacy class a specific type of node and find that the charge $\{\pm\mathrm{k}\}$ corresponds to a node in the lower band gap and $\{\pm\mathrm{i}\}$ to a node in the upper one. Using the rule that $\{\pm\mathrm{i}\} \cdot \{\pm\mathrm{k}\} = \{\mp\mathrm{j}\}$, we find that the charge $\{\pm\mathrm{j}\}$ corresponds to a path that encloses

one node in each band gap. For illustrations, we use the color blue for nodes in the upper band gap ($\{\pm\mathrm{i}\}$) and red for the ones in the lower band gap ($\{\pm\mathrm{k}\}$) [3].

In the previous section, we have seen that the characterization of nodes is only possible up to conjugacy. For nodal lines, we will nevertheless give a meaning to the elements, i.e. the sign of the charge. We relate the sign of the charge to the orientation of the nodal line with respect to a fixed base point using a fixed path.

4.3. Non-Abelian band nodes

We now have a closer look at what the special properties of the non-Abelian charge are. We are in particular interested in the specialties that arise from the non-commutativity. First, we illustrate the properties of the charge explicitly using the case of three bands and the quaternion group. Then, we look at the constraints on nodal line compositions, going into more detail concerning the linking. Finally, we check if an analog of the Nielsen-Ninomiya doubling theorem also holds for this non-Abelian charge.

4.3.1. Braiding of band nodes

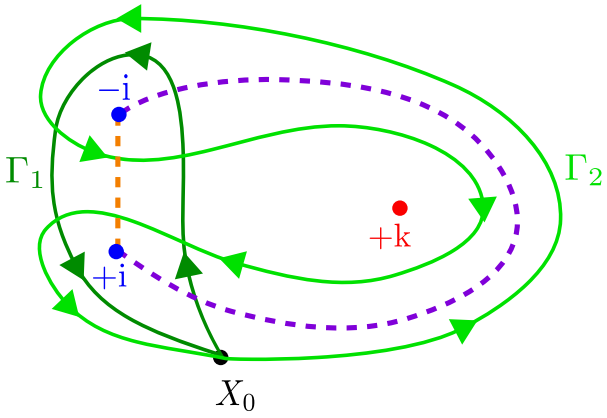

Figure 4.3.: Non-trivial exchange of point nodes in $2D$. We have two nodes created in the same band gap with charges $\pm$i and one node in the other band gap with charge +k (red). Bringing the blue nodes $\pm$i together along the orange path, they can annihilate if, in contrast, they are brought together along the purple line, they cannot annihilate. Adapted from [3].

First, we look at the exchange of nodes which in the non-trivial case is called "braiding". For the sake of simplicity, we start with the case of nodal points in $2D$. Similar to the argumentation why we only use conjugacy classes, we have a base point X_0 and consider different paths (see Figure 4.3). This time we create a pair of nodes inside the path Γ_1 with charges $\pm$i. They need to have opposite charge to be created or annihilated (as $(-\mathrm{i})\cdot\mathrm{i} = 1$ and is therefore trivial). If we now have a node in a different band gap +k

and take a path starting from the base point, which encloses the two nodes ±i by going around node k (path Γ_2), we know from Equation (4.2.7) that the charge of the upper node −i is conjugated as: k(−i)(−k) = i. So the charge of the upper node changes from charge −i to +i. Then the two nodes in the same band gap both have charge +i and they cannot annihilate ((+i) · (+i) = −1). This tells us that it depends on the path we choose to bring the nodes together if they can annihilate or not. Bringing them together in a direct way, they can annihilate, but choosing a path winding behind a different node, they cannot annihilate. This is a first manifestation of the non-Abelian topology.

We can generalize this to nodal lines in $3D$ by interpreting the paths along which we bring the nodal points together as world lines. Considering the time as the third momentum component, we have nodal lines in three dimensions and we deduce, that they change their orientation (sign) if going under a nodal line of different charge.

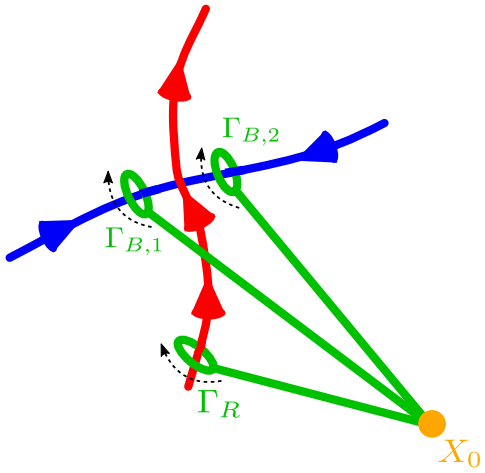

Figure 4.4.: Orientation change of nodal lines using fixed paths. As argued in the text we can fix a path to determine the orientation of the nodal line. This path is shown in green, the black dotted arrow indicated the direction we take around the loop. We see that at the moment the red NL is in front of the blue NL, the orientation changes. The orientations of nodal lines are indicated by red and blue arrows. Adapted from [3].

To understand this in more detail, we consider the situation shown in Figure 4.4. We have a base point (vantage point) X_0 and look at the nodal lines from there. Now, we fix the choice of a path to determine the topological charge of all nodal lines in the same way. First, we go along a straight line to the nodal line, then enclose it with a tight loop and finally come back to the base point following the same straight line. To see what happens to the orientations of the nodal lines we consider a blue NL with charge {±i} going under a red NL with charge {±k}. Then, we choose two paths enclosing the blue nodal line right before and after it goes under the red one. The first called Γ_{B1} and the second Γ_{B2}. In addition, we have a loop Γ_R enclosing the red NL at any point. As

already done twice (compare Eq. 4.2.7), we now know that $\Gamma_{B2} \sim \Gamma_R^{-1} \circ \Gamma_{B1} \circ \Gamma_R$. By choosing the charge of the blue NL on path $\Gamma_{B,1}$ to be +i and the charge of the red NL to be +k, we find the charge of the blue NL on the path $\Gamma_{B,2}$ as $\mathrm{k} \cdot \mathrm{i} \cdot (-\mathrm{k}) = -\mathrm{i}$. So, the blue line changes its orientation. The same argument is valid for a red line moving under a blue line. From this we conclude that whenever a nodal line moves under a nodal line in the other band gap, it changes its orientation.

We can generalize this for the case of more than three bands. Here, we have to distinguish nodes in consecutive band gaps from nodes in further distant band gaps. Nodes that are not in neighboring band gaps have commuting topological charges, and will therefore keep the orientation when moving under each other. For nodes in neighboring band gaps, the charges anticommute, and we have the same situation as for the two gaps in a three band model. So, the orientation of a nodal line in a band gap changes whenever it goes under a nodal line of a neighboring band gap.

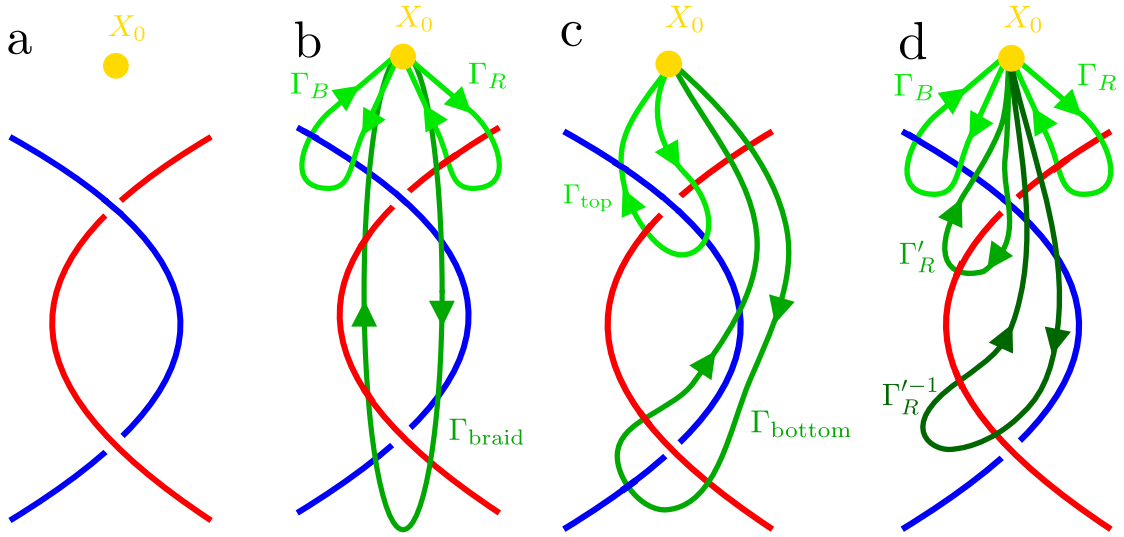

Figure 4.5.: Reciprocal braiding of band nodes: Panel (a) shows the braiding of two nodes. (b) shows the path enclosing the braid starting from the base point X_0 and the two paths enclosing the blue and red nodal line separately. In (c) the path enclosing the braiding is split into one enclosing the upper crossing point and one the lower one. Panel (d) includes paths only enclosing one of the two nodal lines needed to express the path around the braid. Adapted from [3].

Having seen these orientation changes, we now consider the braiding of nodal lines a bit closer as we will encounter it again in the model presented in Section 5.1. By braiding we mean that two nodal lines (or world lines of nodal points, see Ref. [29]) move twice across each other, so that each of them goes under the other once. So, we start for example with charges i (blue) on the left and k (red) on the right, then first move the red under the blue to the left and thereby change its orientation to −k and then move the blue under the red changing its orientation to −i. Finally, we end up

with both nodes at the same position as in the beginning but with opposite charges (Figure 4.5a). Now we show that this braiding is non trivial and we cannot undo it by moving the two nodal lines across each other, while letting the ends fixed. This relates to the non-triviality of the 2π rotation and we could already expect the braiding to have a non-Abelian charge of -1. We now show this in a more specific way.

To obtain the charge of the braid, we enclose the two crossings of blue and red nodal lines by a loop Γ_{braid} starting and ending at the base point X_0 (illustration in Figure 4.5b-d). We now want to express this loop using a homotopic loop that is a combination of the trivial loops Γ_R and Γ_B going around the red and blue nodes, respectively. Therefore, we first divide it into two loops one going around the top and one around the bottom crossing: $\Gamma_{\text{braid}} \sim \Gamma_{\text{top}} \circ \Gamma_{\text{bottom}}$. If at the top the red line goes under the blue line the loop Γ_{top} is homotopic to going first around the blue and then around the red, i.e. $\Gamma_{\text{top}} \sim \Gamma_R \circ \Gamma_B$.

To get the loop around the crossing at the bottom with the red line above the blue, we introduce a loop going around the red line after the top crossing: $\Gamma'_R \sim \Gamma_B^{-1} \circ \Gamma_R \circ \Gamma_B$. Considering that the loop changes direction at the flection point of the nodal line we find that: $\Gamma_{\text{bottom}} \sim \Gamma_b^{-1} \circ \Gamma_R'^{-1}$. Therefore, we express the whole loop as:

$$\Gamma_{\text{braid}} = \Gamma_{\text{top}} \circ \Gamma_{\text{bottom}} = \Gamma_R \circ \Gamma_B \circ \Gamma_B^{-1} \circ \Gamma_R'^{-1} = \Gamma_R \circ \Gamma_B^{-1} \circ \Gamma_R^{-1} \circ \Gamma_B \tag{4.3.1}$$

Assigning the orientation of nodal lines such that a loop Γ_B corresponds to the charge $+\mathrm{i}$, we find for the charge of the braid:

$$n_{\text{braid}} = \mathrm{i} \cdot (-\mathrm{k}) \cdot (-\mathrm{i}) \cdot \mathrm{k} = \mathrm{j}^2 = -1 \tag{4.3.2}$$

So this braiding has a non-trivial topological charge.

4.3.2. Constraints on nodal line compositions

We have some further implications from the non-commutativity of the charge, namely there are some constraints on how nodal lines can be organized together in momentum space. For simplicity we again consider only three bands, before generalizing to more bands. We find three constraints on compositions of nodal lines.

i) Nodal lines with different color (charge) cannot cross. This means, we cannot undo a linking of two different nodal lines.

ii) A nodal ring of one color can only enclose an even number of nodal lines of the other color.

iii) The meaning of $\mathrm{i}^4 = 1$ is really that four nodal lines with same charge and orientation can annihilate.

For the second property, we consider a simple illustration of linked nodal lines and look at their orientations (Figure 4.6). If we have a blue NL ring in the upper band gap

and want to link it with only one red nodal line, there is an ambiguity in the definition of the orientation of the NL ring. Linking it, instead, with two red nodal lines we are able to uniquely determine the orientation.

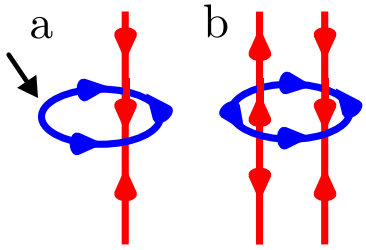

Figure 4.6.: Linking possibilities of nodal lines. Panel (a) shows the situation where the blue nodal line encloses only one red nodal line. The black arrow indicates where a problem with the orientations occurs as the orientation would have to change without passing below a red nodal line. In (b) the possible linking with two nodal lines of the other color is shown.

This directly implies the first property. Figure 4.7 shows the situation before and after moving two NL rings of different color across each other. Yet we have just seen that the second of these situations is not possible which implies that we cannot move different kinds of nodal lines across each other by a continuous deformation of the Hamiltonian.

An illustration on how to annihilate four nodal lines of same charge and orientation can be found in the Supplementary of [3] (Figure S14).

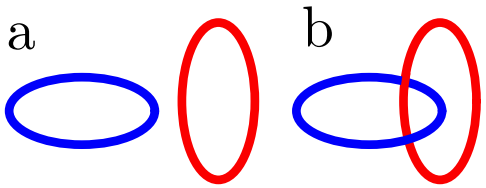

Figure 4.7.: Allowed and forbidden nodal line compositions. Panel (a) shows the allowed composition of two nodal rings. Whereas in (b) we have a problem concerning the orientation of both nodal rings. This pair of illustrations implies that red and blue nodal lines cannot pass through one another.

We now generalize these constraints to more than three bands in the same way as we did it in the last section. Considering that nodal lines in non-neighboring band gaps have commuting charges, we do not have any constraints on them. They can clearly cross each other and enclose an arbitrary number of nodal lines that do not occur in neighboring band gaps. Interesting is only the case of nodal lines in neighboring band gaps as their charges anticommute. They have the same constraints as we just saw for the three band models and the quaternion charge. Clearly, the last property, that four nodal lines with the same charge and orientation can annihilate, holds in any band gap independent of the number of bands.

4.3.3. Linking of nodal lines

In the following chapters, we consider models with linked vs. unlinked nodal lines. Therefore, we want to argue why this linking is interesting in topological materials.

Up to now we have considered the topological characterization of nodal lines using the first homotopy (or fundamental) group. This we have done by enclosing the nodal lines with a closed loop isomorphic to the circle S^1. In $3D$ we can also enclose a ring-shaped nodal line with the sphere S^2 and then characterize the topology of the nodal lines by the second homotopy group of the parameter space $\Pi_2(M)$[2] [24].

Studying the linking of nodal lines, we restrict ourselves to ring-shaped nodal lines, so-called NL rings. If we enclose such a ring with a sphere S^2, we can assign to it an element of the second homotopy group $\Pi_2(M)$. As we are mainly interested in the characterization of nodes in the band gap between the conduction and the valence band, we concentrate on the characterization of Hamiltonians with n occupied and l unoccupied bands, described in Equation (4.2.1). In this case, we have the parameter space given as the real Grassmanian $M_{(n,l)} = O(n+l)/O(n) \times O(n)$. The first homotopy group of this space describes the Berry phase which in the case of $n + l \geq 3$ is quantized to 0 or π, whereas the second homotopy group characterizes the monopole charge. This monopole charge is of interest, as it can be related to higher-order topology [30]. We do not go into more detail on the higher-order topology here but we briefly elaborate on the relation between the monopole charge and the linking number of a NL ring [23].

We can define two linking numbers that describe the linking of a NL ring with nodal lines in neighboring band gaps. By the subscript ± 1, we denote either the band gap above or below the one hosting the NL ring. The value of $w^a_{\pm 1}$ is ± 1 for nodal lines linked with the ring, $+1$ for the orientation away from the ring and -1 if orientated towards the ring. Using this we can define the following quantities [23]:

$$\eta_\pm = \sum_a w^a_{\pm 1} \in \mathbb{Z} \tag{4.3.3}$$

that counts the number of sources and sinks, respectively and

$$\nu_\pm = \frac{1}{2}(\eta_+ \pm \eta_-) \in \mathbb{Z} \tag{4.3.4}$$

So, the number η_+ (η_-) represents the linking with nodal lines in the band gap above (below) the band gap of the NL ring and $\nu_\pm$ is simply a linear combination of them.

For a three band model, we only have two band gaps and there is only one linking number with the neighboring band gap. From the properties of the non-Abelian charge, it is clear that the linking number has to be a multiple of 2, i.e. $\eta = 2n$ with $n \in \mathbb{Z}$, called the Euler class. So the linking number corresponds to elements of the group $2\mathbb{Z}$.

In the case of a four-band model, we find an integer linking number to the nodal lines in the band gap above as well as below with the constraint that the sum of them has to be even ($\eta_- + \eta_+ =$ even), due to the constraint (ii) on nodal line compositions. Thus $\nu_\pm$ define a $\mathbb{Z} + \mathbb{Z}$ topological invariant, corresponding to two Euler numbers.

[2]For the definition of the second homotopy group consider the Appendix A.2.

If we consider many band models with more than six bands, using the non-Abelian charge, it is possible to show that the linking number in that case has the group structure of $\mathbb{Z}_2$. This is done, based on the fact that in many band models, it is possible to trivialize the linking with an even number of nodal lines. The exact prove of this procedure and the linking numbers of all other possible combinations of occupied and unoccupied bands are shown in Ref. [23].

For any number of bands the linking numbers exhibit the same group structure as the monopole charge. So, we can interpret the monopole charge as an information on the linking [23].

A similar result was found by Ref. [31]. They proved the equivalence of the linking number and the monopole charge using the second Stiefel-Whitney class.

We have now seen, why the linking of nodal lines is interesting for topological materials and that it can be related to the monopole charge of nodal lines. This relation can be shown quite easily by using the properties of the non-Abelian charge [23]. As a last step concerning the non-Abelian charge we want to check if the well known doubling theorem (first published by Nielsen and Ninomiya [28] in the context of Weyl fermions and neutrino physics) can be generalized for the non-Abelian charge.

4.3.4. Violation of the doubling theorem

In this section, we show that the Nielsen Ninomiya doubling theorem does not hold for the non-Abelian charge, by which we mean it is possible to produce band nodes with a total non-trivial charge. We do this in analogy to the formulation using Dirac strings[3] done in Ref. [32].

The fermion doubling theorem, in general, states that topological point nodes in the bulk of a lattice Hamiltonian can only occur in pairs such that the total charge of all band nodes vanishes. Examples for the doubling theorem are Dirac points in graphene or Weyl points in $3D$ Weyl semimetals. In other words, we can say that if a Weyl point has a winding number $+1$, there must exist a second one with winding number -1, so the sum over all winding numbers in the BZ has to be zero [33].

A counter example to this was found by Ref. [32]. Using Dirac strings, the work shows that it is possible to have a total winding number of ± 2 in systems with nonzero Euler class when starting with two nodes having winding number $+1$ and -1.

We now want to check the doubling theorem for the non-Abelian charge. The question is if we can show that the product of all nodal points in $2D$ or cross-sections of nodal lines in $3D$ inside the BZ is trivial (equal 1). Using the same arguments as Ref. [32], we see that we could also end up with total non-Abelian charge of -1. To see this, we consider point nodes in $2D$ with Dirac strings. In our context a Dirac string is a tool to implement the non-commutativity of the charges, i.e. if a blue node passes the Dirac string of a red node it reverses its charge and vice versa.

[3] In general Dirac strings are used to include discontinuities in the gauge of a system.

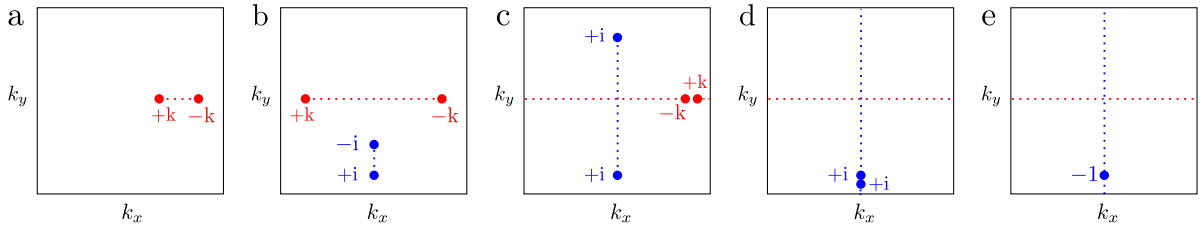

Figure 4.8.: Violation of the doubling theorem for the non-Abelian charge. In panel (a) two red nodal points are created. One of them (b) is moved to the right and two blue nodal points are created. In (c) one of these blue nodes is moved across the BZ and changes its sign when crossing the Dirac string of the red nodes. Panel (d) and (e) show that the red nodes are annihilated but the blue ones leave behind a non-Abelian charge of -1. Adapted from [32], Figure 6.

At time zero, two nodal points with charges $\pm$k in the lower band gap (red) are created. This is possible as the total quaternion charge is $\mathrm{k} \cdot (-\mathrm{k}) = 1$ and therefore the system is in a trivial state. One of them is moved across the BZ and then they are pairwise annihilated leaving behind a Dirac string across the BZ. Now, we create two nodal points in the other band gap $\pm$i (blue). Again, we move one of them (charge $-$i) across the BZ but the moment it crosses the Dirac string of the red nodal line it changes its sign to $+$i. If we now bring them together by crossing the BZ boundary, they cannot annihilate anymore because $(+\mathrm{i}) \cdot (+\mathrm{i}) = -1$ and we end up with a non-trivial total charge (compare Figure 4.8). Hence, we prove that the doubling theorem does not hold for the non-Abelian charge and we can actually have a non-trivial total charge of all nodal points inside the BZ. This can also be extended to $3D$ by looking at different two-dimensional cross-sections through the three-dimensional BZ.

4.4. Open questions and goals

At the end of this quite theoretical first part, we state the goals, we address ourselves to in the numerical analysis of different models describing topological $\mathcal{PT}$-symmetric semimetals. In the following chapters, we will focus on three open problems:

- Better understanding of the correspondence between the edge/surface states of topological materials and the quaternion charge.
- Possibility to differentiate linked and unlinked nodal lines by looking at the surface spectrum.
- Better understanding of the topological phase with non-Abelian charge -1. From the numerical results on the one-dimensional models (Chapter 3, we have the following conjecture: In the topological phase with non-Abelian charge -1 there is always an edge state crossing the middle band from one band gap to the other.

5. Models

For the numerical analysis of the surface states and the bulk-boundary correspondence between the surface states and the non-Abelian topological charge, we use different models. First, one two-dimensional model with point nodes including a tuning parameter (time) that allows us to interpret the point nodes as world lines. Second, we constructed two three-dimensional models in one case with linked and in the other with unlinked nodal-line rings. The diagonal surface BZ projection of these two models looks very similar.

In this chapter, we introduce these three models and show their nodal-line structures. Furthermore, we calculate the quaternion charge of these models along paths through the BZ to arrive at a topological phase diagram consisting of areas with different non-Abelian topological invariants. For all models the lattice parameter a is set to unity.

5.1. 2D braiding model

First, we introduce a two dimensional model with point nodes (Weyl points) that perform a braiding when considering their motion with a tuning parameter t. This model was proposed by Ref. [29]. Then, we have a closer look at this braiding of the nodal points during the evolution along t. Finally, we look at the model from the point of view of the quaternion charge and calculate its value for all threads projecting onto points in the surface BZ[1].

5.1.1. Model in reciprocal and real space

Ref. [29] presents a model with three orbitals per site, an on-site potential on the first orbital and an on-site hopping between the other two orbitals. Furthermore, next nearest hopping between different orbitals is included, resulting in the following Hamiltonian matrix[2]:

$$\mathcal{H}_{2D}(\boldsymbol{k},t) = \begin{pmatrix} f(t) & g(\boldsymbol{k}) & g^*(\boldsymbol{k}) \\ g^*(\boldsymbol{k}) & 0 & h(\boldsymbol{k},t) \\ g(\boldsymbol{k}) & h^*(\boldsymbol{k},t) & 0 \end{pmatrix} \tag{5.1.1}$$

for $\boldsymbol{k}$ inside the BZ $[-\pi,\pi]^2$ and the tuning parameter $t \in [-10,10]$. The on site potential $f(t)$ for the first orbital and the couplings $g(\boldsymbol{k})$ (between the first and the second or third

[1]The surface BZ is the projection of the bulk BZ along some axis, therefore for a BZ of dimension N, it has dimension $(N-1)$. For the construction of the surface BZ see Figure 6.3.

[2]The model is taken from an earlier version of the paper: arXiv version 3, Jan 15 2020 [34].

orbitals) and $h(\boldsymbol{k}, t)$ (between the second and third orbitals) are defined as follows:

$$f(t) = F_{[8,-]}(t) \qquad g(\boldsymbol{k}) = -\mathrm{i} \cdot \left(e^{-\mathrm{i}k_x} - e^{-\mathrm{i}k_y}\right) \tag{5.1.2}$$

$$h(\boldsymbol{k}, t) = h_0(t) + h_1(t) \cdot \left(e^{\mathrm{i}k_x} + e^{\mathrm{i}k_y}\right) \tag{5.1.3}$$

$$\text{with} \qquad h_0(t) = F_{[2,-]}(t) \text{ and } h_1(t) = (10 - F_{[8,+]}(t)) \tag{5.1.4}$$

$$\text{where} \quad F_{[\nu,\pm]}(t) = \frac{1}{2}(|t+\nu| \pm |t-\nu|) \tag{5.1.5}$$

The function $F_{[\nu,\pm]}(t)$ is piecewise linear and has kinks at positions $t = \pm\nu$. This implies that also the functions $f(t), h_0(t)$ and $h_1(t)$ are piecewise linear, compare Figure 5.1.

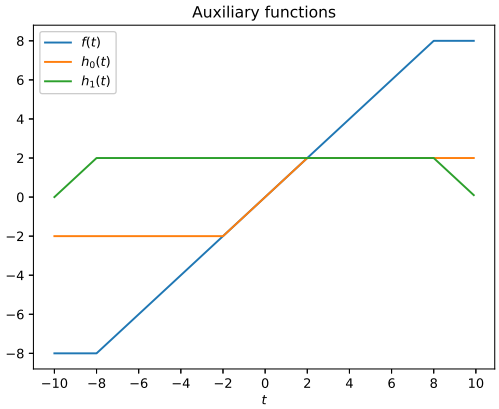

Figure 5.1.: Auxiliary functions used in the definition of the Hamiltonian. The functions $f(t)$ and $h_0(t)$ are point reflected at zero. Therefore, we have no on site hopping for the case $t = 0$. In contrast, the function $h_1(t)$ is mirror reflected w.r.t. the y-axis and non-zero for $t = 0$.

To get a better understanding of this Hamiltonian, we first have a look at the energy spectrum with periodic boundary conditions in both directions x and y. Figure 5.2 shows the energy surfaces for the values $t = -2, 0, 4$. For all values of t the nodal points lie on the diagonals of the BZ. This is why we will be mainly interested in the diagonal projections of this Hamiltonian.

Before going into more detail concerning the behavior of the nodal points in this model, we want to transform it into real space. For the Hamiltonian defined in Eq. (5.1.1) it is possible to directly read out the hopping amplitudes for the tight-binding model. We label the orbitals as A,B and C (from top to bottom in the matrix) and find the real space hopping parameter shown in Figure 5.3. Using these parameters we are able to set up the finite real space model with different types of edges (Section 6.1).

a

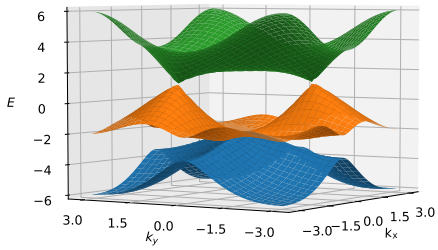

b

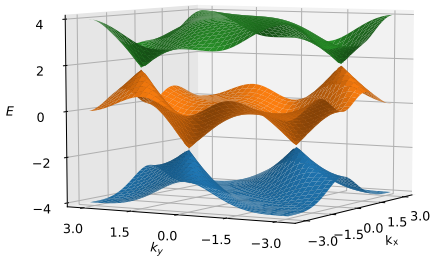

c

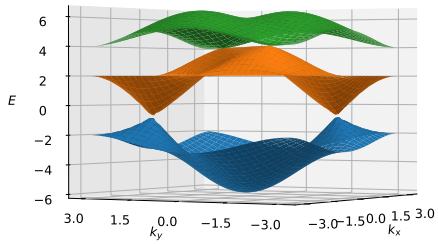

Figure 5.2.: 2D model: Spectrum of the Hamiltonian for values $t = -2, 0, 4$. Panel (a) shows the two-dimensional spectrum of $\mathcal{H}_{2D}$ for $t = -2$. We clearly see two nodal points along one of the diagonals in the upper band gap, as well as a band touching in the middle of the BZ for the lower band gap. Panel (b) shows the spectrum for $t = 0$. Here, we observe two nodal points in the upper and two of them in the lower band gap. All four nodal points lie on the same diagonal of the BZ. Panel (c) shows the situation for $t = 4$. We again observe four nodal points two of them in the upper band gap on one diagonal and the other two in the lower band gap on the other diagonal.

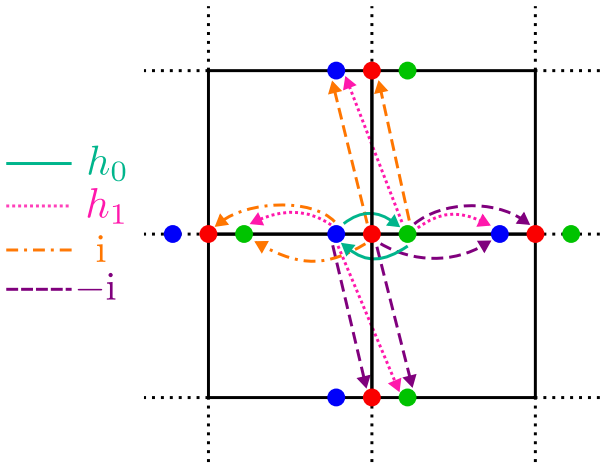

Figure 5.3.: Hopping amplitudes in real space for the two-dimensional braiding model. The red dots represent orbital A, the green ones orbital B and the blue ones orbital C. The hopping probability from the unit cell in the center are represented by the arrows with different colors.

5.1.2. Braiding of the point nodes

We now have a further look at the evolution of the nodal points as a function of t. The parameter t can be interpreted either as the time or as a third momentum component. The later assumption allows us to interpret the trajectories of the nodal points as nodal lines in a 3D model.

Looking at the spectrum for three values of t, we already realized that the nodes lie on the BZ diagonals. This is also true for all other values of t.

From the previous chapters on the non-Abelian charge, we know that the presence of a node in the neighboring band gap can influence the node in the considered band gap. For example, we have seen in Figure 4.3 that in the presence of a node in the neighboring band gap, it depends on the path we choose to bring two nodes together if they can annihilate. This property is also manifested by the Hamiltonian $\mathcal{H}_{2D}$.

We follow the evolution of the nodal points by looking at the spectrum of the Hamiltonian along the two diagonals (11) and $(1\bar{1})$ of the BZ. As in Section 4.3, we denote by $\{\pm\mathrm{k}\}$ the nodes in the lower band gap with color red and by $\{\pm\mathrm{i}\}$ the nodes in the upper band gap having color blue.

For $t = -9$, there appears a pair of nodes in the upper band gap at Γ and move outwards along the diagonal $(1\bar{1})$. Later, for $t = -6$ a second pair of nodes appears but this time in the lower band gap and at M moving towards the center Γ along the diagonal (11). At $t = -2$ these two nodes in the lower band gap meet at Γ and start moving outwards along the other diagonal $(1\bar{1})$. Therefore, as observed in the two-dimensional spectrum for $t = 0$ (Figure 5.2) all the nodal points lie on the same diagonal $(1\bar{1})$. For $t = 2$ the nodes in the upper band gap meet in M (at the boundary of the BZ) and start moving towards Γ along the diagonal (11). Finally, for $t = 6$, the nodes in the upper band annihilate at Γ and for $t = 9$ the other two nodes in the lower band gap annihilate

in M. This process is shown in Figure 5.4

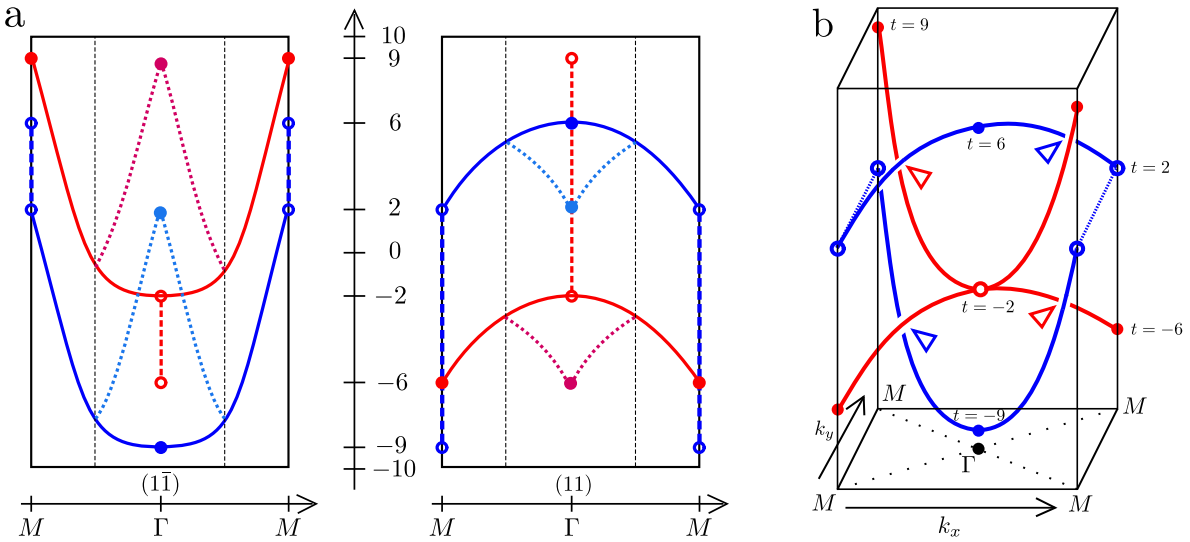

Figure 5.4.: Braiding of the point nodes along the tuning parameter t. For simplicity the figures only show the schematics and not the actual trajectories of the nodal points. These are slightly different and shown in Figure 5.7. Panel (a) shows the two diagonal cuts through the BZ. The red circle indicates the position where the red nodal points change the direction and the blue circles show the direction change of the blue nodal points. By the periodicity all four blue circles indicate the same position in reciprocal space. The dotted lines indicate nodal points moving along the projected direction. In addition the folding into the surface BZ is shown (explained in Figure 5.6). The black dotted lines show the boundaries of the surface BZ and the lighter blue and red doted lines indicate the folded nodal lines. In panel (b) the same is shown in a $3D$ picture where we see the world lines of the nodal points in the two-dimensional BZ. The red and blue triangle show the sign changes of the charges.

In this process the blue nodes as well as the red nodes meet one time but fail to annihilate. This is a manifestation of the non-Abelian braiding. Even tough the blue as well as the red nodes were created as a node-antinode pair, they fail to annihilate at $t = -2$ and $t = 2$ for the blue and the red nodes, respectively. We can see this from the fact that a nodal line changes its orientation when moving under a nodal line of different charge. This is also true for nodal points, i.e. a nodal point changes its sign if its world line moves under the world line of a nodal point with different charge. These sign changes are indicated in Figure 5.4 as triangles. Considering these sign changes, we observe that at the red circle where the two red nodes meet the first time, one of them changed its sign and they will have the same charge which leads to a total charge of -1, so they cannot annihilate. In contrast, until they meet a second time at the boundary of the BZ for $t = 9$, again one of them has changed its sign which then leads to a total charge of $+1$ and they are able to annihilate. The same is true for the blue nodal points. They have a non-trivial total charge of -1 at the blue circles.

5.1.3. Quaternion charge

We now studied the quaternion charge for single nodes and how they change because of the braiding. Another possibility to look at the quaternion charge for a two dimensional model, is to define one-dimensional closed paths through the BZ and define the quaternion charge of this threads. We then end up with regions of different quaternion charge inside the surface BZ projection that are bounded by nodal lines. We now want to determine these regions for different projections. The projections are done along the k_x-axis (the projection along k_y looks exactly the same) as well as along the two diagonals. Figure 5.5 defines the corresponding threads.

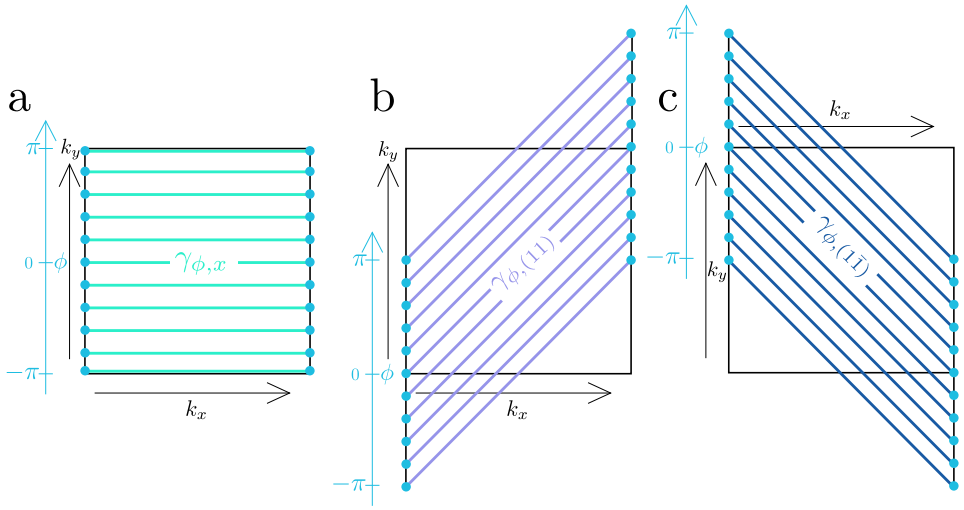

Figure 5.5.: One-dimensional threads through the two dimensional BZ to define the quaternion charge of the $2D$-model. The blue dots indicate the same points just in a different copy of the BZ such that all paths γ_ϕ are closed.

When calculating the quaternion charge along these threads in Figure 5.5b and c, we observe a folding of the BZ. This is also observed by the surface BZ projection along the diagonals. We only take threads through the middle of the BZ and miss some part at two corners. These parts then appear along other threads through the BZ, what we call the folding of the BZ. The procedure of this folding is shown in Figure 5.6.

In Section 3.2.3, we discuss how to calculate the quaternion charge numerically for real one-dimensional systems. The Hamiltonian $\mathcal{H}_{2D}$ (Eq. 5.1.1) is complex. To be able to apply the same technique, we need to make this Hamiltonian real-symmetric[3]. For a $\mathcal{PT}$-symmetric Hamiltonian, this can be done by a constant (k-independent) unitary transformation. Such a constant transformation cannot change the topological invariant of the Hamiltonian up to a group automorphism of the quaternion group, i.e. it is unique for charges $+1$ and -1 but could interchange the charges i,j and k [3]. In our case Ref. [29]

[3]The Hamiltonian has to be symmetric as we still require the Hermicity $\mathcal{H}^\dagger = \mathcal{H}$.

suggests the following transformation:

$$\mathcal{H}_{2D,\text{real}}(\boldsymbol{k},t) = V\mathcal{H}_{2D}(\boldsymbol{k},t)V^\dagger \quad \text{with} \quad V = \sqrt{1\oplus\sigma_x} = \begin{pmatrix} \mathrm{i} & 0 & 0 \\ 0 & \frac{-1+\mathrm{i}}{2} & \frac{1+\mathrm{i}}{2} \\ 0 & \frac{1+\mathrm{i}}{2} & \frac{-1+\mathrm{i}}{2} \end{pmatrix} \tag{5.1.6}$$

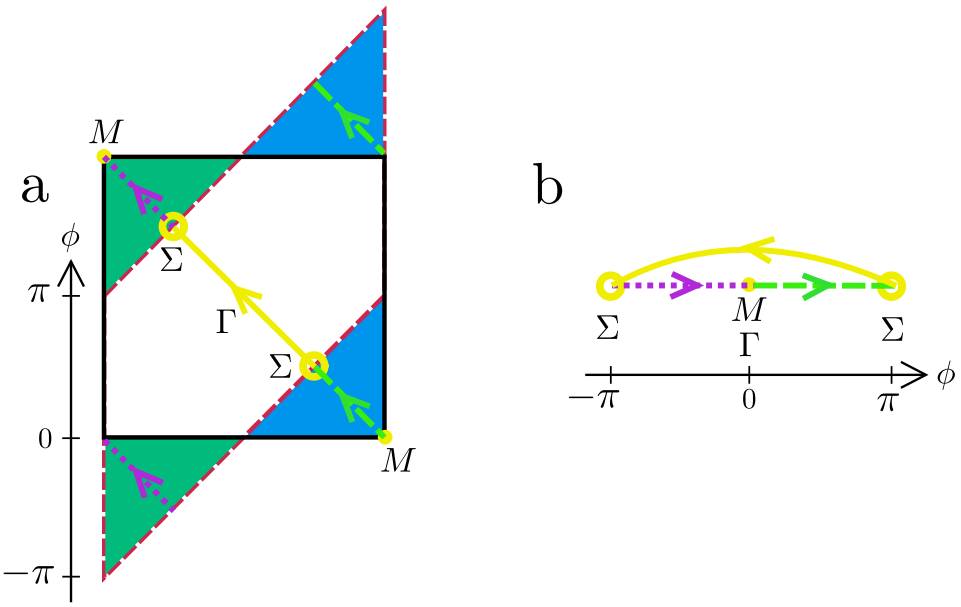

Figure 5.6.: Folding of the BZ along the diagonal projection onto the surface BZ. The black square in panel (a) is the actual BZ. The dotted dark red rhomboid indicates the area, we cover with the threads in Figure 5.5b. By periodicity the two green (blue) triangles represent the same part of the system. The line between the two corners represents a nodal line through the BZ. Panel (b) shows how this nodal line is represented in the folded BZ. The parts of the line with the same color (shape) represent the same in panels (a) and (b).

We are now able to calculate the quaternion charge of the real Hamiltonian (Eq. 5.1.6) along the one-dimensional threads in Figure 5.5. This is done by defining a $1D$ version of the Hamiltonian for a parameter ϕ and a family of closed paths γ_ϕ (threads) through the BZ. The $1D$ Hamiltonian looks as follows:

$$\mathcal{H}_{1D,\phi}(k,t) = \mathcal{H}_{2D,\text{real}}(\gamma_\phi(k),t) \tag{5.1.7}$$

where $k \in [-\pi,\pi]$ is the one-dimensional momentum along which we determine the quaternion charge, and $\phi \in [-\pi,\pi]$ indicates the position of the thread in the BZ.

We take three different families of the paths γ_ϕ along the k_x-axis and the two diagonal axes:

$$\gamma_{\phi,x}(k) = \begin{pmatrix} k \\ \phi \end{pmatrix} \qquad \gamma_{\phi,(11)}(k) = \begin{pmatrix} k \\ \phi + k \end{pmatrix} \qquad \gamma_{\phi,(1\bar{1})}(k) = \begin{pmatrix} k \\ \phi - k \end{pmatrix} \tag{5.1.8}$$

Using these paths, we find the topological phase diagrams in Figure 5.7. Between two regions of different color in these diagrams, there must occur a node. So, we can recognize the evolution of the nodal points along t from Figure 5.4 in the phase diagrams.

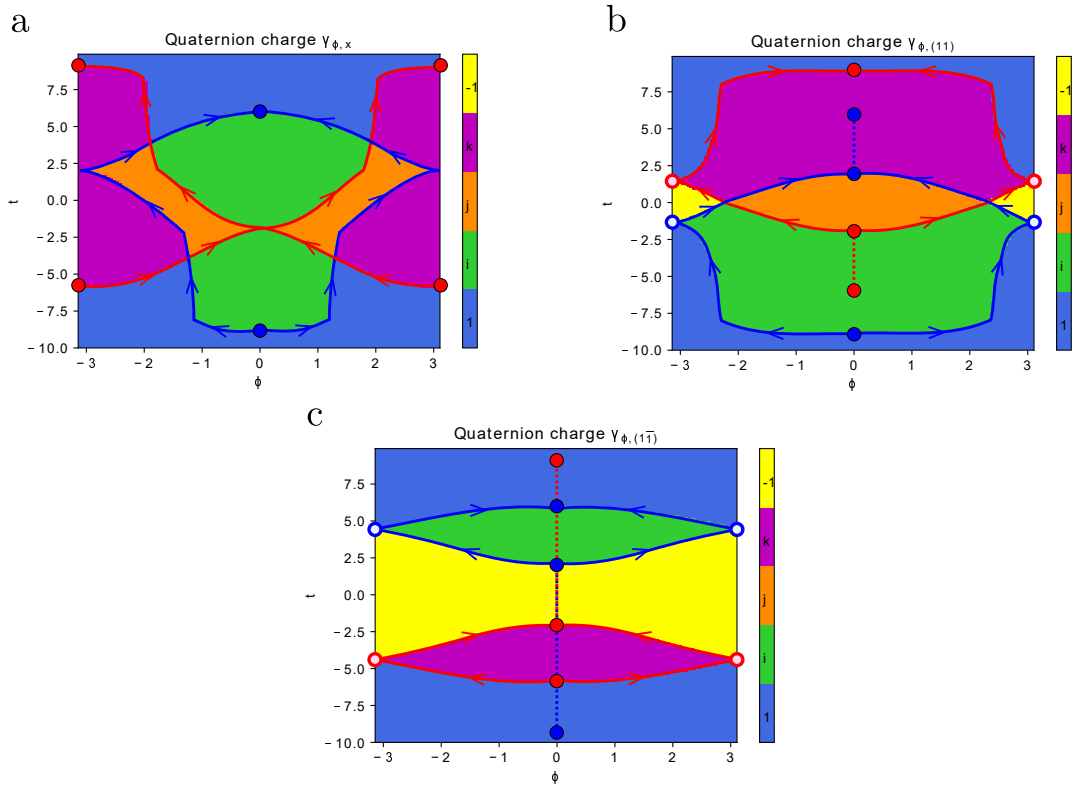

Figure 5.7.: Quaternion charge phase diagram for the $2D$-models for different projections of the BZ. Panel (a) shows the phase diagram for threads along the x-axis, panel (b) along the diagonal (11) and (c) along $(1\bar{1})$. The different colors indicate the phases of different topological charge and the red and blue lines show the trajectories of the nodal points in the lower and upper band gap, respectively.

For the projection along the k_x-axis (Figure 5.7a), we clearly recognize the nodal structure of the model. The green phase starting at $\phi = 0$ for $t = -9$ indicates the node in the upper band gap and the violet region starting at the boundary for $t = -6$ represents the occurrence of the red node in the lower band gap. The orange region with charge j is enclosed by the two nodes and appears/disappears at the braiding points where the trajectories of one nodes goes under the trajectory of the other node.

Panel (b) in Figure 5.7 shows the projection along the (11) diagonal. This can be compared to the cut along the $(1\bar{1})$ diagonal in Figure 5.4a. We again see the pair of blue nodes created at $t = -9$. The red pair created at $t = -6$ cannot be seen as they move along the projected diagonal (indicated by the red dotted line in the figure). At $t = -2$ the blue nodes are at the boundaries of the projected BZ (indicated by blue circles) but by looking at the BZ folding, they appear in a different copy of the BZ and

move towards the center along the orange-violet boundary. For $t = 2$ they disappear as they start moving along the projected diagonal (blue dotted line). The red nodes appear at $t = -2$ in the center as then they move along the diagonal $(1\bar{1})$ which is visible in this projection. They reach the boundary of the projected BZ (red circles) for $t = 2$ and start moving towards the center in a different copy of the BZ enclosing the violet region until they annihilate at $t = 9$. As for the k_x-projection, we find an orange region between the crossing points of the world lines. But in addition, we find the yellow region with charge -1 which we are mainly interested in.

With the same folding of the actual BZ into the surface BZ projection, we look at the last phase diagram (Figure 5.7c). Here, the projection along the $(1\bar{1})$ diagonal is shown and we observe the right panel in 5.4a. We cannot see the blue nodes created at $t = -9$ (blue dotted line) but we see the red ones appearing in the center at $t = -6$. They move towards the boundary (red circles) and back to the center until at $t = -2$ they start moving along the projected diagonal and therefore are not visible anymore (red dotted line). The blue nodes appear at $t = 2$ where they start moving along the diagonal (11). They move to the boundary of the projection (blue circles) and then back to the center enclosing the green region. In this projection, we only find the yellow region -1 but no orange region.

We find the phase with non-Abelian charge -1, in which we are mainly interested, for both diagonal projection. Therefore, we can test our conjecture that in the phase -1 there is a surface state crossing the middle band on this model. This we do in Section 7.3.

5.2. 3D models

After this two-dimensional model with point nodes interpreted as world lines, we now have a look at truly three-dimensional models with nodal lines that are periodic in the third momentum component k_z. We construct two models that look very similar in the diagonal surface BZ projection but in one case the nodal lines in the bulk are linked and in the other case they are unlinked.

5.2.1. Construction

Again, we want to have a three-band model to be able to use the quaternion charge for the description. Therefore, the model has three orbitals A,B,C represented in the Hamiltonian matrix from top to bottom. We choose A to be a p_y-orbital, B a p_x-orbital and C an s-orbital.

With these orbitals, we set up the Hamiltonian as a tight binding model. From the symmetries of the orbitals there are already some restrictions on the hopping amplitudes [35]. For example it is not possible to have a nearest neighbor hopping between the p_x and the p_y orbitals as there is no overlap. Furthermore, due to the symmetry of the

orbitals, the nodal lines are pinned to the high symmetry planes $k_x, k_y = 0, \pm\pi$ in the BZ.

During the process of the construction, we included hoppings by up to four primitive lattice vectors but in the end, we only needed hoppings by three primitive lattice vectors for the linked model and by two for the unlinked one. To find the models, we set up a Hamiltonian with all symmetry-compatible hopping amplitudes as parameters in Python and Mathematica. By checking the Hermicity and the behavior under mirror reflection, i.e.

$$\mathcal{H} = \mathcal{H}^\dagger \quad \text{and} \tag{5.2.1}$$

$$\mathcal{H}(m\boldsymbol{k}) = \hat{m}\mathcal{H}\hat{m}^{-1} \text{ for: } \hat{m} = \hat{m}_x, \hat{m}_y \tag{5.2.2}$$

where $m\boldsymbol{k}$ is the mirror-reflected momentum, and $\hat{m}$ is the mirror operator in the Hilbert space spanned by the (p_y, p_x, s) basis, we ensure that the Hamiltonian has the right properties. We now look at the band structure for different projections of the BZ or cuts through the BZ to find and adjust band nodes. Using Mathematica, we added sliders for the hopping amplitudes to directly adjust the hopping parameters.

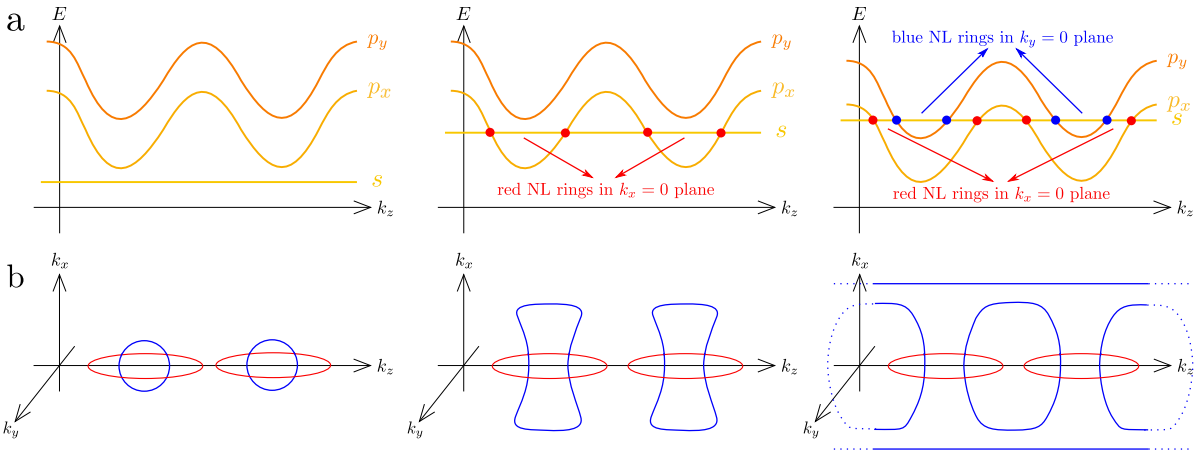

Figure 5.8.: Construction of the linked Hamiltonian. The upper panel shows the band inversion to construct the nodal lines in the $k_x = 0$ and $k_y = 0$ planes. In the lower panel, we show how the deformation is done to arrive at the linking. The dotted line show the continuation in the neighboring BZ.

The construction of the linked model follows the idea of Ref. [31] that uses a double band inversion in a four-band model to produce linked nodal rings with a monopole charge. Here, we want to use only three bands to arrive at linked nodal lines. Our idea is to start from three flat bands and then, add some $-\cos(2k_z)$ shape to the upper two bands coming from orbitals p_y, p_x. Afterwards, we increase the energy of the s-orbital band to first cross the band from orbital p_x, thereby creating a red (lower band gap) NL ring in the $k_x = 0$ plane. Further increasing the energy, it also crosses the p_y-band creating a blue NL ring in the $k_y = 0$ plane. The last and most difficult step is to now

adjust the hopping parameters such that the blue nodal lines are enlarged and then reconnect at $k_z = 0$ and $k_z = \pm\pi$ inside the BZ to end up with linked nodal lines (compare Figure 5.8). We achieve this by including electron hoppings by up to two primitive lattice vectors, e.g. terms of the form $\cos(2k)$.

In addition to this linking of the nodal lines lying in the $k_x = 0$ and $k_y = 0$ planes, respectively, we require that there are no additional nodal lines in the $k_x, k_y = \pm\pi$-planes. To do so, we simply add some additional hopping parameters to suppress the nodal lines occurring in these planes. Including these hopping parameters, we end up with the following Hamiltonian consisting of hoppings by up to three primitive lattice vectors.

$$\mathcal{H}_{\text{linked}} = \begin{pmatrix} \phi_A & t_{AB}^* & t_{AC}^* \\ t_{AB} & \phi_B & t_{BC}^* \\ t_{AC} & t_{BC} & \phi_C \end{pmatrix} \tag{5.2.3}$$

with the entries:

$$\begin{aligned}
\phi_A =& 9 - 3 \cdot (\cos(k_x) + \cos(k_y)) + 4 \cdot \cos(2k_z) && (5.2.4)\\
\phi_B =& 6.25 - 3 \cdot \cos(k_x) - 2.5 \cdot \cos(k_y) - 1.5 \cdot \cos(2k_x) \\
&+ 4 \cdot \cos(2k_z) - 1 \cdot \cos(2k_x)\cos(k_y) && (5.2.5)\\
\phi_C =& 1 - 2 \cdot \cos(2k_x) - 1 \cdot \cos(2k_z) && (5.2.6)\\
t_{AB} =& 2 \cdot \sin(k_x)\sin(k_y) && (5.2.7)\\
t_{AC} =& -\,\mathrm{i}\sin(k_y) && (5.2.8)\\
t_{BC} =& -\,\mathrm{i}\sin(k_x) && (5.2.9)
\end{aligned}$$

The construction of the unlinked model is easier. To achieve an approximately equivalent diagonal projection as for the linked model, we can shift the NL rings from the plane $k_x = 0$ to the $k_x = \pm\pi$ plane and instead of centering them in the middle, we center them at the boundary of the plane.

Again we start with three flat bands and give the bands of orbitals p_x, p_y a dispersion with the shape of $\cos(2k_z)$. For both $k_x = k_y = 0$, we let the s-band intersect with the p_y-band to form two red NL rings in the plane $k_y = 0$. This is done by giving the s-band a $-\cos(k_x)$ shape. By further giving the p_x-band a $\cos(k)$ shape along k_x and k_y, we also find the NL rings in the $k_x = \pm\pi$ plane. So, we end up with the following model including hoppings by up to two primitive lattice vectors for the unlinked model:

$$\mathcal{H}_{\text{unlinked}} = \begin{pmatrix} \phi_A & t_{AB}^* & t_{AC}^* \\ t_{AB} & \phi_B & t_{BC}^* \\ t_{AC} & t_{BC} & \phi_C \end{pmatrix} \tag{5.2.10}$$

with the entries:

$$\phi_A = -6.6 + 2 \cdot \cos(k_y) + 3 \cdot \cos(2k_z) \tag{5.2.11}$$
$$\phi_B = 2 + 2 \cdot (\cos(k_x) + \cos(k_y)) + 3 \cdot \cos(2k_z) \tag{5.2.12}$$
$$\phi_C = -3.5 - 2 \cdot \cos(k_x) \tag{5.2.13}$$
$$t_{AB} = 2 \cdot \sin(k_x) \sin(k_y) \tag{5.2.14}$$
$$t_{AC} = -\mathrm{i} \sin(k_y) \tag{5.2.15}$$
$$t_{BC} = -\mathrm{i} \sin(k_x) \tag{5.2.16}$$

5.2.2. Nodal lines of the models

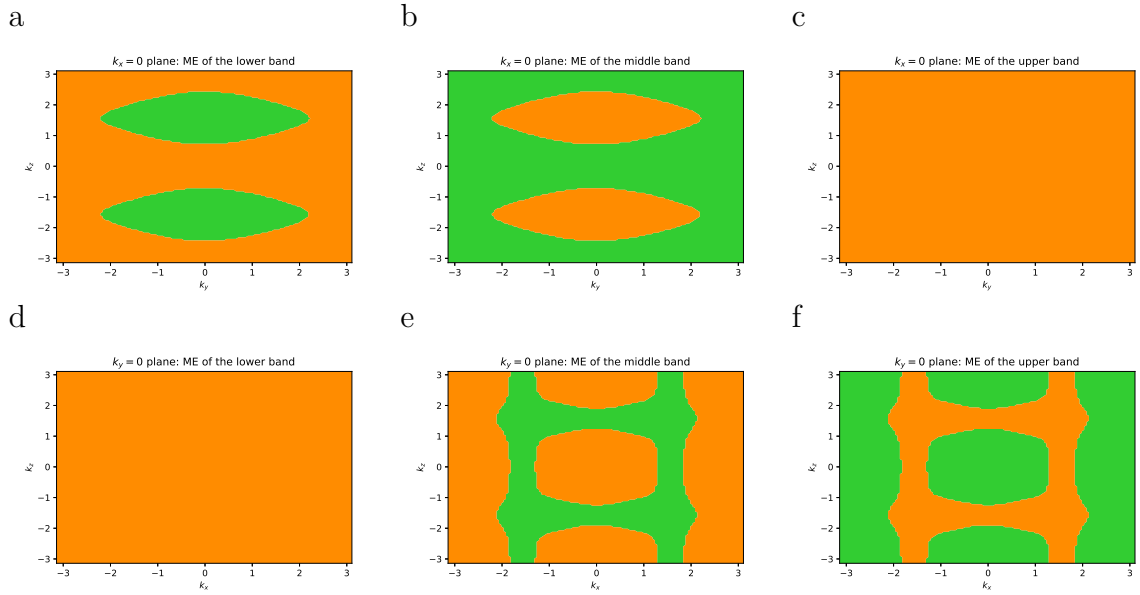

Figure 5.9.: Mirror eigenvalues for the high symmetry planes in the linked model. The different colors show the sing of the mirror eigenvalue and the boundaries between the colors indicate the position of the nodal lines. The upper three diagrams show the mirror eigenvalue for the $k_x = 0$ plane, and we see that we have two NL rings in the lower band gap. In the lower line there is the same for the $k_y = 0$ plane, where we have two NL rings (one of them at the k_z boundary of the BZ) and two nodal lines through the BZ in the upper band gap. The other high symmetry planes corresponding to $k_x = \pm\pi, k_y = \pm\pi$ show no changes in mirror eigenvalues.

We now have a closer look at the nodal-line structure of these models. One possibility to make nodal lines visible on a mirror symmetric plane, is to look at the eigenvalues of the mirror operator. We can calculate the mirror eigenvalues for each band individually. For a nodal line in the planes $k_x = 0, \pm\pi$, the mirror eigenvalue of $\hat{m}_x$ changes from $+1$ to -1 or vice versa for the lower two bands if we cross a nodal line in the lower band gap. In the case of a nodal line in the upper band gap the mirror eigenvalue changes for

the upper two bands. The same is true for the $k_y = 0, \pm\pi$ and the operator $\hat{m}_y$. We can apply this to our linked and unlinked model to check the nodal line structure.

For our models, having orbital basis (p_y, p_x, s) the mirror operators are the following:

$$\hat{m}_x = \begin{pmatrix} 1 & 0 & 0 \\ 0 & -1 & 0 \\ 0 & 0 & 1 \end{pmatrix} \qquad \text{and} \qquad \hat{m}_y = \begin{pmatrix} -1 & 0 & 0 \\ 0 & 1 & 0 \\ 0 & 0 & 1 \end{pmatrix} \tag{5.2.17}$$

We now apply this procedure to our two models and look at the mirror eigenvalues at specific planes and for the different bands. In the linked model, the only mirror eigenvalue changes occur for the planes $k_x = 0$ and $k_y = 0$ (Figure 5.9). For the unlinked case, we find the mirror eigenvalue changes in the $k_y = 0$ and the $k_x = \pm\pi$ planes (Figure 5.10).

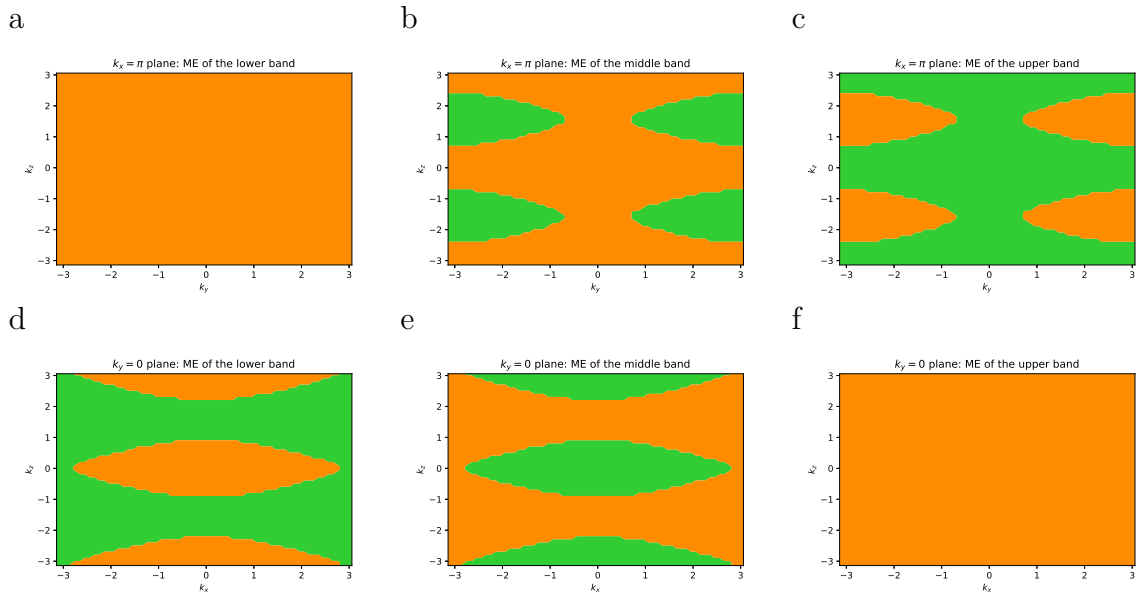

Figure 5.10.: Mirror eigenvalues for the high symmetry planes in the unlinked model. Again the colors represent the sing of the mirror eigenvalue and the boundaries the nodal lines. The upper line shows the results for the $k_x = \pi$ plane (due to the periodicity the $k_x = -\pi$ plane looks exactly the same). We find two NL rings in the upper band gap both at the boundary in k_y-direction. The lower three diagrams show the mirror eigenvalues on the $k_y = 0$ plane and we find two NL rings (one of them at the k_z boundary) in the lower band gap. The other high symmetry planes corresponding to $k_x = 0, k_y = \pm\pi$ show no changes in mirror eigenvalues.

Using these results from the mirror eigenvalues, we can also illustrate the nodal lines inside the three-dimensional BZ for both the linked and the unlinked model. By looking at the nodal lines along a diagonal, we can see the similarity of the surface BZ projections of the two models (Figure 5.11).

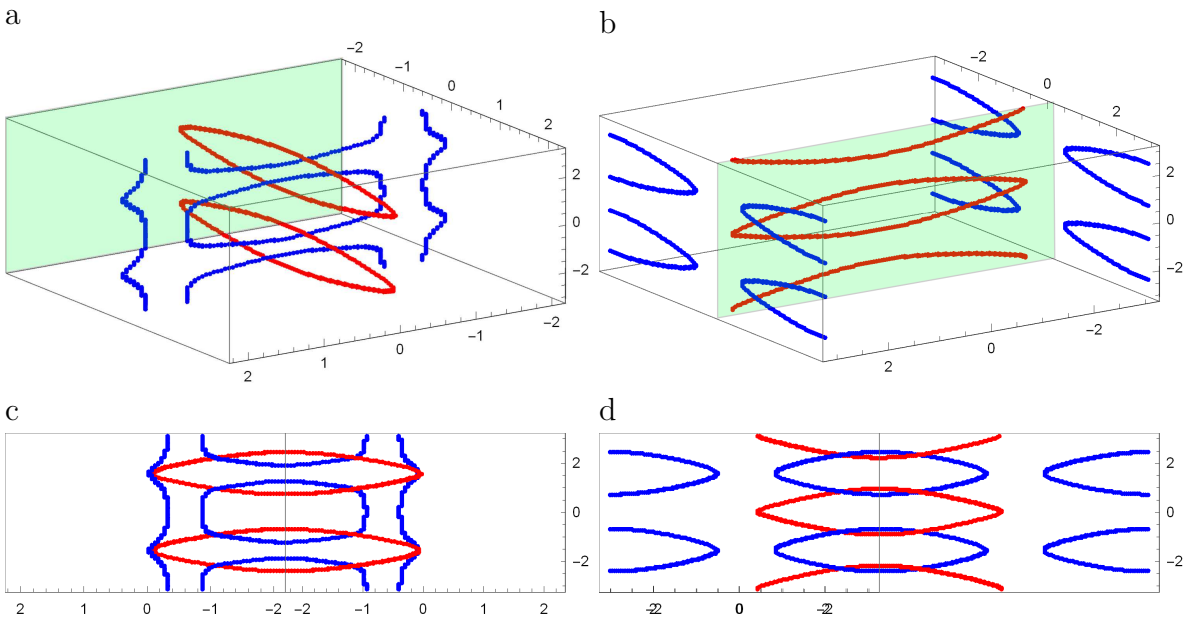

Figure 5.11.: Nodal lines inside the three-dimensional BZ for the linked and the unlinked model. Panel (a) shows the nodal-line structure of the linked model in the $3D$ BZ. Blue lines correspond to nodal lines in the upper band gap and red lines represent the nodal lines in the lower band gap. In panel (b) we see the nodal-line structure for the unlinked model. The transparent blue planes are not intersected by any nodal lines and are therefore taken for the calculation of the quaternion charge. Panels (c) (linked) and (d) (unlinked) show the same nodal-line structures projected along the diagonal and we can see the similarity between the two models. The main difference are the additional straight nodal lines along the k_z direction for the linked model. In addition, the red and blue lines are interchanged between the two models

5.2.3. Quaternion charge

As for the two-dimensional braiding model, we now look at the quaternion charge phase diagrams. Therefore, we have to define a one-dimensional version of the Hamiltonian along some threads through the BZ and we need the Hamiltonian to be real. The reality of the Hamiltonian, we again get by a constant unitary transformation.

We know that our Hamiltonian is $\mathcal{PT}$-symmetric. For the Hamiltonian to be real-symmetric, we need the $\mathcal{PT}$-symmetry to be represented as simple complex conjugation. Therefore, we look at what these symmetries explicitly do to our orbitals. The parity changes the sign of the p_x and p_y orbital, i.e. it is represented as a diagonal matrix with entries $(-1, -1, 1)$ on the diagonal. Furthermore, the time reversal symmetry is simple identity times complex conjugation (time reversal does not influence the orbitals). Then the $\mathcal{PT}$-symmetry of our system is represented the diagonal matrix $\mathrm{diag}(-1, -1, 1)$ times complex conjugation $\mathcal{K}$. We now search for a unitary transformation U of the $\mathcal{PT}$-

symmetry operator $\mathcal{O}$ such that:

$$\mathcal{O} \mapsto U\mathcal{O}U^\dagger = \mathcal{K} \text{ for: } \mathcal{O} = \begin{pmatrix} -1 & 0 & 0 \\ 0 & -1 & 0 \\ 0 & 0 & 1 \end{pmatrix} \mathcal{K} \tag{5.2.18}$$

We then easily find the transformation to be the following matrix:

$$U = \begin{pmatrix} \mathrm{i} & 0 & 0 \\ 0 & \mathrm{i} & 0 \\ 0 & 0 & 1 \end{pmatrix} \tag{5.2.19}$$

With this we can define the real-symmetric version of the (un)linked Hamiltonian as:

$$\tilde{\mathcal{H}}_{(un)linked}(k_x, k_y, k_z) = U\mathcal{H}_{(un)linked}(k_x, k_y, k_z)U^\dagger \tag{5.2.20}$$

We now do the same as for the quaternion charge in the two-dimensional model. As we are interested in the surface BZ projection along the diagonals, we chose the threads along the diagonal in the k_x-k_y-plane and treat k_z in the same way as we did for the tuning parameter t. In this model the projection along both diagonals is the same and we only need one family of paths and choose $\gamma_{\phi,(11)}$ in Eq. (5.1.8). For $\phi \in [-\pi, \pi]$ and $k_z \in [-\pi, \pi]$, we then find the $1D$ Hamiltonian to determine the quaternion charge along $k \in [-\pi, \pi]$ as:

$$\mathcal{H}_{1D,\phi,(un)linked}(k, k_z) = \tilde{\mathcal{H}}_{(un)linked}(\gamma_\phi(k), k_z) \tag{5.2.21}$$

The resulting topological phase diagrams of the linked and unlinked models are shown in Figure 5.12. Here, we do not restrict ourselves to conjugacy classes but really look at the charges including the sings. In that way it is possible to also see the orientations of the nodal lines. However, to be able to really see the charges and not only up to conjugacy, we need to fix the frames we take at the start positions to determine the charge. Therefore, we take a continuous choice of initial frames by choosing a plane inside the BZ which is not intersected by any nodal line (planes are indicated in Figure 5.11a,b) and starting all the threads at this plane. By this choice the initial frames differ from neighboring ones only by infinitesimal rotations. We were not able to do this in the two-dimensional braiding model, as there exists no such plane.

In the diagram for the unlinked model, we easily recognize the NL structure. We find the regions enclosed by red nodal lines (lower band gap) to have charge k and the ones enclosed by blue nodal lines (upper band gap) to have charge i. The orange regions are the ones where the red and the blue overlap and are enclosed by one nodal line of each color.

A bit more difficult to understand is the phase diagram for the linked model. We can understand the different phases in the following way. If we crossing a nodal line of charge i, we enter a region of charge i. If we then cross a nodal line of a different charge, e.g. charge k, we end up in a region of charge $\mathrm{j} = \mathrm{k} \cdot \mathrm{i}$. In this way it is easier to understand the phase diagram. We first look at the red nodal lines, they include the

orange and violet region. On the other hand, the blue nodal lines lie along the boundary between the orange and the violet regions as well as between the blue and the green regions. For a better insight, we can analyze the quaternion charge using the above convention by crossing nodal lines along a path starting at $k_z = 0, \phi = -\pi$ going along the $k_z = 0$ line until $\phi = 0$ and then increasing k_z to end up at $\phi = 0, k_z = \pi$. We start in the trivial (blue) region, then we first pass a nodal line of charge $-$i ending up in the dark green region. Again, we cross a blue nodal line but this time with opposite orientation, i.e. charge i, which leads again to a trivial region. Increasing k_z we first cross a red nodal line, giving a violet region of charge k. By the above convention we know that now crossing a nodal line of charge $-$i we end up in a region of charge $\mathrm{j} = -\mathrm{i} \cdot \mathrm{k}$ (orange). Crossing another blue nodal line this time with opposite orientation i we again are in the violet region and finally crossing a red nodal line with charge -k, we are back in the trivial (blue) region.

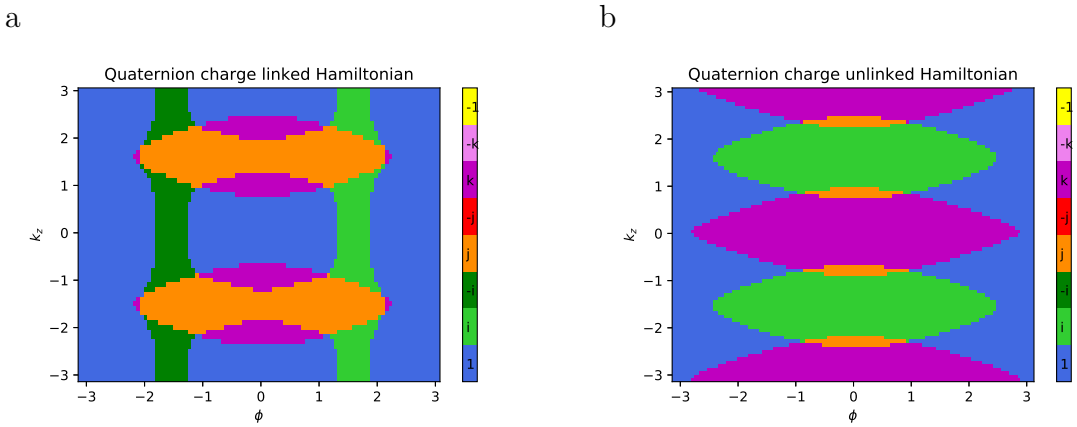

Figure 5.12.: Phase diagram of the quaternion charge for the linked and unlinked model. The different colors indicate the phases of different topological charge.

We can do this for arbitrary paths to determine all orientations of the nodal lines. Noteworthy here is the blue nodal lines crossing the whole BZ along k_z direction have the same orientation and are therefore not able to annihilate. This is the reason why we were not able to get rid of these lines during the construction. Furthermore, we unfortunately do not have a region with charge -1 and are not able to check our conjecture on these models.

5.2.4. Similarity of the models

One of the open questions is, if we are able to differentiate the linked and the unlinked model by only looking at the surface spectrum. Unfortunately, we are not as we will see in Section 7.2 and we are able to already suggest this similarity of the models using the quaternion charge.

To see this, we assume[4] a correspondence between the topological charges and the surface states. Then to be able to see the linking, we should already see a difference in the topological phase diagrams. The blue nodal lines crossing the BZ cannot annihilate because they have the same orientation[5], so we cannot get rid of the green regions in the phase diagram of the linked nodal lines (Figure 5.12a). But we could try to add these regions to the phase diagram of the unlinked model (Figure 5.12b). As in the unlinked model the middle NL ring is in the lower band gap (red), we try to add the nodal lines also in the lower band gap. To do so, we create a node-antinode pair of nodal lines crossing the BZ along the k_z-direction at the left end of the BZ. We then shift the nodal line with charge −k towards the middle until it lies close to the nodal line structure. At the same time the nodal line with charge +k crosses the BZ boundary and is shifted towards the nodal line structure from the right. By some deformation of the nodal line rings, we realize that we get the same regions as in the phase diagram for the linked model up to conjugacy classes. Only charges i and k are exchanged, i.e. nodal lines in the lower and the upper band gap switched. This can be seen in Figure 5.13.

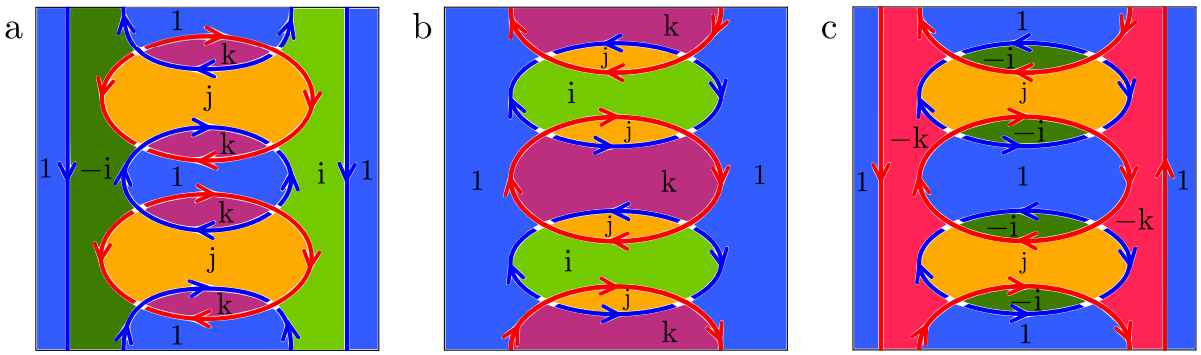

Figure 5.13.: Schematics of the topological phase diagram including orientations of the nodal lines. Panel (a) shows the nodal lines of the linked model including their orientations schematically. In addition the regions of different charges are indicated with colors. Panel (b) shows the same for the linked model. In panel (c) we added two straight nodal lines with different orientations to the unlinked model and then determined the regions of different charges. If we only consider the charges up to conjugacy, we can see that panel (a) and (c) look the same just with i and k exchanged.

Therefore, under the assumption of a direct correspondence between the surface states and the topological phases, we already know that it is not possible to tell if two NL rings are linked or not by only looking at the surface spectrum.

[4]Our results for the surface states of the different models suggest such a bulk-boundary correspondence. See Section 7.1.

[5]To determine the orientation of the nodal lines, we use the following convention. A nodal line moving from left to right has orientation − and the one moving from right to left has orientation +. Furthermore, we determine the topological region after crossing the NL by multiplying the charge before the NL with the invariant of the NL (±i, for blue NL and ±k for red NL) from the left.

6. Techniques to study models

In this chapter, we present the methods we use to study the surface states in the different models. First, we show the procedure to set up finite Hamiltonians in the slab geometry[1] using different edges. Then, we explain four different methods to visualize the surface states. The first three methods implement the actual band structure of the Hamiltonian whereas the last method flattens the bands while keeping the topology of the model unchanged.

6.1. Finite models

To be able to observe surface states, we first need to set up finite models in real space. This is done inside the x-y-plane[2]. In all models presented in Chapter 5, we consider the z-axis (for the $2D$ model Eq. (5.1.1) the parameter t and for the $3D$ models Eq.s (5.2.3) and (5.2.10) the third momentum-component k_z.) as a tuning parameter, and study the surface states for cuts at different positions along this axis. Inside the (k_x, k_y)-plane, we can consider different types of edges. We can either have open boundary conditions in the x or y directions, or we have open boundaries along one of the diagonals. For all the cases, the construction is done, using enlarged unit cells (compare Figure 6.1). A system that is infinite in one direction (momentum k) and has a width L in the other direction can then be interpreted as a periodic one-dimensional system with $3L$ orbitals on each site. So we can represent the finite system for each value of k_z or t, respectively, as a $3L \times 3L$-matrix of the following form:

$$\mathcal{H}_{\text{finite}}(k) = \begin{pmatrix} t^0 & t^{-1} & t^{-2} & t^{-3} & \cdots \\ t^1 & t^0 & t^{-1} & t^{-2} & \ddots \\ t^2 & t^1 & t^0 & t^{-1} & \ddots \\ t^3 & t^2 & t^1 & t^0 & \ddots \\ \vdots & \ddots & \ddots & \ddots & \vdots \end{pmatrix} \tag{6.1.1}$$

where t^n are 3×3 matrices representing the hopping amplitudes between different small unit cells. More precisely the element at position (α, β) in block t^n represents a hopping from orbital β in the small unit cell i to orbital α in the small unit cell $i - n$. The k-independent part of these hopping amplitudes corresponds to processes within the

[1] By this, we mean that the model has open boundary conditions along one direction (either along an axis or along a diagonal) and periodic boundaries along the other two directions.

[2] Compare to the procedure for graphene, e.g. Chapter 7 of Ref. [5].

enlarged unit cell while the part including an additional phase factor $e^{\pm imk}$ correspond to a hopping by $\pm m$ enlarged unit cells to the left.

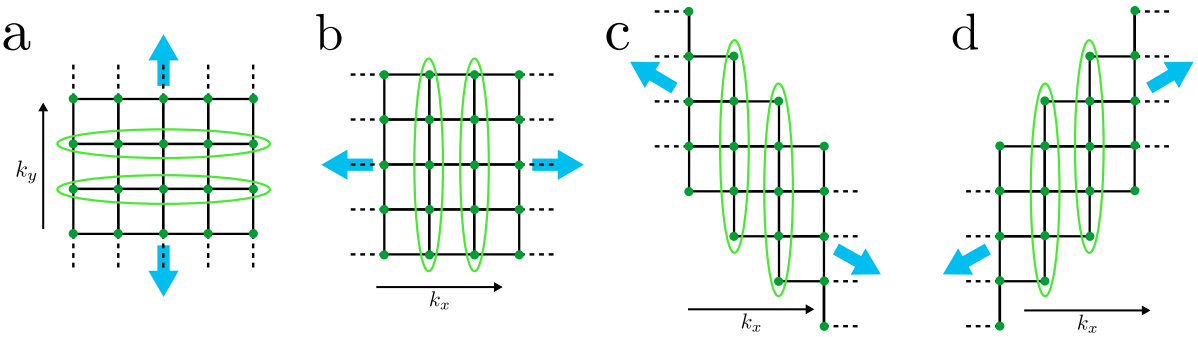

Figure 6.1.: Enlarged unit cells for the construction of the finite model. The green ellipses show the enlarged unit cells, each containing $L = 5$ original unit cells (represented as dark green dots. The blue arrows indicate along which direction the systems are periodic and thereby infinite.

To better understand this, we explicitly analyze two examples, one which is finite along an axis and the other finite along a diagonal. First, we construct the Hamiltonian matrix for the two-dimensional braiding model, with finite length in y-direction. For simple illustration, we here set $L = 5$, although in the numerical analysis in Chapter 7, we consider larger values. In this case, we have open boundary conditions with five sites in the y-direction and periodic ones in the x-direction. Therefore, we can still consider $k = k_x$ as a good quantum number. A hopping by m enlarged unit cells to the left then picks up a factor of e^{imk}. The Hamiltonian matrix is found by explicitly sketching the system with all the hopping amplitudes (Figure 6.2a). Using this, we find the following blocks depending on the tuning parameter t and the quantum number k in the one-dimensional BZ $[-\pi, \pi]$. For this geometry and the $2D$ Hamiltonian (Eq. 5.1.1), we find the following blocks in the slab geometry Hamiltonian Eq. (6.1.1):

$$
\begin{aligned}
t^0 &= \begin{pmatrix} f(t) & -\mathrm{i}e^{-\mathrm{i}k} & \mathrm{i}e^{\mathrm{i}k} \\ \mathrm{i}e^{\mathrm{i}k} & 0 & h_0(t) + h_1(t)e^{\mathrm{i}k} \\ -\mathrm{i}e^{-\mathrm{i}k} & h_0(t) + h_1(t)e^{-\mathrm{i}k} & 0 \end{pmatrix} \\
t^1 &= \begin{pmatrix} 0 & 0 & -\mathrm{i} \\ -\mathrm{i} & 0 & h_1(t) \\ 0 & 0 & 0 \end{pmatrix} \qquad t^{-1} = t^{1\dagger}
\end{aligned}
\tag{6.1.2}
$$

In exactly the same way, we find the Hamiltonian that is finite in x-direction and periodic in y-direction. For this case we have $k = k_y$ as a good quantum number and

find the following blocks for the Hamiltonian:

$$t^0 = \begin{pmatrix} f(t) & \mathrm{i}e^{-\mathrm{i}k} & -\mathrm{i}e^{\mathrm{i}k} \\ -\mathrm{i}e^{\mathrm{i}k} & 0 & h_0(t) + h_1(t)e^{\mathrm{i}k} \\ \mathrm{i}e^{-\mathrm{i}k} & h_0(t) + h_1(t)e^{-\mathrm{i}k} & 0 \end{pmatrix}$$
$$t^1 = \begin{pmatrix} 0 & 0 & \mathrm{i} \\ \mathrm{i} & 0 & h1(t) \\ 0 & 0 & 0 \end{pmatrix} \qquad t^{-1} = t^{1\dagger} \tag{6.1.3}$$

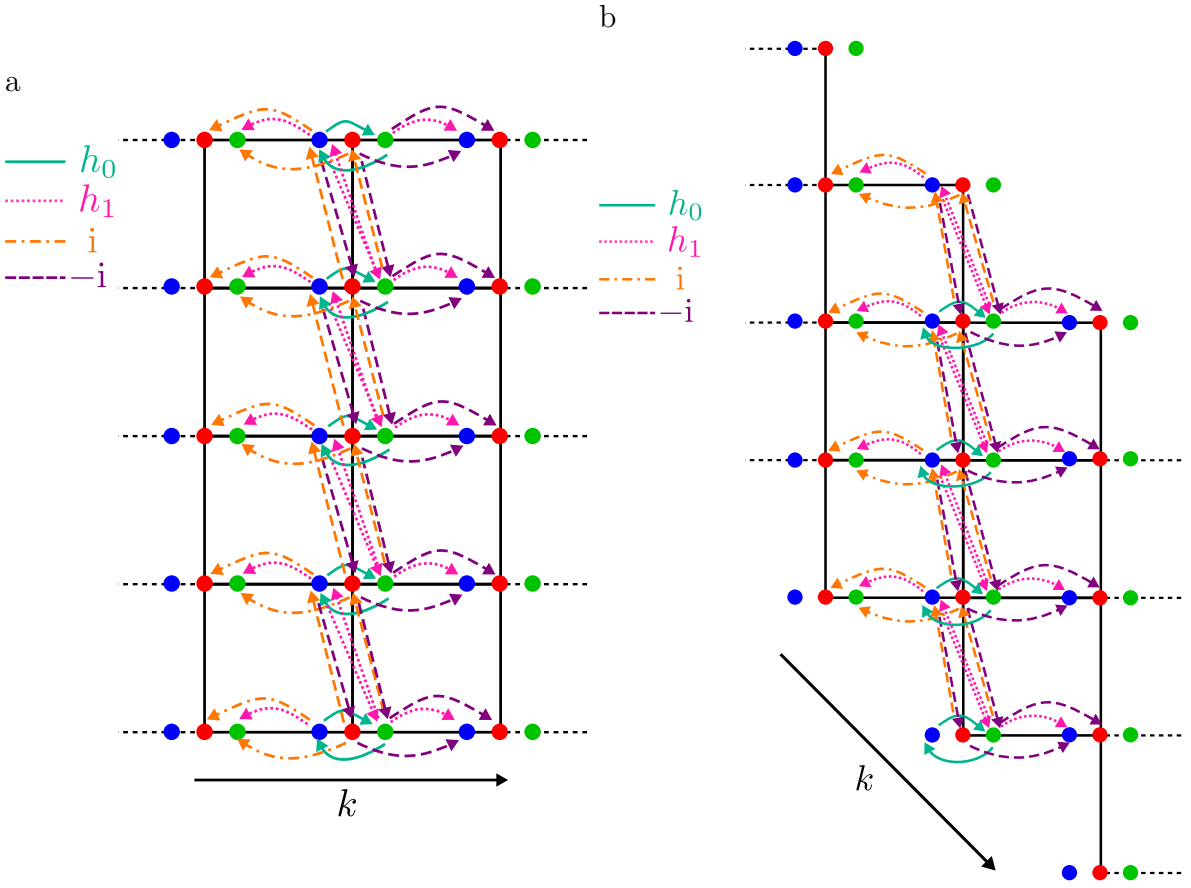

Figure 6.2.: Construction of the finite models. The blue, green and red dots represent orbitals A,B and C. Indicated by the different colors are the hopping amplitudes between all the orbitals for the two-dimensional braiding model (Eq. 5.1.1). Therefore we only consider the hoppings from the enlarged unit cell in the middle. Panel (a) shows the situation for the system finite in y-direction whereas the panel (b) sketches a model finite in the (11)-direction. From the figures we can read out the hopping blocks for the finite Hamiltonian. Hoppings that do not change layers correspond to the block t^0, whereas hoppings by n layers down (up) correspond to the blocks t^n (t^{-n}). The same can also be sketched for the $3D$-model but including many more hopping parameters.

For the diagonals the procedure is the same but now the enlarged unit cell is always shifted by one smaller unit cell up or down for the construction (compare Figure 6.1c,d). We look at this in more detail for the system finite along the (11)-diagonal and infinite along $(1\bar{1})$. Figure 6.2b shows what the system looks like with these shifted enlarged unit cells. We define the enlarged unit cells such that they consist of L smaller unit cells along the y-axis. In this setting we can take $k = k_- = \frac{1}{\sqrt{2}}(k_x - k_y)$ as a good quantum number in which the system is infinite. Again, we draw all the hopping amplitudes and are then able to read out the blocks in the Hamiltonian.

$$\begin{aligned} t^0 &= \begin{pmatrix} f(t) & 0 & 0 \\ 0 & 0 & h_1(t) \\ 0 & h_1(t) & 0 \end{pmatrix} \\ t^1 &= \begin{pmatrix} 0 & 0 & \mathrm{i}\left(e^{\mathrm{i}k} - 1\right) \\ \mathrm{i}\left(e^{\mathrm{i}k} - 1\right) & 0 & h_1(t)\left(e^{\mathrm{i}k} + 1\right) \\ 0 & 0 & 0 \end{pmatrix} \qquad t^{-1} = t^{1\dagger} \end{aligned} \tag{6.1.4}$$

We also find the hopping blocks for the system which is finite along the $(1\bar{1})$-diagonal and infinite along (11). Now, we choose $k = k_+ = \frac{1}{\sqrt{2}}(k_x + k_y)$ as the good quantum number and the blocks look as follows:

$$\begin{aligned} t^0 &= \begin{pmatrix} f(t) & 0 & 0 \\ 0 & 0 & h_1(t) \\ 0 & h_1(t) & 0 \end{pmatrix} \\ t^1 &= \begin{pmatrix} 0 & -\mathrm{i}e^{-\mathrm{i}k} & -\mathrm{i} \\ -\mathrm{i} & 0 & h_1(t) \\ -\mathrm{i}e^{-\mathrm{i}k} & h_1(t)e^{-\mathrm{i}k} & 0 \end{pmatrix} \qquad t^{-1} = t^{1\dagger} \end{aligned} \tag{6.1.5}$$

For the three-dimensional models in the linked (Eq. 5.2.3) and the unlinked (Eq. 5.2.10) case, we are mainly interested in the system that is finite along the (110)-diagonal. In addition, we also looked at the linked model finite along the x-axis. The resulting finite models for these Hamiltonians can be found in Appendix B.

Having constructed these finite models, we now look at three different techniques to find the surface states of them.

6.2. Energy spectra

A simple technique to detect surface states is to compare the energy spectra of open vs. periodic boundary conditions along some momentum ϕ. This method is often used for the zero modes in graphene, e.g. [36].
For simplicity, we denote by ϕ (instead of k_x, k_y or k) the continuous momentum in the $1D$ system with enlarged unit cell, i.e. ϕ is the surface BZ momentum. To find the energy spectrum for the open boundary conditions for a specific value of k_z and t, respectively, we take the Hamiltonian matrix of the finite system (Eq. 6.1.1) and

diagonalize it inside the one-dimensional surface BZ (so for ϕ in $[-\pi, \pi]$) for the fixed value of k_z or t, respectively. This is done numerically using Python for discrete values of ϕ. We then end up with $3L$ energy bands inside the surface BZ.

We want to compare these energy bands to the projection of the infinite model onto the surface BZ (Figure 6.3). The projection along the x-(y-)axis, corresponds to a finite system along the x-(y-)axis. We again do this numerically using Python. Therefore, we take discrete values of ϕ and k_p where by ϕ we denote the surface BZ momentum and by k_p the momentum along which we do the projection. For the projection along the k_p-axis, we diagonalize the 3×3-Hamiltonian matrix (Eq. 5.1.1, 5.2.3 or 5.2.10, respectively) for the first value of k_p and all the values of ϕ in the $1D$ surface BZ $[-\pi, \pi]$ and plot the three resulting energy bands inside this BZ. We then do the same for all other fixed values of k_p in the same plot and arrive at the surface BZ projection with $3N$ bands (N is the number of discrete values along k_p).

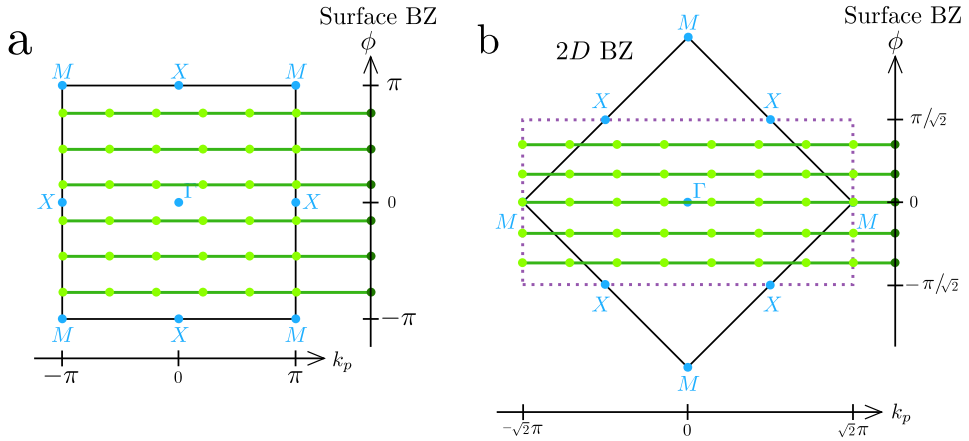

Figure 6.3.: Different surface BZ projections. Panel (a) shows the construction of the surface BZ projection along either the x- or the y-axis for $N = 5$. The light green dots on one green line are all projected onto the same position in the surface BZ (dark green dot). In panel (b) the same is shown for the diagonal projection along either diagonal and for $N = 7$. Here the purple rectangle represents the same dots as the original BZ. The factors of $\sqrt{2}$ in the surface BZ in panel (b) are dropped in the analysis in Chapter 7, by implicitly replacing $a \mapsto \sqrt{2}a$

In the case of the diagonal surface BZ projection, we have to keep in mind that the surface BZ extends only from X to M to X but we have to include the whole BZ in the projection. This we do by replacing the square BZ (black in Figure 6.3) with the purple dotted rectangle. Each point in the original BZ then corresponds to exactly one point in the purple rectangle, and the volume of the rectangle is $(2\pi)^2$ as the one of the square BZ. We again take ϕ and k_p as defined above and do the construction in the same way as for the projections along one of the axes. The only difference is that now we have ϕ in the range $\left[-\pi/\sqrt{2}, \pi/\sqrt{2}\right]$ and therefore k_p in the range $\left[-\sqrt{2}\pi, \sqrt{2}\pi\right]$. A possible choice for ϕ and k_p is shown in Figure 6.3. Later, in the plots of the projected spectrum, we

replace the original lattice parameter a by $a' = \sqrt{2}a$ and set this new lattice parameter a' to unity. With this we again find the surface BZ momenta ϕ in the range $[-\pi, \pi]$.

We can now choose some fixed values of k_z and t[3], and compare the plot of the finite system with the surface BZ projection. In both plots we should clearly find the bulk bands with energy gaps. The surface states we find as additional lines inside these energy gaps of the finite system but not in the projection of the infinite system. These additional lines, i.e. the surface states, typically occur between two band nodes. An example for this method can be found in Figure 6.4

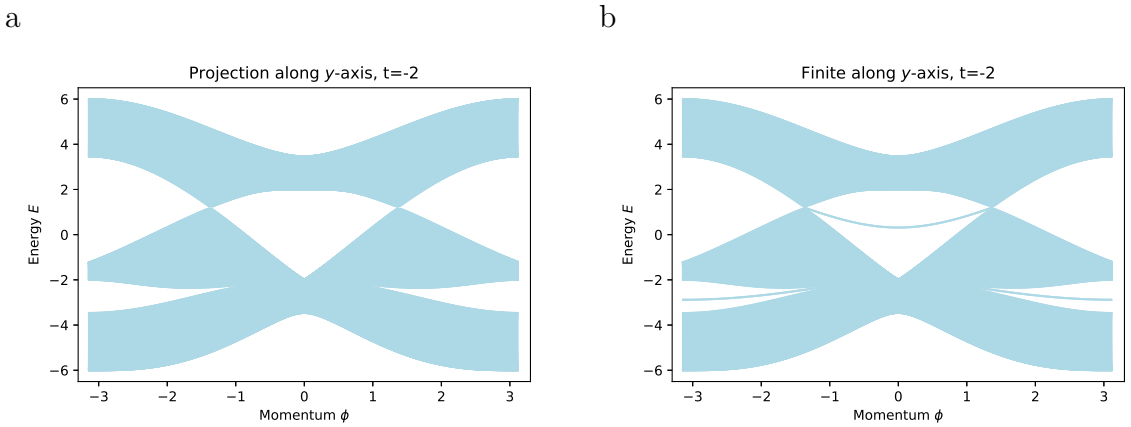

Figure 6.4.: Example for the comparison of open vs. periodic boundary conditions for the $2D$ braiding model at $t = -2$. Panel (a) shows the spectrum of the infinite Hamiltonian projected along the y-axis. In panel (b) we see the spectrum of a finite Hamiltonian with 100 layers along the y-direction. We clearly see one additional line in the upper band gap in the middle and one in the lower band gap on the boundaries of the surface BZ, in the case of open boundary conditions. Each of these lines corresponds one surface state on each end of the system.

Unfortunately this method is not able to clearly resolve energy bands representing surface states that lie close to the bulk bands, and is unable to visualize surface states lying within the bulk bands. Therefore, we present a second technique that uses the surface spectral function.

6.3. Surface spectral function

The second technique, we present, is based on plotting the surface spectral function to detect surface states and therefore allows us to visualize certain surface states that lie close to or within the bulk energy spectrum. Up to now we treated a state to have a specific energy and momentum. To overcome the discreteness of the numerically

[3]Later in the results, we will also choose arbitrary paths in the surface BZ, specified by coordinates (ϕ, t) and (ϕ, k_z), respectively.

computed spectra of finite systems, we assign each state ψ at momentum k and energy ε_k a Lorentzian-smeared spectral function $A_\psi^\eta(\varepsilon, k)$ where η is the energy smearing factor[4]. This spectral function is then defined as:

$$A_\psi^\eta(\varepsilon, k) = \frac{1}{\pi} \frac{\eta}{(\varepsilon - \varepsilon_k)^2 + \eta^2} \tag{6.3.1}$$

In the limit $\eta \to 0$ this represents the delta-distribution $A_\psi^\eta(\varepsilon, k) = \delta(\varepsilon - \varepsilon_k)$.

We can now define the surface spectral function at each point (ε, k) in the following way:

$$A(\varepsilon, k) = \sum_{\psi @ k} \text{Probability}(\psi \text{ is at the edge}) \cdot A_\psi^\eta(\varepsilon, k) \tag{6.3.2}$$

$$= \sum_{\psi @ k} \sum_{\text{orbitals } \alpha} |\psi_{i=\text{edge}}^\alpha|^2 A_\psi^\eta(\varepsilon, k) \tag{6.3.3}$$

where the sum over all ψ at some specific k is the sum over all eigenstates of the finite system at this momentum k. The second sum appearing in the second line is over all the orbitals at the site i = edge corresponding to one of the two edges and ψ_i^α is the probability amplitude of the state for being on site i in orbital α. For most of the points (ε, k) the value of the function is very close to zero. The first factor in the sum in Equation (6.3.3) is very small for all states that are not localized close to the edge, while the second factor is close to zero if the energy ε is not in a close neighborhood of an eigenvalue of the Hamiltonian. This implies that the surface spectral function only attains a significant value at some (ε, k) if there is a state well localized at the surface for this momentum and energy.

We can use this technique to visualize the surface states in contour plots. In our models we again do this for specific values of k_z and t, respectively, and later for paths in the surface BZ, using the finite Hamiltonian matrices of the form (6.1.1). With Python we first define a meshgrid of discrete points for k in the one-dimensional BZ as well as for ε in the range of energy of the Hamiltonian. At each point of the meshgrid, we calculate the surface spectral function (6.3.3). The value of this function is then represented by different colors, very low values are represented in blue and higher ones in yellow/green. For a good choice of the steps in the mesh grid and the parameter η, we can see the surface states as clear yellow/green areas in the contour plots (Example shown in Figure 6.5).

By again looking at the formula for the surface spectral function (6.3.3), we see that there is a second possibility to get large values at some points (ε, k). If the dispersion of a bulk band at a certain k_p is very narrow and centered at energy ε_p, then the bands cumulatively lead to a noticeable value of $A(\varepsilon_p, k_p)$ which becomes visible in the plot (light blue lines in Figure 6.5).

[4]This smearing is often used in ARPES experiments, e.g. Ref. [37].

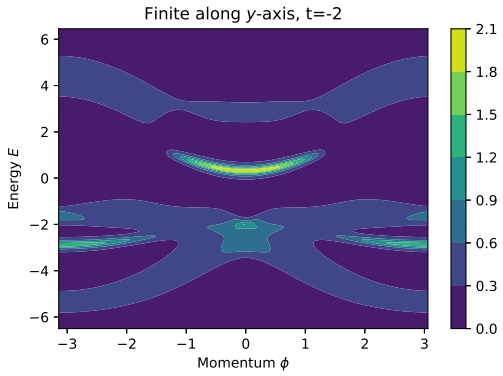

Figure 6.5.: Example for the method using the surface spectral function. The value of the surface spectral function indicated by the colorbar is expressed in arbitrary units. As in Figure 6.4, we look at the $2D$ braiding model for $t = -2$. We clearly see the same surface states as by using the first method (green lines) but, in addition, we see in a slightly lighter blue then the background some signatures of the bulk bands corresponding to positions where the bulk bands are quite narrow.

With these two presented methods we are only able to visualize real surface states. In real materials and also in theoretical models, it is possible that the surface states start to hybridize with the bulk states. Sometimes surface states lying in the bulk energy spectrum strongly hybridize with the delocalized bulk states while keeping an increased spectral weight at the boundary. This feature we refer to as a surface resonance. The last method, we present for the non-flattened Hamiltonian, is also able to recognize surface resonances instead of only clear surface states, provided that the hybridization with the bulk states is not too strong.

6.4. Inverse participation ratio

To detect the surface resonances (localized over many sites at the boundary), we can use the inverse participation ratio (IPR)[5]. In general the IPR is defined as follows:

$$I_{\psi}^{(2n)} = \frac{\sum_{\text{sites } i} \left(\sum_{\text{orbitals } \alpha} |\psi_i^{\alpha}|^2\right)^n}{\sum_{\text{sites } i} \sum_{\text{orbitals } \alpha} |\psi_i^{\alpha}|^2} \tag{6.4.1}$$

for $n \geq 2$, for the analysis of the surface spectrum in Chapter 7 we set $n = 2$. Different to the method for the surface spectral function Eq. (6.3.3), we here sum over all sites i and orbitals α rather than only over those lying at the edges. For normalized wave functions ψ, the denominator equals 1.

We now compare the value of this IPR for localized vs. not localized states. Without loss of generality we look at a system with N sites and only one orbital per site.

[5]These technique was often used for the Anderson localization, e.g. in Ref. [38].

In the situation where the states are delocalized, we know from the normalization that $\sum_i |\psi_i|^2 = 1$. If the state is uniformly distributed over all sites, this implies that $|\psi_i|^2 = \frac{1}{N}$, therefore $|\psi_i|^{2n} = \frac{1}{N^n}$ and we find for the IPR:

$$I_\psi^{(2n)} = \frac{\sum_i \frac{1}{N^n}}{\sum_i \frac{1}{N}} = \frac{1}{N^{(n-1)}} \tag{6.4.2}$$

From this formula we conclude that if a state is delocalized the IPR gets very small for large N and by doubling the number of sites it should get smaller by a factor of $2^{(n-1)}$.

We now compare this to the situation where a state is localized with a localization lengths of s sites (in our case at the boundary). If we are in a situation where the localization length is larger then our system size ($s > N$), we observe the same as if the state was delocalized. In contrast, for the situation $s < N$, we still have $\sum_i |\psi_i|^2 = 1$ but now we have a weight of $\frac{1}{s}$ for the sites over which the state is localized and a weight of 0 for all other sites. Therefore, we find that $|\psi|^{2n} = \frac{1}{s^n}$, independent on N.

This implies that independent on the number of sites $N > s$, the value of the IPR will be approximately:

$$I_\psi^{(2n)} = \frac{\sum_{\text{localization sites } i} \frac{1}{s^n}}{\sum_i \frac{1}{N}} = \frac{1}{s^{(n-1)}} \tag{6.4.3}$$

We now are able to visualize the states in a graph. For a fixed parameter k_z o t and for each momentum k inside the surface BZ, we diagonalize the Hamiltonian in slab-geometry (6.1.1) to get the eigenvectors and eigenvalues. We then calculate the IPR for each eigenstate and plot the eigenvalues ε_ψ on the x-axis and the IPR $I_\psi^{(2n)}$ on the y-axis (Figure 6.6a). In this plot we observe the bulk bands with an IPR of $1/N^{(n-1)}$, i.e. close to zero, and at a higher IPR the surface states or resonances. A perfect localized (surface) state, we see at an IPR of 1 and the closer to 1 the IPR of a state gets, the shorter is its localization length.

A second method to visualize the IPR is to fix k_z or t, respectively and then calculate the IPR for each $\phi \in [-\pi, \pi]$[6]. We then plot the surface BZ momentum on the x-axis and the energy on the y-axis, whereas the IPR is indicated by different colors. Dark blue represents a value close to 0 and yellow close to 1. This method is shown in Figure 6.6b and we can clearly see the whole band structure in dark blue and some lines in lighter blue/yellow indicating the surface states/resonances as well as their localization length.

Now, we have seen three different techniques to visualize surface states for finite systems. All these methods consider the actual Hamiltonians, as presented in Chapter 5, which exhibit a large dispersion of the bulk energy bands. Sometimes it is impossible to find surface states of a system using any of these methods. Therefore, we introduce a last method where we, instead of the actual band dispersion, use spectrally flattened bands in the Hamiltonian. This is possible as by flattening the band to some fixed energies we do not alter the topology of the models.

[6]We will later also use this method for other paths through the surface BZ.

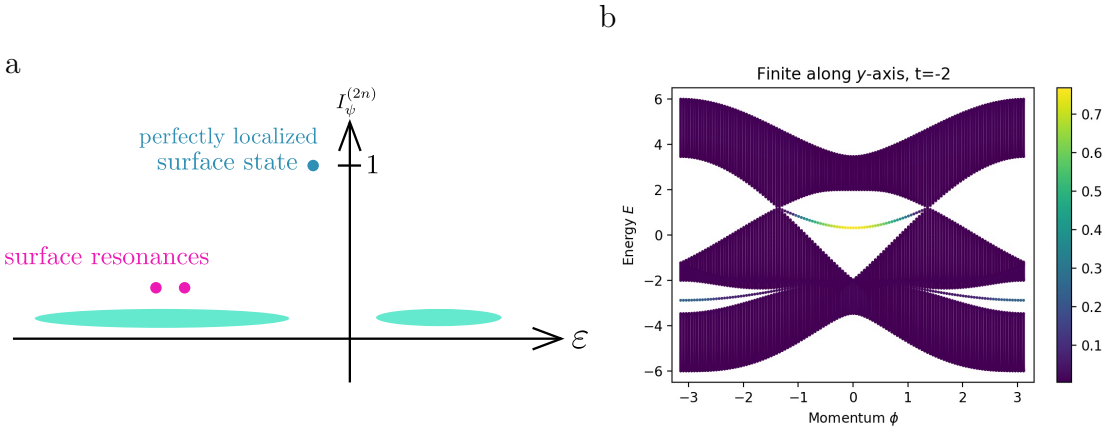

Figure 6.6.: Detect surface states/resonances using the IPR. Panel (a) shows the schematics of this method. The bulk bands are shown as light blue ellipses. In addition we show surface resonances (pink) with an IPR of around 0.2 and a single-site localized surface state (dark blue) with IPR equal 1. Panel (b) shows the method applied on the $2D$ braiding model for the system finite along the y-axis for $t = -2$. In yellow we can see the same surface states as with the methods presented before.

6.5. Spectral flattening

For this last technique, we want to flatten the bands of the Hamiltonian, similar to Eq. (4.2.4) and then use the first technique where we compare the periodic vs. open boundary conditions. In the case of the flattened Hamiltonian the system with periodic boundaries exhibits three flat bands at energies $-1, 0$ and 1, whereas for the open boundary conditions, we observe some additional bands occurring between these flat bands. To find these spectra, we first flatten the Hamiltonian, then Fourier transform it to a lattice in the slab geometry along some axis to finally determine the eigenvalues of this one-dimensional Hamiltonian numerically. We use this method only along the diagonals, therefore, we choose the system to be finite along the (11)-diagonal and can easily transform the final formula for the system finite along the $(1\bar{1})$-diagonal.

We start with our tight binding Hamiltonian in the reciprocal space $H(k_x, k_y, k_z)$ (or in the $2D$-system $H(k_x, k_y, t)$). First, we flatten this Hamiltonian and then consider a finite system in slab geometry along the (11)-direction.

To find the flattened Hamiltonian, we diagonalize the Hamiltonian for N discrete values of k_x and k_y in the range $[-\pi, \pi]$. The z-direction, we treat as a continuous parameter. For all of these N^2 points, we find three eigenvalues ε_α and the corresponding eigenstates $|u^\alpha_{k_x,k_y}\rangle$. To get the Hamiltonian with flat bands, we take the list of eigenvalues $\tilde{\varepsilon}^\alpha = (-1, 0, 1)$. We then define the flattened Hamiltonian $Q(k_x, k_y, k_z)$ as:

$$Q(k_x, k_y, k_z) = \sum_\alpha |u^\alpha_{k_x,k_y}\rangle \tilde{\varepsilon}^\alpha \langle u^\alpha_{k_x,k_y}| \tag{6.5.1}$$

To construct the Hamiltonian on a finite lattice, we have to take the discrete 2D inverse Fourier transform[7] w.r.t. k_x and k_y for a fixed k_z (for simplicity we write $Q(k_x, k_y, k_z)$ as $Q(k_x, k_y)$.

$$Q_{n_1,n_2} = Q\left(-\pi + n_1 \cdot \frac{2\pi}{N}, -\pi + n_2 \cdot \frac{2\pi}{N}\right) \tag{6.5.2}$$

Doing the Fourier transform (for each component of the matrix separately), we get the real Fourier coefficients: q_{m_1,m_2}. These can be interpreted as the amplitude of a hopping by m_1 unit cells along the x-direction and m_2 along the y-direction.

Using these hopping amplitudes, we can set up the Hamiltonian in the slab geometry with enlarged unit cells. For simplicity at this point we choose the number of sites of one enlarged unit cell in the slab geometry to be equal to the number of discrete points, we choose to perform the flattening, i.e. the number of layers $L = N$. We then find the following block Hamiltonian consisting of $N \times N$ blocks of the size 3×3.

$$\mathcal{H}_{slab} = \begin{pmatrix} t^0 & t^{-1} & t^{-2} & t^{-3} & \cdots \\ t^1 & t^0 & t^{-1} & t^{-2} & \ddots \\ t^2 & t^1 & t^0 & t^{-1} & \ddots \\ t^3 & t^2 & t^1 & t^0 & \ddots \\ \vdots & \ddots & \ddots & \ddots & \vdots \end{pmatrix} \tag{6.5.3}$$

where we consider blocks t^l for $l = -N/2, \ldots, 0, \ldots, N/2$. For perfectly flat bands, we actually would need to include infinite neighbor hopping, but by the properties of the Fourier transform the coefficients are periodically and will decrease until $N/2$ and then increase again which motivates us to perform the indicated truncation. Using the hopping amplitudes q_{m_1,m_2}, we set up a tight-binding model finite in (11)-direction and infinite along the $(1\bar{1})$-diagonal with momentum denoted by $\tilde{k}$. This is done by choosing the blocks t^l as follows:

$$t^{\pm l} = \sum_{a=-N/2}^{N/2} q_{a,-(a\pm l)} e^{-i\tilde{k}a} = \sum_{a=-N/2}^{N/2} q_{a,-a\mp l} e^{-i\tilde{k}a} \tag{6.5.4}$$

where for each block we include all the hopping amplitudes of up to $N/2$ enlarged unit cells to the left and the right.

Now we want to do a coordinate transformation to be able to interpret these hopping amplitudes as Fourier transforms in the first coordinate.

$$q(x, y) \to r(s, t) \tag{6.5.5}$$

We take $s = x$ and $t = x + y$ to only have the a in the first coordinate. The inverse transformation is then $x = s$ and $y = t - s$. So we can write:

$$t^l = \sum_{a=-N/2}^{N/2} r_{a,-l} e^{-i\tilde{k}a} = R(\tilde{k}, -l) \tag{6.5.6}$$

[7]For the definition of the Fourier transform, see Appendix C.

To get a simple formula, we now want to write out all the Fourier transforms:

$$R(\tilde{k}, -l) = \frac{1}{N^2} \sum_{k_x} \sum_{k_y} \sum_{a} Q(k_x, k_y) \exp(i\tilde{k}a) \exp(ik_x a) \exp(ik_y(-a-l)) \tag{6.5.7}$$

$$= \frac{1}{N^2} \sum_{k_x} \sum_{k_y} \sum_{a} Q(k_x, k_y) \exp(ia(k_x - k_y - \tilde{k})) \exp(-ik_y l) \tag{6.5.8}$$

$$= \frac{1}{N} \sum_{k_x} \sum_{k_y} Q(k_x, k_y) \delta_{ky, kx-\tilde{k}} \exp(-ik_y l) \tag{6.5.9}$$

$$= \frac{1}{N} \sum_{k_x} Q(k_x, k_x - \tilde{k}) \exp(-il(k_x - \tilde{k})) \tag{6.5.10}$$

where we have used that the Kronecker delta can be written as $\delta_{mn} = 1/N \sum_k \exp(k(n-m))$ to get rid of the summation over a.

Now, we have a simple Fourier-transform-like formula to find the Hamiltonian at each point $\tilde{k}$ which we then apply to obtain the flattened spectrum of the finite Hamiltonian in slab geometry. Its implementation requires us to find the flattened Hamiltonian for discrete points k_x and $\tilde{k}$ as $Q(k_x, k_x - \tilde{k})$. At these discrete points the Hamiltonian is given by Eq. (6.5.3) with the following blocks:

$$t^l(\tilde{k}) = \frac{1}{N} \sum_{k_x} Q(k_x, k_x - \tilde{k}) \exp(-il(k_x - \tilde{k})) \tag{6.5.11}$$

We are now able to implement the flattened Hamiltonian in slab geometry finite along the (11)-diagonal in Python depending on the surface BZ momentum $\tilde{k}$ and for fixed tuning parameters along the z-direction (k_z or t). To visualize the surface states, we diagonalize the $3N \times 3N$-matrix (Eq. 6.5.3) for some discrete values of $\tilde{k} \in [-\pi, \pi]$. We then plot the the eigenvalues at $\tilde{k}$ vs. the momenta $\tilde{k}$ and end up with the spectrum of the flattened Hamiltonian.

In the same way we can also get the Hamiltonian finite along the $(1\bar{1})$-diagonal, and we then end up with the following formula for the blocks:

$$t^l(\tilde{k}) = \frac{1}{N} \sum_{k_x} Q(k_x, k_x - \tilde{k}) \exp(il(k_x - \tilde{k})) \tag{6.5.12}$$

where only the sign of the exponent in the exponential function is changed.

With this technique it is possible to really visualize the topology of the Hamiltonian without a possible hybridization of the surface states with the bulk and we should be able to detect the surface states also for systems, we cannot see them using the three methods presented above. Figure 6.7 shows an example of this method applied on the $3D$ unlinked model.

a

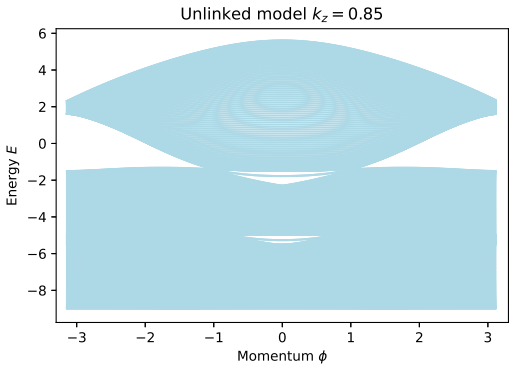

b

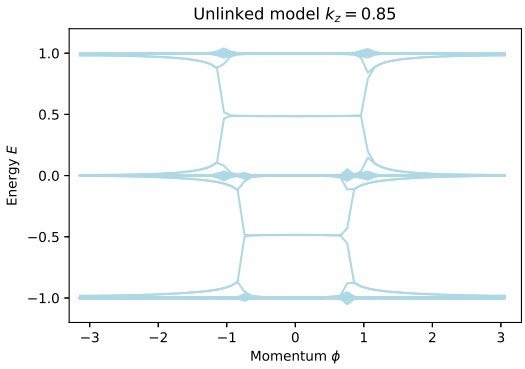

Figure 6.7.: Example for the method using the spectrally flattened Hamiltonian. Panel (a) shows the spectrum of the unlinked Hamiltonian finite along one of the diagonals for $k_z = 0.85$. In panel (b), we see the same system using the spectrally flattened Hamiltonian. Using the spectral flattening, we see the surface states clearer and over a larger range of surface BZ momenta ϕ.

7. Results on the behavior of the edge states

In this chapter, we apply the techniques presented in the previous chapter on the two-dimensional and three-dimensional models from Chapter 5. For all the finite models, we set the number of sites[1] to $L = N = 100$. Thereby, we concentrate on the open questions from Section 4.4. First, we want to find a relation between the numerically calculated quaternion charge and the occurrence of surface states. Further, we compare the linked and the unlinked model, and try to find a way to differentiate them by looking solely on their surface spectrum. Last, we check our conjecture on the phase with quaternion charge -1.

7.1. Correspondence between the surface states and the quaternion charge

In this section, we establish a correspondence between the quaternion charge in some region in the topological phase diagram (Figures 5.7 and 5.12) and the occurring surface states in this region. We have already seen a correspondence in Chapter 3 on the elementary $1D$ models for topological insulators with flat bands. There ,we have observed that charge i leads to one edge state per edge between the upper two bands, charge k between the lower two bands, and charge j between the highest and lowest bands. For charge -1 we found three edge states per edge, one of them crossing the middle band. This crossing, we further establish in the Section 7.3.

To check the correspondence, we look at the surface states along different paths $\gamma(\phi, t)$ in the surface BZ of the $2D$ model, where t is the tuning parameter of the model and ϕ the well defined momentum in the slab geometry. We consider one path for each termination to cover all the possible topological phases. For the system that is finite along the y-axis (which has a spectrum equivalent to that of the system finite along the x-axis), we take a path at $t = 0$ over the range of ϕ from $-\pi$ to π. In the model that is finite along the (11)-diagonal, we take again the path along ϕ for $t = 0$. For the last termination (finite along the diagonal $(1\bar{1})$, we take a path along t from -10 to 10 for a fixed value of $\phi = \pi/2$. The paths are indicated by white lines in Figure 7.1.

[1] This choice is justified in Appendix D.

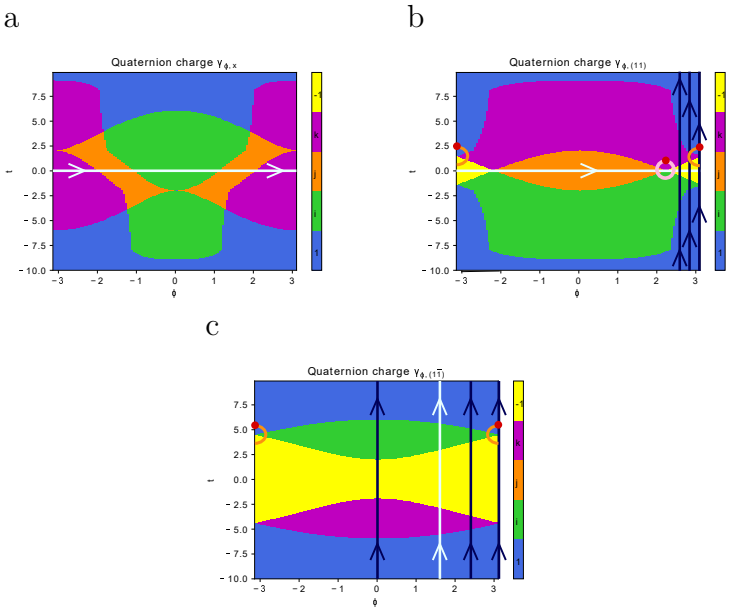

Figure 7.1.: Topological phase diagrams of the $2D$ model with indicated paths used to analyze the topological bulk-boundary correspondence and to check our conjecture on the phase with charge -1. Panel (a) shows the topological phase diagram with indicated paths for the system finite along the y-axis, (b) for the system finite along the (11)-diagonal and (c) along the $(1\bar{1})$-diagonal. The white paths are used to find the correspondence between the surface states and the quaternion charge in this section, the black paths and the closed orange and pink paths are used as examples for our conjecture on the phase with topological charge -1 in Section 7.3

We now use all four techniques[2] presented in the previous chapter to analyze the surface states along these paths, starting with the system finite along the y-axis. For all the models studied in slab geometry, there is a left-right symmetry for the edges, i.e. the surface spectrum at both edges are identical. Therefore, when counting the surface states, we focus only on the states localized near one edge, ignoring the other edge.

In Figure 7.1a, we again find the topological phase diagram with the indicated path along ϕ for $t = 0$. Staring from $\phi = -\pi$ going to $\phi = \pi$, we find the following regions:

$$\text{k (violet)} \to \text{j (orange)} \to \text{i (green)} \to \text{j (orange)} \to \text{k (violet)} \tag{7.1.1}$$

Figure 7.2 shows the surface states for the chosen path through the phase diagram. By comparing the open vs. the periodic boundary conditions, we find a surface state in the lower band gap (red lines) for ϕ in the ranges $[-\pi, -1.2]$ and $[1.2, \pi]$. In addition, we observe one surface state in the upper band gap for ϕ approximately in the range $[-2.1, 2.1]$. If we compare this to the charges inside the surface BZ along this path, we

[2]The spectral flattening we only apply for the two diagonals, as for the system finite along the y-axis, we can clearly see the surface states with the other methods.

conclude that in the violet region (charge k), we find a surface state in the lower band gap, in the green region (charge i), we find one in the upper band gap and in the orange region, we observe one in each band gap. So the observed bulk-boundary correspondence matches our expectations from the observations on the $1D$-model, except for the phase with charge j, which we further elaborate using the linked and unlinked model towards the end of the section. Also by looking at the spectral function and the IPR, we can clearly find the same surface states as yellow regions in the plots.

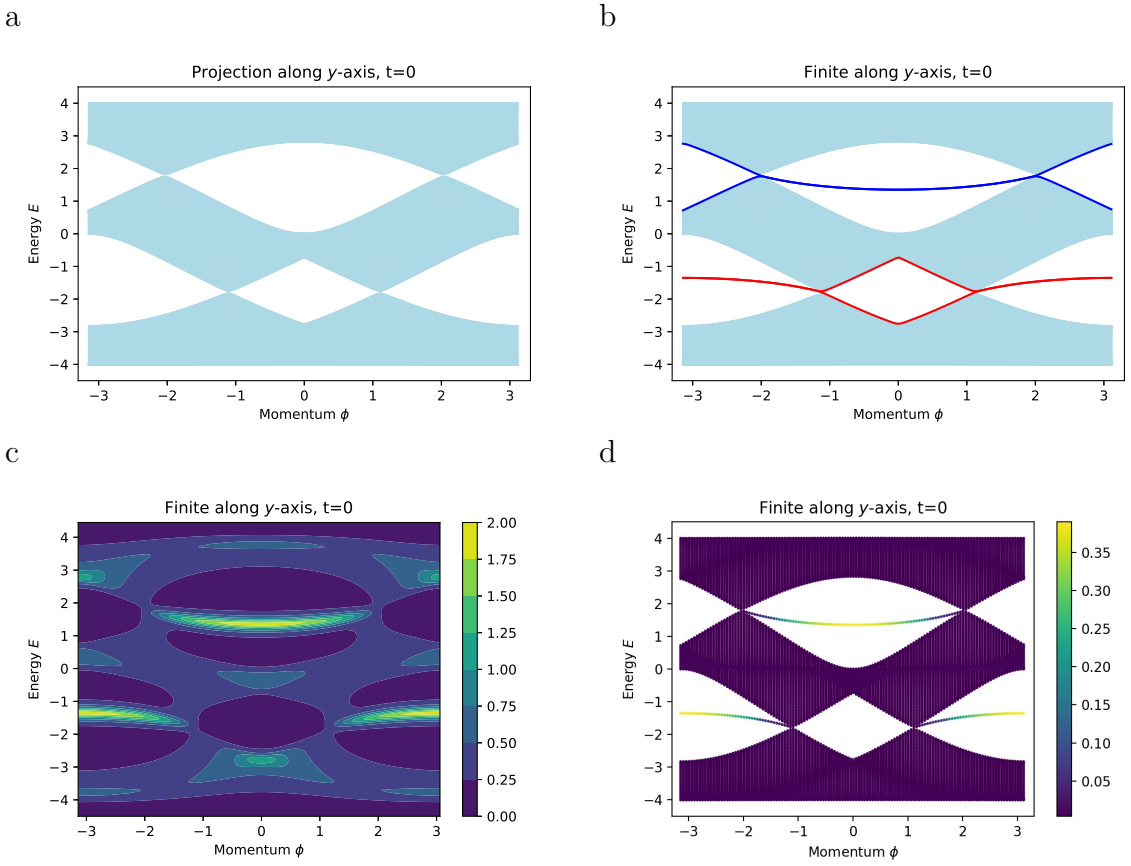

Figure 7.2.: Surface states in the $2D$ model for a finite system along the y-axis and for a fixed value of the tuning parameter $t = 0$. Panel (a) and (b) represent the first method, where we compare open and periodic boundary conditions, (a) shows the projection along the y-axis (periodic) and (b) shows the finite system. The red (blue) lines indicate the bands N,$(N + 1)$ ($2N$,$(2N + 1)$) when numbered from lowest to highest energy, i.e. the states around the filling fraction of 1/3 (2/3). Panel (c) shows the spectral function with values in arbitrary units, and panel (d) shows the IPR of each state.

For the system that is finite along the (11)-diagonal the path through the phase diagram is indicated in Figure 7.1b. Again, we go along ϕ for the value $t = 0$. Along this

path, we find the following topological charges:

$$-1 \text{ (yellow)} \rightarrow \text{j (orange)} \rightarrow -1 \text{ (yellow)} \tag{7.1.2}$$

The surface states for this path are shown in Figure 7.3.

Here, we observe one surface state in the lower band gap and one in the upper band gap both for ϕ approximately in the range $[-\pi, -2.2]$ and $[2.2, \pi]$ by comparing the open and periodic boundaries. When looking at the surface spectral function, we observe these surface states only in light green, but we see an additional one (actually there are two on top of each other, one per end of the system) at zero energy over the whole range of momenta ϕ. This is also confirmed by looking at the IPR plot. We clearly see the surface states at energy zero with an IPR of 1, i.e. perfectly localized. In the flattened spectrum (panel e), we cannot see these surface states because they lie completely inside the middle bulk bands. So in the yellow region, we find three surface states one in each band gap and one in the center of the middle band. In the orange region, we only observe the surface state lying inside the bulk band.

The correspondence in this termination perfectly agrees with the observation in the $1D$-model where we also observed one edge state in the middle between the lowest and the uppermost band for the charge j and three edge states for the charge -1. However, by comparing the regions with charge j in this termination vs. in the system that is finite along the y-axis, we do not observe the same correspondence, and will further study this mismatch using the linked and unlinked models in $3D$.

The spectrum of this system in the slab geometry (finite along the (11)-diagonal for $t = 0$) suggests a particle hole symmetry, i.e. a symmetry that relates the state at $E(\phi, k_p)$ to a second state at $-E(\phi, -k_p)$. By ϕ we denote the surface BZ momentum indicated in the plots and by k_p the momentum along the projected diagonal (compare Figure 6.3). To find the symmetry, we first need the Hamiltonian in these coordinates. Therefore we use the following coordinate transformation (re-scaled such that both ϕ and k_p are in the range $[-\pi, pi]$)[3]:

$$\phi = k_x - k_y \qquad \text{and} \qquad k_p = \tfrac{1}{2}(k_x + k_y - \pi) \tag{7.1.3}$$

from this we get the inverse transformation:

$$k_x = \tfrac{1}{2}(2k_p + \pi + \phi) \quad \text{and} \quad k_y = \tfrac{1}{2}(2k_p + \pi - \phi) \tag{7.1.4}$$

[3]The spectrum of the Hamiltonian $\mathcal{H}_{2D}$ at $t = 0$ is actually not antisymmetric around $(k_x, k_y) = (0, 0)$ but around $(\pi/2, \pi/2)$. This we correct by shifting the origin in the transformation below. Nevertheless we therefore do not really have a particle-hole symmetry but only a particle-hole-like symmetry.

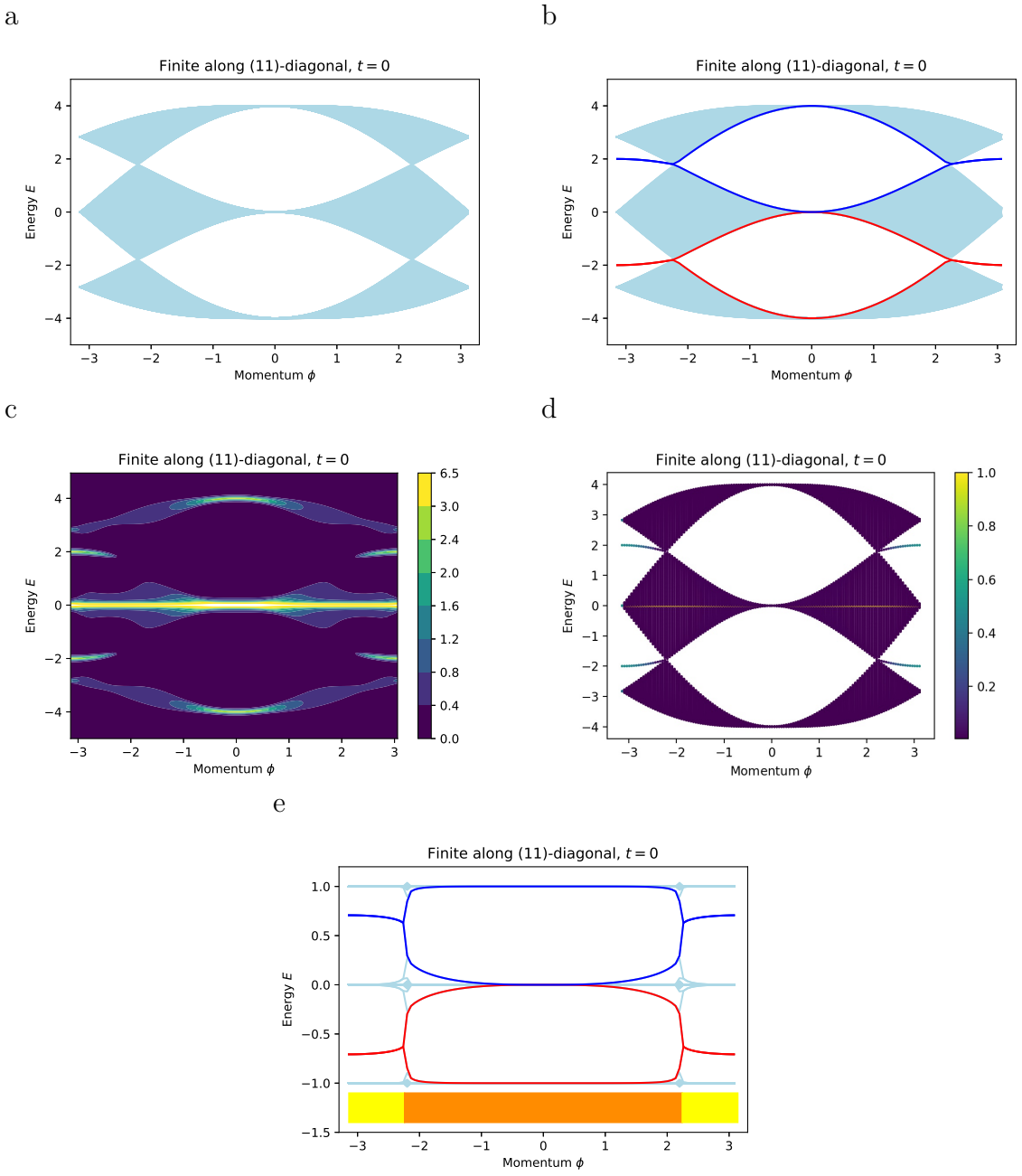

Figure 7.3.: Surface states in the $2D$ model for a finite system along the (11)-diagonal and for a fixed value of the tuning parameter $t = 0$. Panels (a)-(d) show the same methods as in Figure 7.2 with a small difference that this time the red (blue) lines correspond to the bands $(N-1)$,N ($(2N+1)$,$(2N+2)$), i.e. the states just below (above) the filling fraction of 1/3 (2/3). In addition, we have the flattened spectrum of the Hamiltonian in panel (e) with the same color scheme as in (b). The color bar at the bottom indicates the quaternion charge of the region we are in.

Indeed, we see that for $t = 0$ the Hamiltonian (Eq. 5.1.1) simplifies as the functions

$f(t)$ and $h_0(t)$ vanish. This means that we only have nearest neighbor hopping but no on site potential or on site hoppings. In the above diagonal coordinates, we then find the Hamiltonian as:

$$\mathcal{H}_{t=0}(\phi, k_p) = \begin{pmatrix} 0 & 2\mathrm{i}\sin\left(\frac{\phi}{2}\right)e^{-\mathrm{i}k_p} & -2\mathrm{i}\sin\left(\frac{\phi}{2}\right)e^{\mathrm{i}k_p} \\ -2\mathrm{i}\sin\left(\frac{\phi}{2}\right)e^{\mathrm{i}k_p} & 0 & 4\mathrm{i}\cos\left(\frac{\phi}{2}\right)e^{\mathrm{i}k_p} \\ 2\mathrm{i}\sin\left(\frac{\phi}{2}\right)e^{-\mathrm{i}k_p} & -4\mathrm{i}\cos\left(\frac{\phi}{2}\right)e^{-\mathrm{i}k_p} & 0 \end{pmatrix} \tag{7.1.5}$$

To get the desired particle-hole-like symmetry of the spectrum, we need the following transformation of the Hamiltonian to hold:

$$\mathcal{P}\mathcal{H}_{t=0}(\phi, k_p)\mathcal{P}^{-1} = \mathcal{H}_{t=0}(\phi, -k_p) \tag{7.1.6}$$

The corresponding symmetry operator can then be found as:

$$\mathcal{P} = \begin{pmatrix} 1 & 0 & 0 \\ 0 & 1 & 0 \\ 0 & 0 & 1 \end{pmatrix} \cdot \mathcal{K} \tag{7.1.7}$$

where $\mathcal{K}$ represents the complex conjugation operator.

Using this particle-hole-like symmetry, we see that the additional surface state inside the middle bulk band needs to lie exactly at zero energy throughout the whole surface BZ. If it was not at energy zero but at a finite value of ε there must be a second state at energy $-\varepsilon$, as it is the case for the other surface states with energy approximately 2.

The last termination for the $2D$-model we look at is finite along the $(1\bar{1})$-diagonal. Here, we analyze the spectrum along a path from $t = -10$ to $t = 10$ for the value of $\phi = \pi/2$ (indicated in Figure 7.1c). Starting at -10 along this path, we observe the following phases:

$$1 \text{ (blue)} \to \text{k (violet)} \to -1 \text{ (yellow)} \to \text{i (green)} \to 1 \text{ (blue)} \tag{7.1.8}$$

Figure 7.4 shows the surface states for this path using the different methods. Comparing the open vs. periodic boundary conditions, we can only suggest that there is a surface state in the lower as well as the upper band gap for t approximately in the range $[-3, 3]$. The same two surface states, we also observe in the IPR plot. Looking at the spectrally flattened Hamiltonian, the surface states become easier to detect. For t in the range $[-6, -2.5]$, we find one surface states in the lower band gap. Then for $t \in [-2.5, 2.5]$, we can see three surface states, one of them crossing the middle band, in agreement with our conjecture about the phase with charge -1[4]. Finally for t approximately in $[2.5, 6]$, we see one surface states in the upper band gap. Knowing that these states should exist, we can also observe them in the spectral function (panel c).

[4]Here, in contrast to the $1D$-model it is not really one surface state passing through the middle band but a more complicated situation where one surface state merges into the middle band after another surface state has been ejected from the middle band to the other band gap.

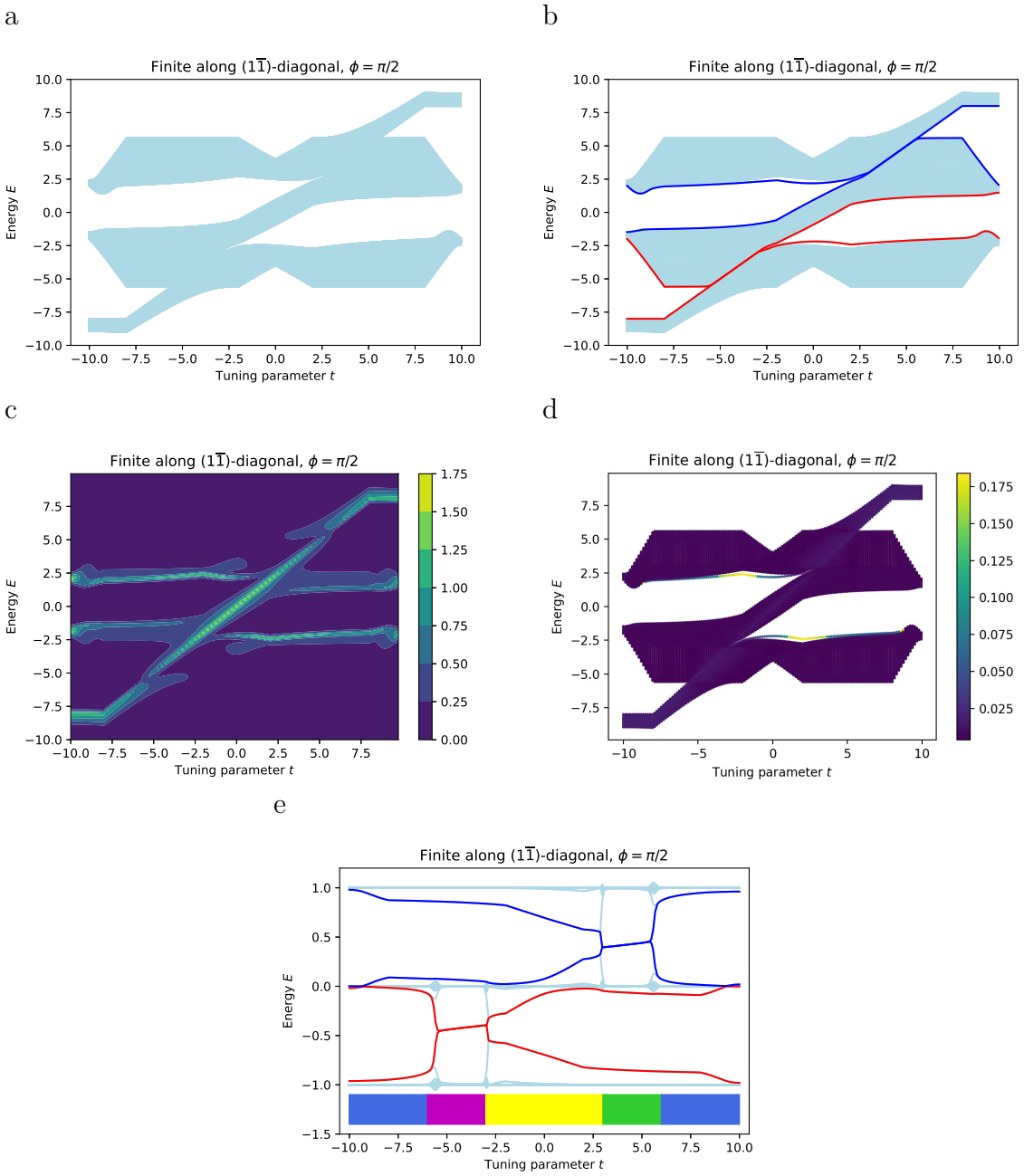

Figure 7.4.: Surface states in the $2D$ model for a finite system along the $(1\bar{1})$-diagonal and for a fixed value of the momentum $\phi = \pi/2$. Panels (a)-(e) show the same methods as in Figure 7.3 but the colors in (b) and (e) are again taken as in Figure 7.2

Again these observations are in a good agreement with the correspondence found in the $1D$-model. The trivial phase of charge 1 leads to no surface states, the phase of charge k (i) is manifested by a surface state in the lower (upper) band gap and in the region of charge -1, we can observe three surface states, namely one in each band gap and one of them crossing the middle band, i.e. changing from one band gap to the other.

What is left now is to further establish the expected surface states for the phase of charge j. Therefore, we consider the linked and unlinked models. In these models, we find the charge j by fixing $\phi = 0$ and taking a path along $k_z \in [-\pi, \pi]$ (see Figure 7.6). Looking at the spectrally flattened Hamiltonian for this path in the two models, we suggest that in most of the cases the region with charge j exhibits one surface states in the upper and one of them in the lower band gap (Figure 7.5).

a b

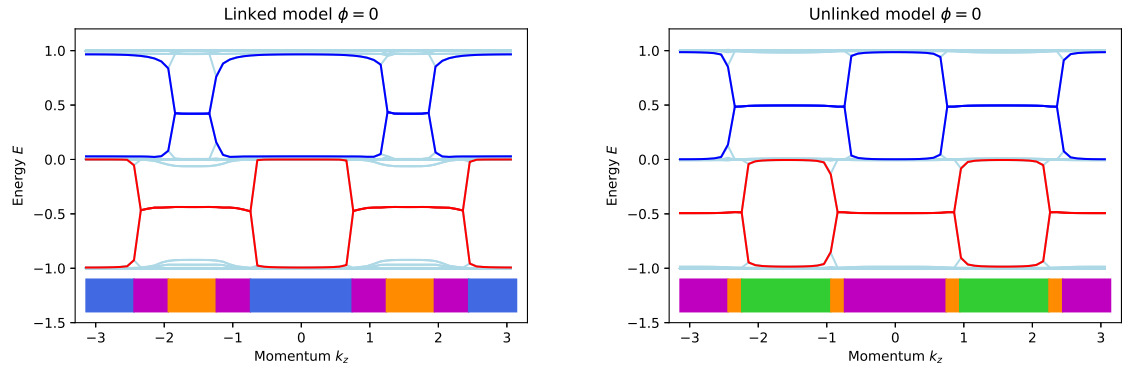

Figure 7.5.: Surface states in the $3D$ models finite along one of the diagonals for a fixed value of the momentum $\phi = 0$. Panel (a) shows the results for the linked model and panel (b) for the unlinked one. The surface states are compatible with the bulk-boundary correspondence deduced from studying the $1D$ and $2D$-models.

Using the above results, we conclude with the following correspondence generalized from the one-dimensional model to higher dimensions:

- charge 1 (blue): no surface states
- charge i (green): one surface state in the upper band gap
- charge k (violet): one surface state in the lower band gap
- charge j (orange): either one surface state in each band gap or one surface state inside the middle band
- charge -1 (yellow): three surface states and at least one in each band gap

The ambiguity of the surface states for charge j can be understood from the two possible interpretations of the phase with charge j. We can either interpret the charge j as $\mathrm{k} \cdot \mathrm{i}$, i.e. a superposition of the charges i and k leading to one surface state in each band gap, or we interpret it as the phase with a π Berry phase for the uppermost and lowest band (as we did in the one-dimensional model), leading to one surface state between these two bands.

Having established a simple bulk-boundary correspondence between the non-Abelian topological charge and the surface states mainly using the $2D$ braiding model, we now have a closer look at the linked and unlinked models in $3D$.

7.2. Linked versus unlinked model

In this section, we try to find a difference between the surface spectrum[5] of the linked and the unlinked model. Therefore, we again consider different closed paths in the surface BZ of the models (Figure 7.6). For both models, we take comparable paths to be able to investigate a difference between the models. These paths are chosen in a way that they enclose one or two overlays of nodal lines[6] and such that by going along the paths, we observe the same topological phases in the same order in both models.

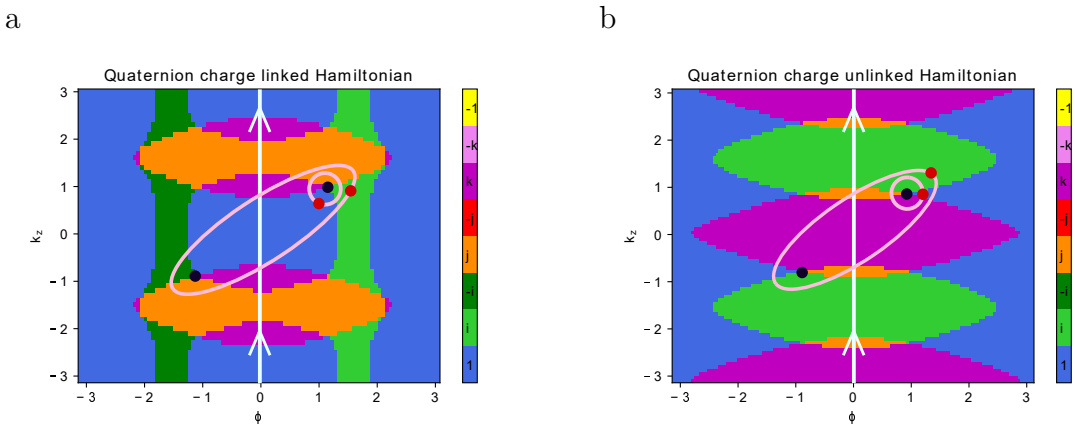

Figure 7.6.: Topological phase diagrams of the $3D$ model with indicated paths used for the analysis. Panel (a) shows the topological phase diagram and the chosen paths for the linked model, panel (b) for the unlinked model. The white line indicates the path chosen in Section 7.1 to determine the bulk-boundary correspondence for the topological charge j. The pink circle and ellipse show the paths we take to compare the models. Indicated by the black dots are the overlays of two nodal lines that are enclosed by the paths.

Before analyzing the surface states along these chosen paths, we have a look on how the different methods work in this more complicated models. Therefore we take a path along $\phi \in [-\pi, \pi]$ for the fixed value of $k_z = 1.5$. From the established bulk-boundary correspondence for this non-Abelian charge, we expect one surface states in each band

[5]The method used in experimental physics to probe the band structure, the angle-resolved photoemission spectroscopy (ARPES) is essentially a surface probe, in which injected photons enter the materials to a depth of only few atomic layers. It is therefore easier to detect the materials surface states rather then the true bulk spectrum and a correspondence between the linking, and the surface spectrum would be helpful to detect materials with linked nodal lines.

[6]By overlay, we mean that one nodal line lies on top of the other nodal line such that one of them changes its charge from $\pm$i ($\pm$k) to $\mp$i ($\mp$k).

gap in the linked model for $\phi \in [-2.2, 2.2]$ and one surface states in the upper band gap for $\phi \in [-2.4, 2.4]$ for the unlinked model. Figure 7.7 shows all presented techniques applied to the linked model and Figure 7.8 applied to the unlinked model.

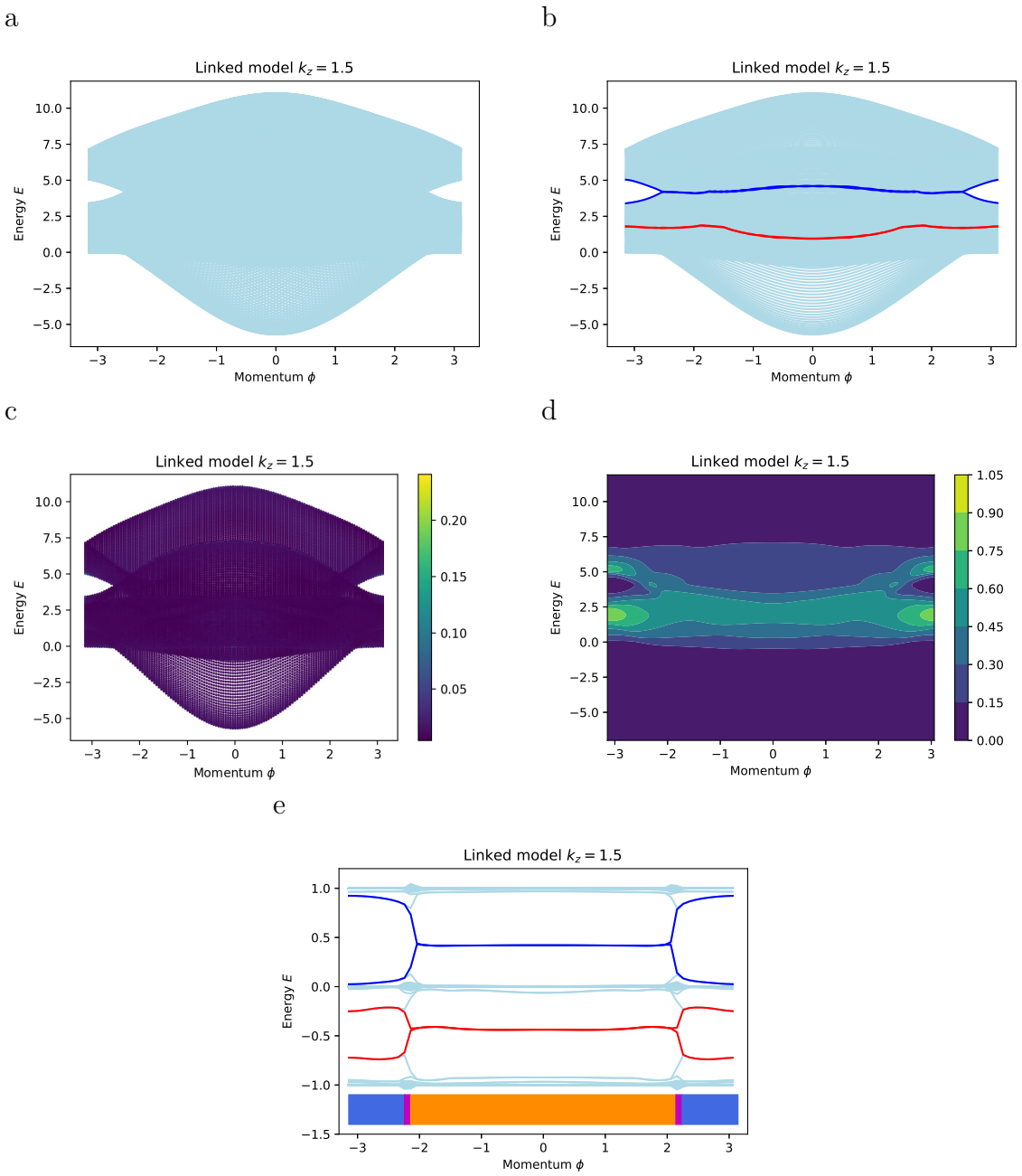

Figure 7.7.: All techniques applied to the linked model, finite along one of the diagonals and for a fixed value of $k_z = 1.5$. Panels (a)-(e) show the same methods as Figure 7.3.

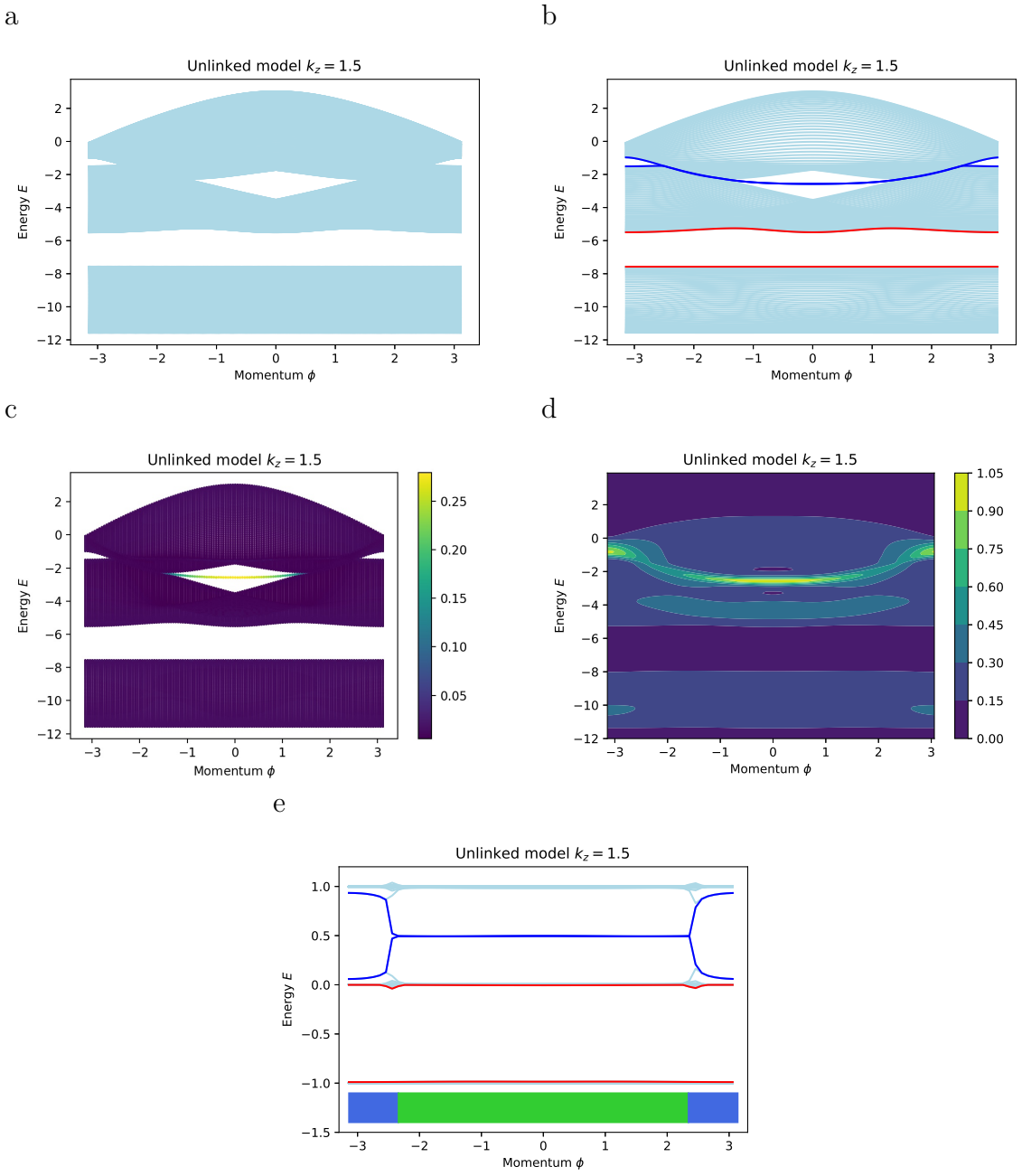

Figure 7.8.: All techniques applied to the unlinked model, finite along one of the diagonals and for a fixed value of $k_z = 1.5$. Panel (a)-(e) show the same methods as Figure 7.3.

For the linked model all methods except the spectral flattening completely fail to show any signature of surface states. However this is a feature of our specific model with linked nodal lines where the dispersion of the bulk bands prevents the existence of well-formed energy gaps and not a general signature of the linking of nodal lines. Indeed, after applying the spectral flattening, we find the surface states we expect from the formulated bulk-boundary correspondence. In the case of the unlinked model, we are

able to detect two surface states using the comparison of the open vs. periodic boundary conditions, the IPR method and the spectral function. Nevertheless it is not completely clear between which values of ϕ these states occur. Again the spectral flattening reveals exactly the expected behavior of the surface states.

To analyze the surface states along the paths shown in Figure 7.6, we first need a good representation of these paths. The path enclosing only one overlay we take as a circle, and to enclose the two overlays we use an ellipse. Like this we can easily parameterize these paths with a cyclic parameter $t \in [0, 2\pi]$. For the circle in both models, we find the following representation of the paths as two component vectors, both starting in the trivial region (blue).

$$\gamma_{1,\text{linked}} = \begin{pmatrix} 1.2 + 0.5 \cdot \cos(t - \frac{5}{8}\pi) \\ 1 + 0.5 \cdot \sin(t - \frac{5}{8}\pi) \end{pmatrix} \qquad \gamma_{1,\text{unlinked}} = \begin{pmatrix} 0.9 + 0.5 \cdot \cos(t) \\ 0.9 + 0.5 \cdot \sin(t) \end{pmatrix} \tag{7.2.1}$$

where the first component is the surface BZ momentum ϕ and the second component is the third momentum k_z, i.e. the two component vectors encode points (ϕ, k_z) in the $2D$ surface BZ.

For the ellipses, we take the simple parameterization using the two semi-axes instead of the radius, but we in addition have to rotate the ellipses by an angle of $\alpha = \pi/4$. We then find the following parameterization, taking the starting point inside the green region:

$$\gamma_{2,\text{linked}} = \begin{pmatrix} \cos(\alpha) & -\sin(\alpha) \\ \sin(\alpha) & \cos(\alpha) \end{pmatrix} \cdot \begin{pmatrix} 1.9 \cdot \cos(t - \frac{3}{16}\pi) \\ 1 \cdot \sin(t - \frac{3}{16}\pi) \end{pmatrix} \tag{7.2.2}$$

$$\gamma_{2,\text{unlinked}} = \begin{pmatrix} \cos(\alpha) & -\sin(\alpha) \\ \sin(\alpha) & \cos(\alpha) \end{pmatrix} \cdot \begin{pmatrix} 1.6 \cdot \cos(t + \frac{1}{8}\pi) \\ 0.9 \cdot \sin(t + \frac{1}{8}\pi) \end{pmatrix} \tag{7.2.3}$$

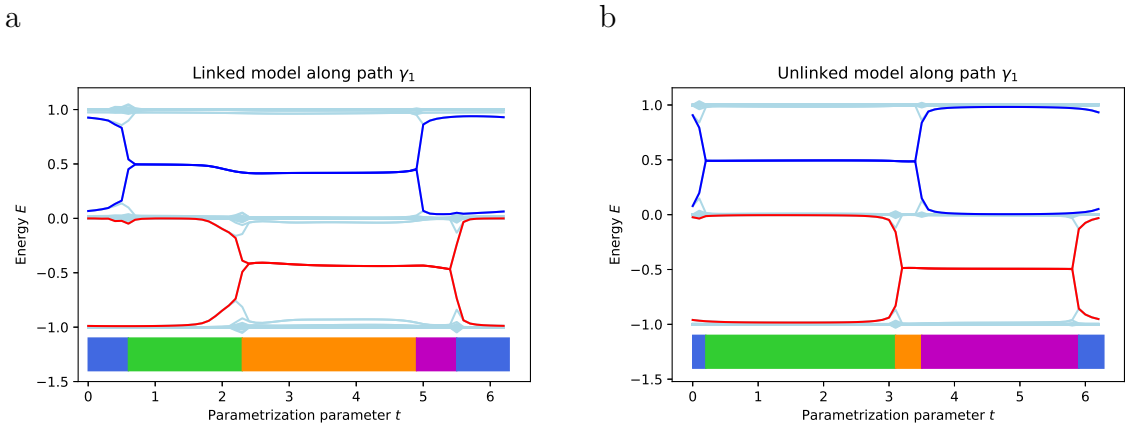

Figure 7.9.: Comparison of the linked and the unlinked model along a path enclosing one node. Panel (a) shows the surface states in the linked model and panel (b) in the unlinked model.

Having defined the paths, we are now able to analyze the surface states along them. Figure 7.9 shows the spectrally flattened finite system along the circular path enclosing a single overlay. From the topological phase diagram, we find the following charges:

$$1 \text{ (blue)} \rightarrow \text{i (green)} \rightarrow \text{j (orange)} \rightarrow \text{k (violet)} \rightarrow 1 \text{ (blue)} \tag{7.2.4}$$

Looking at the surface states, we do not see any qualitative difference between the two models along this path. Only the linked model has a bit more noise in it, probably because this model has a more complicated band dispersion. Furthermore, we can see that for the linked model as it is also the case in the $2D$ model, the surface states do not lie exactly at energy ± 0.5, whereas for the unlinked model they do.

Similarly by looking at the surface states along the elliptical path, we cannot find any difference between the models. The sequence of colors here is:

$$\begin{aligned} \text{i (green)} \rightarrow \text{j (orange)} \rightarrow \text{k (violet)} \rightarrow 1 \text{ (blue)} \rightarrow \text{i (green)} \\ \rightarrow \text{j (orange)} \rightarrow \text{k (violet)} \rightarrow 1 \text{ (blue)} \rightarrow \text{i (green)} \end{aligned} \tag{7.2.5}$$

Again we have a bit more noise and the surface states not at ± 0.5 in the linked model, but the occurring surface states are the expected ones from the topological phases and the bulk-boundary correspondence.

a

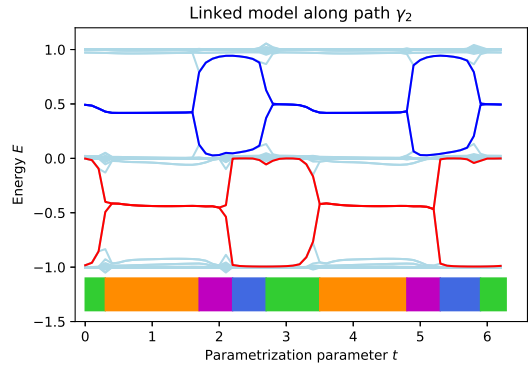

b

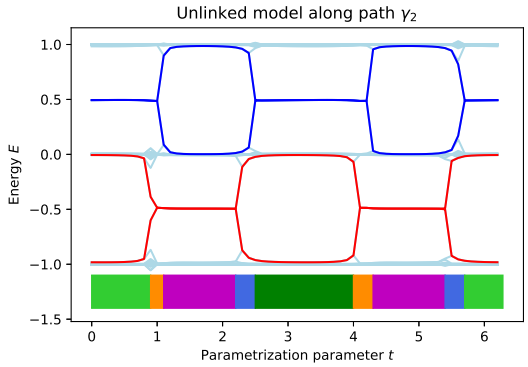

Figure 7.10.: Comparison of the linked and the unlinked model along a path enclosing two overlays. Panel (a) shows the surface states in the linked model and panel (b) in the unlinked model.

So we conclude, that we unfortunately cannot find any difference in the edge spectrum between the linked and the unlinked model as already expected from the similarity of the topological phase diagram combined with the presented bulk-boundary correspondence (see Section 5.2.4).

7.3. Region of charge -1

Last, we want to check our conjecture on the phase with non-Abelian topological charge -1. The conjecture is stated as follows:

Conjecture. *Whenever we have a region in the surface BZ with topological charge -1 (yellow) bounded by charge i (green) on one side and charge k (violet) on the other side, and we take a path starting in the region i (k), passing through the region -1 and ending up in the region k (i), we find one edge state passing through the middle band.*

We now choose several paths going through the region -1, some of them fulfilling the condition that they go from i to k or vice versa, and some of them violating the condition. Unfortunately, we only find the region of charge -1 in the two-dimensional model along the two diagonals. Therefore, we choose several paths in these two finite models (indicated in Figure 7.1b,c).

First, we check the conjecture for paths along $t \in [-10, 10]$ for some fixed values of ϕ. All of them fulfill the condition of the conjecture. For the model finite along the diagonal (11), we take the values $\phi = \pi, \pi - 0.25, \pi - 0.5$. For the one finite along $(1\bar{1})$, we have already seen the case of $\phi = \pi/2$, and in addition consider $\phi = \pi, 3\pi/4, 0$. Figure 7.11 shows the surface states along these paths.

In the case of the system finite along the (11)-diagonal all the crossings are quite clear, whereas for the other termination (finite along $(1\bar{1})$-diagonal) we only observe a clear crossing for the case $\phi = \pi$. For all other cases where $\phi \neq \pi$ (Figure 7.11d and 7.4e) it seems more as if one states merges the middle band and a bit earlier a different state is ejected from the middle band. However, still we have one surface state pumped across the band gap. Finally, for the case of $\phi = 0$, we observe a lot of noise and cannot tell anything about the surface states in the phase -1 as both band gaps are closed.

The many lines inside the band gaps in Figure 7.11f arise from the fact that we do not have a gap. By looking at the topological phase diagram in Figure 5.7 with the indicated paths of the nodal points, we see that we have a gap closing of the upper band gap for $t \in [-9, 2.5]$ and in the lower band gap for $t \in [-2.5, 9]$. In the case of such gap closing we actually cannot do the spectral flattening properly and therefore we observe a lot of additional lines inside the band gaps and not only the actual surface states.

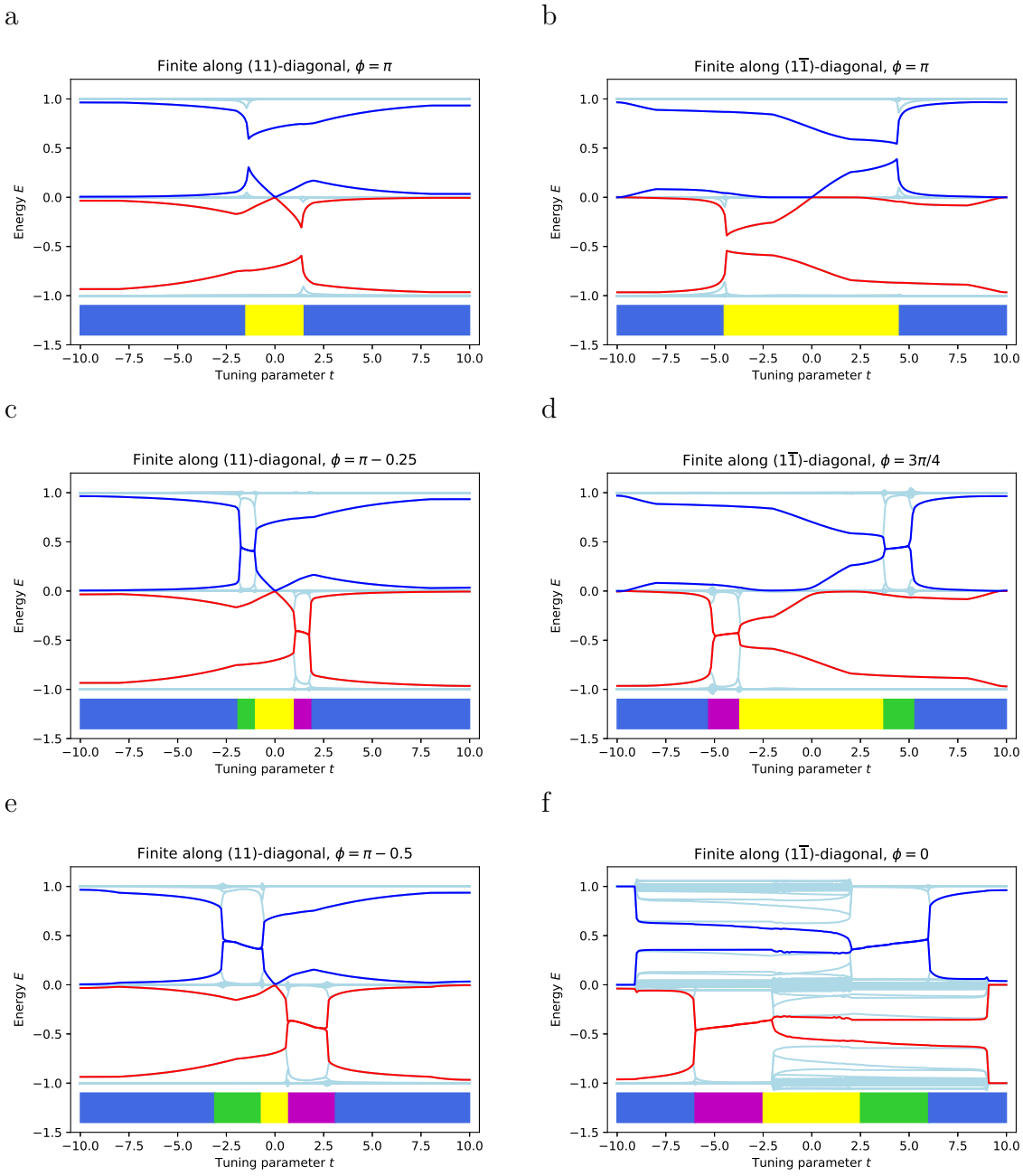

Figure 7.11.: Surface state crossing the middle band along paths at constant ϕ for both diagonal terminations of the $2D$ braiding model. Panels (a),(c) and (e) show two surface states for the finite system along the (11)-diagonal. Along these paths, we can even observe two surface states crossing the middle band but probably only one of them is topological. The surface states of the system finite along the $(1\bar{1})$-diagonal are shown in panels (b), (d) and (f). Looking at panels (a) and (b), we can see that even if we enter the phase of charge -1 from the trivial phase, we still find a surface state passing through the middle band.

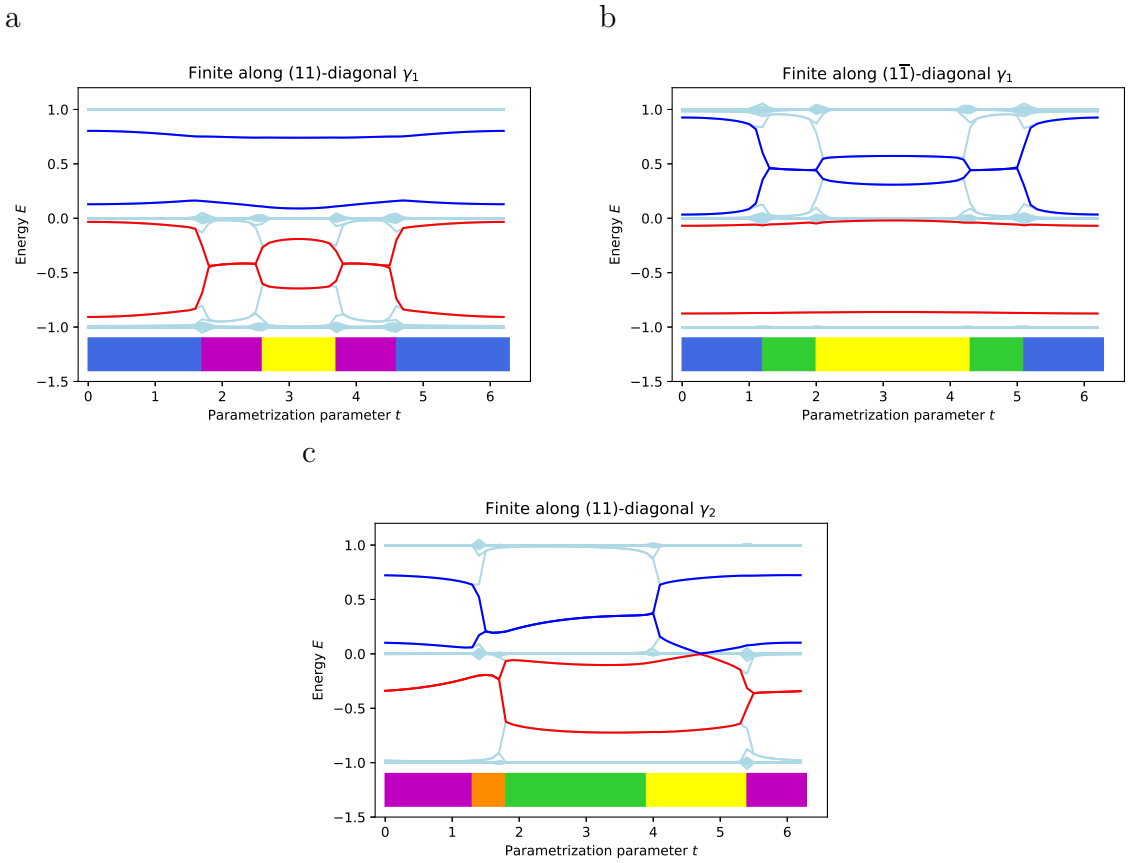

Figure 7.12.: Surface states for some closed paths passing through the region of charge -1 in the $2D$ model. Panel (a) and (b) show the paths that violate the condition of the conjecture and we clearly see no state passing through the middle band. For both terminations (finite along (11) in (a) and finite along $(1\bar{1})$ in (b)), we only find surface states in either the upper or the lower band gap throughout the whole process. Panel (c) shows the surface state for the path fulfilling the condition and we can find a surface state passing the middle band.

As a second step, we now also look at some paths where the condition in the conjecture is violated. Therefore, we take the closed paths shown in Figure 7.1. For the two paths in (orange) we enter and leave the yellow region (charge -1) from the same region either of charge k or i. On the other hand for the third path (pink), we enter the yellow region from the green one and leave it into the violet one. We again parameterize the paths as ellipses in the following way:

$$\gamma_{1,(11)} = \begin{pmatrix} \pi + 0.3 \cdot \cos(t + \pi/2) \\ 1.5 + 1 \cdot \sin(t + \pi/2) \end{pmatrix} \qquad \gamma_{1,(11)} = \begin{pmatrix} \pi + 0.5 \cdot \cos(t + \pi/2) \\ 4.5 + 1 \cdot \sin(t + \pi/2) \end{pmatrix} \tag{7.3.1}$$

$$\gamma_{1,(11)} = \begin{pmatrix} 2.4 + 0.3 \cdot \cos(t + \pi/2) \\ 0 + 1 \cdot \sin(t + \pi/2) \end{pmatrix} \tag{7.3.2}$$

Figure 7.12 shows the surface states along these paths. As expected, we do not find a

surface state passing the middle band in the first two cases, but we can find a crossing approximately at $t = 4.6$ for the last case (panel (c)).

In this chapter, we were able to more precisely specify the bulk-boundary correspondence deduced in Chapter 3 by studying $1D$ elementary models. The only relevant modification corresponds to charge j, where we do not always observe one surface state between the uppermost and the lowest band but sometimes one surface state in each band gap. Further, we specified the behavior of the surface states in the phase of charge -1 depending on the charges surrounding the phase. Unfortunately, in the second part, we were not able to find any difference between the linked and the unlinked model. Finally, we could find some evidence using the two-dimensional model, that our conjecture on the topological phase with charge -1 holds in general.

8. Conclusion and Outlook

8.1. Conclusion

In this work we attempted to better understand the non-Abelian topological charge. Therefore, we studied different models in various dimensions and with varying number of bands.

We started with elementary one-dimensional models consisting of three flat bands. By performing different rotations of the three eigenstates throughout the BZ, we were able to realize the different topological charges and found the corresponding edge states (some of this analysis was already done by Ref. [3] in the Supplementary material). Then, we generalized these models to N flat bands and had a closer look at different filling fractions for the N-band model. We further found some evidence that in the topological phase with charge -1 it is possible to pump one edge state across all the middle bands from the uppermost to the lowest band gap. In the elementary three band model we could even find an analytic solution for this pumped edge state and found that it is perfectly localized on the outermost site.

After this simple one-dimensional model, we had a closer look at the two-dimensional model presented by Ref. [29]. This model exhibits nodal points that perform a braiding along a tuning parameter t. We then calculated the topological phase diagrams for different terminations of the model. Interesting about this model is, that along both diagonal projections, we find the topological phase with charge -1.

Last, we considered two original $3D$ models. We constructed these models in a way that their nodal lines look similar along the diagonal projection but in one case the nodal lines are linked and in the other case they are unlinked. Also for this model, we calculated the quaternion charge but they do not show the topological phase of charge -1.

We then studied the surface states of the presented two- and three-dimensional models in the slab geometry, finite along different directions. Therefore, we used several techniques that either use the actual band dispersion of the models or use a Hamiltonian with flattened bands.

First, we used different paths through the BZ of the models in slab geometry and were able to find a bulk-boundary correspondence for the surface states and the topological charge in the phase diagram.

Our second goal was to find a difference in the surface spectrum of the linked and the unlinked model. Therefore, we took two paths in the linked and the unlinked model enclosing one and two overlays of nodal lines, respectively, but unfortunately, we could

not find any difference in the surface spectrum. The absence of a clear-cut difference, we could already guess from the similarity of the topological phase diagram and the established bulk-boundary correspondence between the surface states and the quaternion charge.

The last thing we studied, was the behavior of the surface states in the topological phase with charge -1. We formulated the conjecture that under some constraint in the phase -1, there is always a surface state passing through the middle band. Taking different paths in the topological phase diagram of the two-dimensional braiding model, we were able to support our conjecture.

8.2. Outlook

Although we could gain some insight into this non-Abelian topological charge, there are still some open questions, we did not address to but that are definitely worth further research.

Looking at the spectrum of the flattened Hamiltonian of the different models, we observe that the surface states are not always at the same energy. Often they have energy close to the middle of the band gap, i.e. ± 0.5 but not always. Especially in the linked modal in $3D$ as well as in the braiding model, we often observe the surface states at arbitrary energies, e.g. Figures 7.9a and 7.3e. An interesting related question is whether it is possible to determine the energy the surface state has in the flattened Hamiltonian. Perhaps it could even be possible to differentiate the linked and the unlinked model using this different energies of the surface states in the spectrally flattened Hamiltonian. For the linked model it seems as if the surface states attract each other in energy if at the same position there is one in each band gap, e.g. 7.9 where we clearly see a small dropping of the energy of the surface state in the upper band gap at $t \approx 2.2$.

A second interesting aspect also observed in the flattened Hamiltonian, we see for example in Figure 7.11a where we look at the $2D$ braiding modal, finite along the (11) diagonal at a path along t for the value $\phi = \pi$. In this case, from the topological phase diagram we know that we enter the phase with charge -1 directly from the phase with charge 1. Concerning the surface states, we would expect non of them in the trivial phase and two of them for the charge -1. Looking at the Figure, we can actually observe already some trivial surface state in the phase with charge 1 that turn into topological ones when entering the phase of charge -1. Further we also observe too many surface states in the phase of charge -1 of which it would be interesting to know which ones are topological. So the interesting question here is, how can we distinguish between a trivial and a topological surface state. One possibility could be to use the slope of the state when approaching the boundary of the topological phase. Looking for example at Figure7.11a, we suggest that probably the slope of the topological state diverges when approaching the topological phase transition (e.g. in the upper band gap for $\phi \approx 2$).

Another possibility to do further research could be to choose different model. On one hand, one could try to add the additional lines proposed in Section 5.2.4 to the unlinked

model, to arrive at two models that look even more similar than they do at the moment. Then one could study the surface states again to check if there is really no difference in the surface spectrum of the linked and the unlinked model.

On the other hand, one could set up some different models. One idea would be to change the positions of the orbitals inside the unit cell. Instead of centering all of them, they could be placed at different positions. Studying the surface states it could be interesting to check the behavior of the surface states depending on the topological charge also in this case.

Another possibility to change the models would be to study models with more then three bands[1] and then looking at the generalized quaternions. An interesting question would be if also for more bands, we still observe a surface state crossing the middle bands in the phase of charge -1 or if the state only crosses some of the middle bands depending on the charge on the boundary of the phase with charge -1. In general it would be interesting to find a correspondence between the surface states and the topological charge also for more than three bands.

However, besides these further ideas concerning the two- and three-dimensional semimetals, there remain also open questions concerning the one-dimensional model.

In the trivialization of the 4π-rotation, we observed a degeneracy around $m \approx 17$ in Figure 3.7. The question here is whether this degeneracy is a purely accidental feature of our specific model or if there is a topological reason behind this and it would also occur for other trivializations of a 4π-rotation, thereby being topological stable.

Furthermore, in the one-dimensional N-band model, we have seen that we can pump one edge state from the uppermost to the lowest band gap. The question that remains is whether we are able to define a periodically driven system (Floquet system) to pump this edge state up to the highest band gap again to end up with a closed cycle in energy.

[1] We did this in the case of the $1D$-system but not for higher dimensions.

A. Topology

Here, we give a short overview on some topological concepts used in the main text (mainly in Section 2.2). We start with the different properties of topological spaces (connected, path connected, simply connected), then define homotopy groups and covering spaces. Finally, we give some simplifications for spaces that are usually encountered in physics.

A.1. Topological spaces

A topological space S is connected if the only subsets $M \subset S$ which are closed and open at the same time are S itself and the empty set $\emptyset$. This is equivalent to stating that a space is connected if it is not the union of two non-empty disjoint sets.

Path connected is a slightly stronger property that implies connected. If for each two points $a, b \in S$ there exists a path $\alpha : [0,1] \to S$ with $\alpha(0) = a$ and $\alpha(1) = b$ the topological space S is called path-connected. There exist some spaces that are connected but not path-connected. Last, we want to define simply connectedness which is the strongest property. A topological space S is simply connected if it is path-connected and every path between the end points a, b can be continuously deformed to any other path between the same end points. Equivalently (by taking $a = b$, this means that every closed path in the space is contractible [39, 40].

An equivalent definition for simply connected is that it is path-connected and the first homotopy group, also called the fundamental group, is trivial. Therefore, we want to define the fundamental group.

A.2. Homotopy groups

First, we need to define what a homotopy is. Consider a family of paths $\gamma_t : I \to X$ with X a topological space, I the interval $[0,1]$ and $0 \leq t \leq 1$. This family is called a homotopy of paths if i) the end points are independent of t, i.e. $\gamma_t(0) = x_0$ and $\gamma_t(1) = x_1$, and ii) the map $F : I \times I \to X$ defined as $F(s,t) = \gamma_t(s)$ is continuous. We say that two paths γ_0 and γ_1 are homotopic if they are connected by such a homotopy of paths γ_t and we write $\gamma_0 \simeq \gamma_1$. For fixed end points, this is an equivalence relation and we can define equivalence classes.

Using this, we are now able to define the fundamental group $\Pi_1(X, x_0)$ of the topological space X for a base point x_0. It is the quotient group of all paths γ with base point

(start and end point) x_0, modulo the homotopy of paths. So in formula we write:

$$\Pi_1(X, x_0) = \{\text{set of all closed paths } \gamma \text{ with base point } x_0\}/\{\text{homotopy of paths}\} \tag{A.2.1}$$

In path-connected spaces the fundamental group is independent of the base point and we simply call it $\Pi_1(X)$.

An example for a space with non-trivial fundamental group is a torus T^2 whose fundamental group is $\mathbb{Z} \times \mathbb{Z}$. Conversely, a ball or the sphere S^2 are examples of spaces with trivial fundamental groups. In a similar way, we can also define the nth homotopy group. Therefore, we generalize the interval $I = [0, 1]$ to I^n with the boundary ∂I^n, the subspace where at least one coordinate is equal to 0 or 1. Then, we can define the nth homotopy group ($n \geq 2$) of the space X with base point x_0 denoted by $\Pi_n(X, x_0)$ to be the homotopy class of maps $f : (I^n, \partial I^n) \to (X, x_0)$. The family of paths f_t need to satisfy the condition $f_t(\partial I^n) = x_0$. In the case of $n = 1$ this is exactly the definition of the fundamental group. We can further extend the definition to $n = 0$ where I^0 is a point and its boundary is the empty set. So the zeroth homotopy group $\Pi_0(X, x_0)$ is just the set of path-connected components of X. Similar to the case of the fundamental group, the higher homotopy groups for path-connected spaces are independent on the choice of the base point, and we can write $\Pi_n(X)$. A special property of the homotopy groups is that for $n \geq 2$ the groups $\Pi_n(X)$ are Abelian [40].

A.3. Covering spaces

Finally, we want to consider covering spaces of topological spaces. A covering space of a topological space X is a space $\tilde{X}$ with a map $p : \tilde{X} \to X$ with the property that for each point $x \in X$ there exists a neighborhood U such that $p^{-1}(U)$ is a union of disjoint open sets mapped homeomorphically on U by the map p.
For each connected space which is locally path-connected and semilocally simply connected there exists a simply connected covering space, called the universal cover. It is locally the same as the original space but has now a fundamental group which is trivial. Simply connected spaces are their own universal covers [40].

A.4. Application in physics

In physics most connected spaces are also path-connected and we therefore define the homotopy groups independent of the base points. Indeed most spaces in physics are manifolds M and each connected manifold has a universal cover. To see this, we use the fact that each manifold is locally contractible. This is the case because each point in a manifold has a neighborhood which is homeomorphic to an Euclidean space that is clearly contractible. Locally contractible then implies locally connected, locally path-connected and locally simply connected. So if we further assume that the manifold is

connected, we see that it fulfills all the conditions to have a universal cover. In addition, the universal cover of a manifold is a manifold as well [40].

B. Real-space version of the $3D$-models

Using the same technique as in Section 6.1 to sketch the situation with L layers, we can find the blocks in the Hamiltonian (Eq. 6.1.1) for the linked and the unlinked model (Eq.'s 5.2.3 and 5.2.10). For the linked model we construct the system that is finite along the x-axis as well as the one finite along the (110)-diagonal, whereas for the unlinked model we only take the system finite along (110). This time, we also need to include the blocks $t^{\pm 2}$ and for the linked case also $t^{\pm 3}$. Similar to the treatment of the tuning parameter t in the $2D$ model, also for the $3D$ model we fix the values of k_z and look at one-dimensional models in the (k_x, k_y)-plane. The blocks then look as follows: For the linked model, finite along x and quantum number $k = k_y$:

$$
\begin{aligned}
t^0 &= \begin{pmatrix} 9 - 3\cdot\cos(k) + 4\cdot\cos(2k_z) & 0 & \mathrm{i}\cdot\sin(k) \\ 0 & 6.25 - 2.5\cdot\cos(k) + 4\cdot\cos(2k_z) & 0 \\ -\mathrm{i}\cdot\sin(k) & 0 & 1 - 1\cdot\cos(2k_z) \end{pmatrix} \\
t^1 &= \begin{pmatrix} -1.5 & -\mathrm{i}\cdot\sin(k) & 0 \\ -\mathrm{i}\cdot\sin(k) & -1.5 & 0.5 \\ 0 & -0.5 & 0 \end{pmatrix} \qquad t^{-1} = t^{1\dagger} \\
t^2 &= \begin{pmatrix} 0 & 0 & 0 \\ 0 & -0.75 - 0.5\cdot\cos(k) & 0 \\ 0 & 0 & -1 \end{pmatrix} \qquad t^{-2} = t^{2\dagger}
\end{aligned}
\tag{B.0.1}
$$

finite along the diagonal (110) with quantum number $k = k_- = \frac{1}{\sqrt{2}}(k_x - k_y)$:

$$
\begin{aligned}
t^0 &= \begin{pmatrix} 9 + 4\cdot\cos(2k_z) & 1\cdot\cos(k) & 0 \\ 1\cdot\cos(k) & 6.25 + 4\cdot\cos(2k_z) & 0 \\ 0 & 0 & 1 - 1\cdot\cos(2k_z) \end{pmatrix} \\
t^1 &= \begin{pmatrix} -1.5\cdot\left(1 + e^{\mathrm{i}k}\right) & 0 & 0.5 \\ 0 & -1.25 - 1.5\cdot e^{\mathrm{i}k} - 0.25\cdot e^{2\mathrm{i}k} & 0.5\cdot e^{\mathrm{i}k} \\ -0.5 & -0.5\cdot e^{\mathrm{i}k} & 0 \end{pmatrix} \qquad t^{-1} = t^{1\dagger} \\
t^2 &= \begin{pmatrix} 0 & -0.5\cdot e^{\mathrm{i}k} & 0 \\ -0.5\cdot e^{\mathrm{i}k} & -0.75\cdot e^{2\mathrm{i}k} & 0 \\ 0 & 0 & -e^{2\mathrm{i}k} \end{pmatrix} \qquad t^{-2} = t^{2\dagger} \\
t^3 &= \begin{pmatrix} 0 & 0 & 0 \\ 0 & -0.25\cdot e^{2\mathrm{i}k} & 0 \\ 0 & 0 & 0 \end{pmatrix} \qquad t^{-3} = t^{3\dagger}
\end{aligned}
\tag{B.0.2}
$$

For the unlinked model finite along the (110)-diagonal and quantum number $k = k_- = \frac{1}{\sqrt{2}}(k_x - k_y)$:

$$
\begin{aligned}
t^0 &= \begin{pmatrix} -6.6 + 3\cdot\cos(2k_z) & 1\cdot\cos(k) & 0 \\ 1\cdot\cos(k) & 2 + 3\cdot\cos(2k_z) & 0 \\ 0 & 0 & -3.5 \end{pmatrix} \\
t^1 &= \begin{pmatrix} 1 & 0 & 0.5 \\ 0 & 1 + e^{\mathrm{i}k} & 0.5\cdot e^{\mathrm{i}k} \\ -0.5 & -0.5\cdot e^{\mathrm{i}k} & -e^{\mathrm{i}k} \end{pmatrix} \qquad t^{-1} = t^{1\dagger} \\
t^2 &= \begin{pmatrix} 0 & -0.5\cdot e^{\mathrm{i}k} & 0 \\ -0.5\cdot e^{\mathrm{i}k} & 0 & 0 \\ 0 & 0 & 0 \end{pmatrix} \qquad t^{-2} = t^{2\dagger}
\end{aligned}
\tag{B.0.3}
$$

These blocks for the finite models could also be found by a Fourier transform, which in the case of many hopping (as in our $3D$ models) is less prone to mistakes. Again we only consider cuts at different values of k_z. We then have an effective $2D$ Hamiltonian $\mathcal{H}_{\text{eff}}(k_x, k_y)$ represented as a 3×3-matrix. For such Hamiltonians, we can find the hopping blocks directly by taking the Fourier transform along the finite axis. Considering the Hamiltonian to be finite along the x-direction (good quantum number k_y), we have the following formula for the blocks:

$$
\left(t^n(k_y)\right)_{\alpha\beta} = \frac{1}{2\pi}\int_{-\pi}^{\pi} e^{\mathrm{i}nk_x}\left(\mathcal{H}_{\text{eff}}(k_x, k_y)\right)_{\alpha\beta}\, dk_x \tag{B.0.4}
$$

This integral can either be evaluated analytically with the help of Mathematica or we can do it numerically using Python. For the diagonal termination of the models, we need to express them using the momenta k_+, k_- and then do the same Fourier transform as we did above for k_x, k_y.

C. Convention for the discrete Fourier transform

Consider a function $f(x)$ in real space at N discrete values x_i. We find the coefficients $F(k)$ of the Fourier transform by the following formula: For one dimensional functions:

$$F_n = \sum_{m=1}^{N} f_m \exp\left(-i\frac{2\pi}{N}nm\right) \tag{C.0.1}$$

and the inverse Fourier transform as:

$$f_m = \frac{1}{N}\sum_{n=1}^{N} F_n \exp\left(i\frac{2\pi}{N}nm\right) \tag{C.0.2}$$

In two dimensions we have:

$$F_{n_1,n_2} = \sum_{m_1=1}^{N}\sum_{m_2=1}^{N} f_{m_1,m_2} \exp\left(-i\frac{2\pi}{N}(n_1m_1 + n_2m_2)\right) \tag{C.0.3}$$

as well as the inverse transformation:

$$f_{m_1,m_2} = \frac{1}{N^2}\sum_{n_1=1}^{N}\sum_{n_2=1}^{N} F_{n_1,n_2} \exp\left(i\frac{2\pi}{N}(n_1m_1 + n_2m_2)\right) \tag{C.0.4}$$

D. Number of sites for finite systems

We justify our choice of $N = L = 100$ used in Chapter 7. Therefore, we first look at the $2D$ braiding model for a system finite along the y-axis and $t = 0$. We compare the spectrum with open boundary conditions for different number of layers L. Second, we look at the linked system along the path $\gamma_{1,\text{linked}}$ in Equation (7.2.1) and check the behavior of the flattened model depending on the number of sites N. For both systems we compare the results for the following number of sites/layers: $10, 20, 50, 80, 100, 150, 200, 300$.

Figure D.1 shows the spectrum with open boundary conditions for the different number of layers. Already for $L = 10$, we can see the surface states, but we see only few single lines for the bulk states. Starting from $L = 50$, we see the bulk bands much clearer but we still see single lines. For $L \geq 100$ and the presented data resolution, we do not see lines anymore for the bulk bands but really one area covering the range of the bulk bands. Therefore in this case $L = 100$ seems to be a good choice because by choosing L even larger it does not provide further improvements of the presented data (except the time needed for the computation grows rapidly).

The same is shown for the linked model and the technique of the spectral flattening in Figure D.2. Again, we can already see the surface states for $N = 10$. However, the bulk bands seem to have some dispersion. For $N = 50$ the surface states get quite clear and most of the bulk dispersion is gone. The changes by further increasing N are quite small but the spectrum gets sharper each time until $N = 200$. Between $N = 200$ and $N = 300$ the spectrum does not change anymore within the naked eye resolution. In this case $N = 100$ is a good choice as the spectrum is sharp enough and does not change much by further increasing N, while the computation time is still quite short.

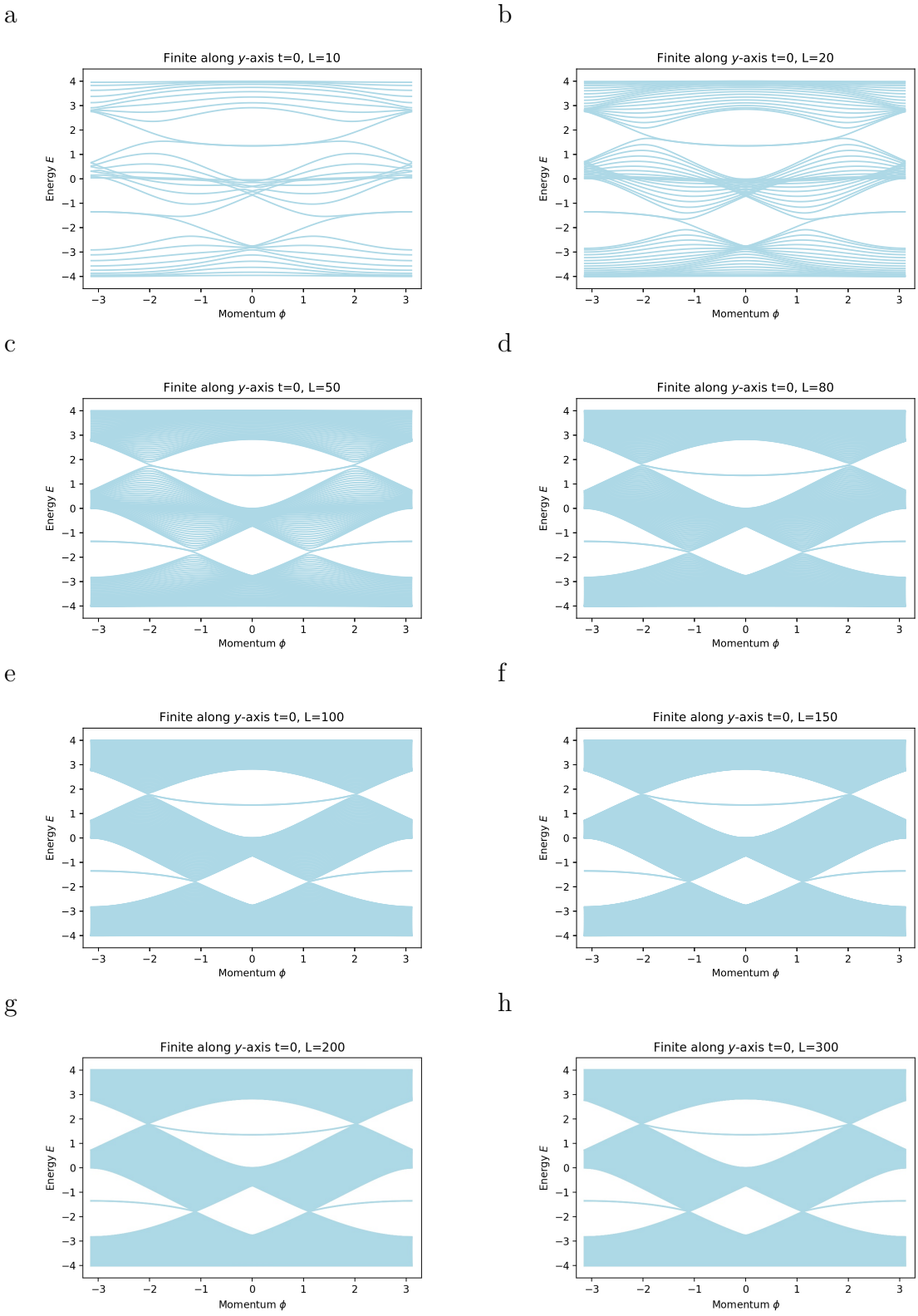

Figure D.1.: Effect of the choice layers L on the spectrum of a lD-system with open boundary conditions. For an illustration, we look at the $2D$ braiding model finite along the y-axis for the value $t = 0$

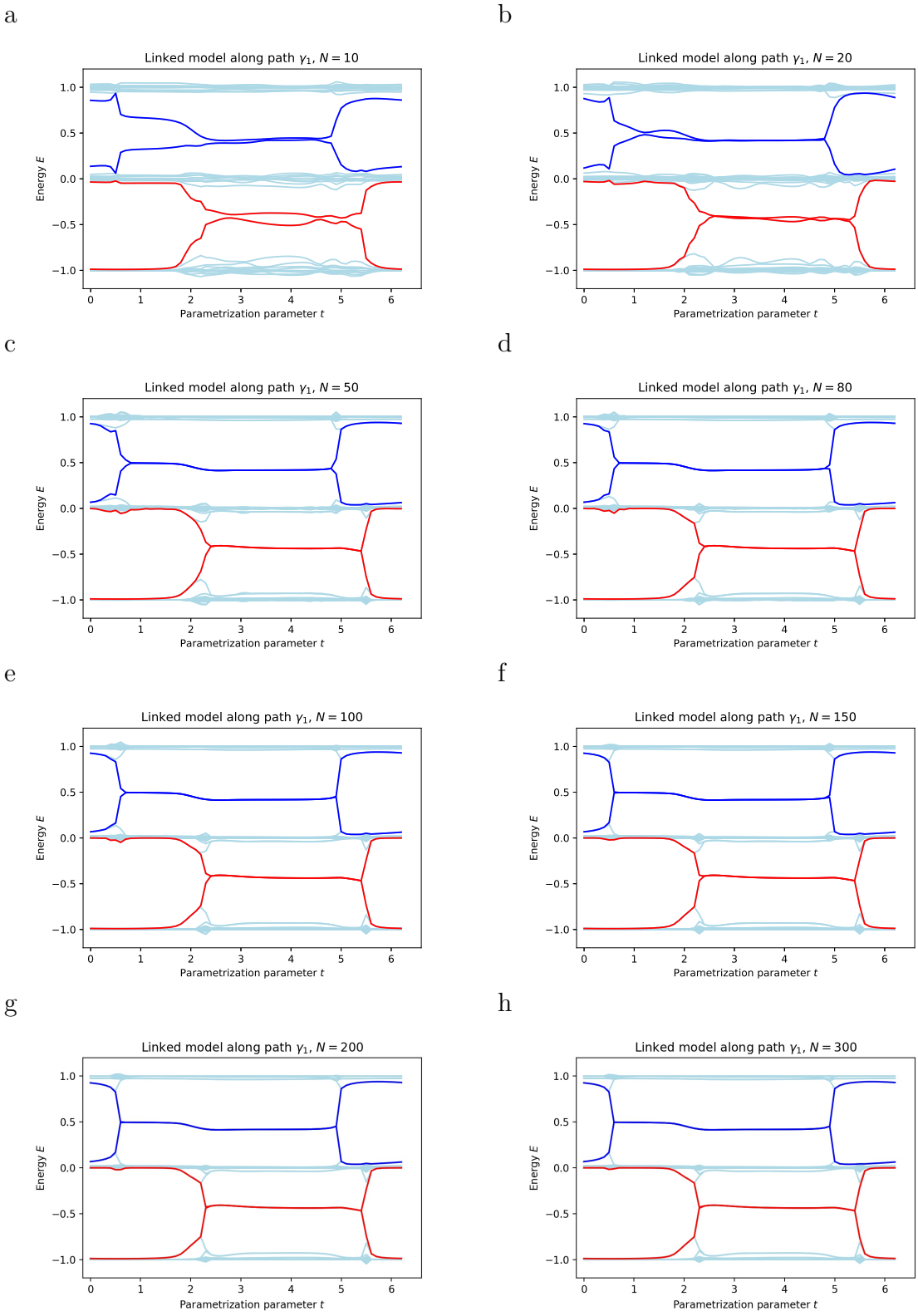

Figure D.2.: Effect of the choice of N (number of sites) on the spectrum of a spectrally flattened lD-system with open boundary conditions. For an illustration, we look at the unlinked model along the circular path in Equation 7.2.1.

List of Figures

List of Tables

Bibliography

[1] Haijun Zhang, Chao-Xing Liu, Xiao-Liang Qi, Xi Dai, Zhong Fang, and Shou-Cheng Zhang. Topological insulators in Bi_2Se_3, Bi_2Te_3 and Sb_2Te_3 with a single Dirac cone on the surface. *Nature Physics*, 5(6):438–442, 2009.

[2] Frank Arnold, Marcel Naumann, Shu-Chun Wu, Yan Sun, Marcus Schmidt, Horst Borrmann, Claudia Felser, Binghai Yan, and E. Hassinger. Chiral Weyl pockets and Fermi surface topology of the Weyl semimetal TaAs. *Physical Review Letters*, 117(14):146401, 2016.

[3] QuanSheng Wu, Alexey A. Soluyanov, and Tomáš Bzdušek. Non-Abelian band topology in noninteracting metals. *Science*, 365(6459):1273–1277, 2019.

[4] Michael V. Berry. Quantal Phase Factors Accompanying Adiabatic Changes. *Proceedings of the Royal Society of London. Series A, Mathematical and Physical Sciences*, 1984.

[5] Andrei B. Bernevig and Taylor L. Hughes. *Topological insulators and topological superconductors*. Princeton University Press, 2013.

[6] Michael V. Berry. *A.Shapere, F.Wilczek. Geometric Phases in Physics*, chapter The quatmum phase, five years after, pages 7–28. World Scientific, 1989.

[7] Thomas Ihn. *Topology in Physics. From Geometry to Condensed Matter Systems*. ETH Zürich, 2018. `https://people.phys.ethz.ch/~ihn/Topology/TopologyInCondensedMatter_ThomasIhn_12Jun2018.pdf`, accessed: 18.07.2020.

[8] Brian C. Hall. *Lie Groups, Lie Algebras, and Representations. An Elementary Introduction*. Springer International Publishing, 2015.

[9] Ming-Che Chang. Berry phase in solid state physics. Department of Physics, National Taiwan Normal University. `https://phy.ntnu.edu.tw/~changmc/Paper/Berry_IFF_FF_4.pdf`, accessed: 25.8.2020.

[10] David Vanderbilt. *Berry Phases in Electronic Structure Theory: Electric Polarization, Orbital Magnetization and Topological Insulators*. Cambridge University Press, 1st edition, 2018.

[11] Gern Czycholl. *Theoretische Festkörperphysik Band 1: Grundlagen: Phononen und Elektronen in Kristallen*. Springer: Berlin, 4th edition, 2016.

[12] Joshua Zak. Berry's Phase for Energy Bands in Solids. *Physical Review Letters*, 62(23), 1989.

[13] Gilles Montambaux, Lih-King Lim, Jean-Noël Fuchs, and Frédéric Piéchon. Winding Vector: How to Annihilate Two Dirac Points with the Same Charge. *Physical Review Letters*, 121(25):256402, 2018.

[14] N. David Mermin. The topological theory of defects in ordered media. *Reviews of Modern Physics*, 51(3):591–648, 1979.

[15] Mark Staley. Understanding quaternions and the Dirac belt trick. *European Journal of Physics*, 31(3):467–478, 2010.

[16] Nicolas Borghini. *Lecture: Symmetries in Physics*, chapter The groups SO(3) and SU(2) and their representations, pages 69–75. University Bielefeld, 2018. `https://www.physik.uni-bielefeld.de/~borghini/Teaching/Symmetries/12_15.pdf`, accessed: 20.7.2020.

[17] Dominik Gresch, Gabriel Autès, Oleg V. Yazyev, Matthias Troyer, David Vanderbilt, B. Andrei Bernevig, and Alexey A. Soluyanov. Z2Pack: Numerical implementation of hybrid Wannier centers for identifying topological materials. *Physical Review B*, 95(7):075146, 2017.

[18] Patrick M. Lenggenhager, Xiaoxiong Liu, Stepan S. Tsirkin, Titus Neupert, and Tomáš Bzdušek. Multi-band nodal links in triple-point materials. *arxiv:2008.02807*, 2020.

[19] Robert B. Laughlin. Quantized Hall conductivity in two dimensions. *Physical Review B*, 23(10):5632–5633, 1981.

[20] Martin Holthaus. Floquet engineering with quasienergy bands of periodically driven optical lattices. *Journal of Physics B: Atomic, Molecular and Optical Physics*, 49(1):013001, 2015.

[21] Wladimir A. Benalcazar, Tianhe Li, and Taylor L. Hughes. Quantization of fractional corner charge in C_n-symmetric higher-order topological crystalline insulators. *Physical Review B*, 99(24):245151, 2019.

[22] John von Neumann and Eugene P. Wigner. Über das Verhalten von Eigenwerten bei adiabatischen Prozessen. *Physikalische Zeitschrift*, 30:467–470, 1929.

[23] Apoorv Tiwari and Tomáš Bzdušek. Non-Abelian topology of nodal-line rings in $\mathcal{PT}$-symmetric systems. *Physical Review B*, 101(19):195130, 2020.

[24] Chen Fang, Hongming Weng, Xi Dai, and Zhong Fang. Topological nodal line semimetals. *Chinese Physics B*, 25(11), 2016.

[25] János K. Asbóth, László Oroszlány, and András Pályi. *A Short Course on Topological Insulators. Lecture Notes in Physics*. Springer International Publishing, 2016.

[26] Andrea F. Young, Yuanbo Zhang, and Philip Kim. *Physics of Graphene*, chapter Experimental Manifestation of Berry Phase in Graphene. Springer: Cham, 2013.

[27] N. Peter Armitage, Eugene J. Mele, and Ashvin Vishwanath. Weyl and Dirac semimetals in three-dimensional solids. *Reviews of Modern Physics*, 90(1):015001, 2018.

[28] Holger Bech Nielsen and Masao Ninomiya. Absence of neutrinos on a lattice: (i). Proof by homotopy theory. *Nuclear Physics B*, 185(1):20 – 40, 1981.

[29] Adrien Bouhon, QuanSheng Wu, Robert-Jan Slager, Hongming Weng, Oleg V. Yazyev, and Tomáš Bzdušek. Non-Abelian Reciprocal Braiding of Weyl Nodes and its Manifestation in ZrTe. *Nature Physics*, 2020.

[30] Zhijun Wang, Benjamin J. Wieder, Jian Li, Binghai Yan, and B. Andrei Bernevig. Higher-Order Topology, Monopole Nodal Lines, and the Origin of Large Fermi Arcs in Transition Metal Dichalcogenides $X\mathrm{Te}_2$ ($X = \mathrm{Mo}, \mathrm{W}$). *Physical Review Letters*, 123(18):186401, 2019.

[31] Junyeong Ahn, Dongwook Kim, Youngkuk Kim, and Bohm-Jung Yang. Band Topology and Linking Structure of Nodal Line Semimetals with Z_2 Monopole Charges. *Physical Review Letters*, 121(10):106403, 2018.

[32] Junyeong Ahn, Sungjoon Park, and Bohm-Jung Yang. Failure of Nielsen-Ninomiya Theorem and Fragile Topology in Two-Dimensional Systems with Space-Time Inversion Symmetry: Application to Twisted Bilayer Graphene at Magic Angle. *Physical Review X*, 9(2):021013, 2019.

[33] Zhesen Yang, Andreas P. Schnyder, Jiangping Hu, and Ching-Kai Chiu. Fermion doubling theorems in 2D non-Hermitian systems for Fermi points and exceptional points. *arXiv:1912.02788*, 2019.

[34] Adrien Bouhon, QuanSheng Wu, Robert-Jan Slager, Hongming Weng, Oleg V. Yazyev, and Tomáš Bzdušek. Non-Abelian Reciprocal Braiding of Weyl Nodes and its Manifestation in ZrTe. *arXiv:1907.10611v3*, 2019. Version 3.

[35] Nimisha Raghuvanshi and Avinash Singh. The role of Hund's coupling in the stabilization of the (0, π) ordered spin density wave state within the minimal two-band model for iron pnictides. *Journal of Physics: Condensed Matter*, 23(31):312201, 2011.

[36] Mahito Kohmoto and Yasumasa Hasegawa. Zero modes and edge states of the honeycomb lattice. *Physical Review B*, 76(20):205402, 2007.

[37] Andrea Damascelli, Zahid Hussain, and Zhi-Xun Shen. Angle-resolved photoemission studies of the cuprate superconductors. *Review of Modern Physics*, 75(2):473–541, 2003.

[38] Rafael A. Méndez-Sánchez, Lil Gutiérrez, Miguel A. Morales, Jordy Flores, Alfredo Diaz-de Anda, and Guillermo Monsivais. Anderson Localization Phenomenon in One-Dimensional Elastic Systems. *Acta Physica Polonica A*, 124(6):1063, 2013.

[39] Klaus Jänich. *Topologie*. Springer: Berlin, 8th edition, 2005.

[40] Allen Hatcher. *Algebraic topology*. Cambridge University Press, 2002.